2-9-2010

Synthesis and evaluation of rare-earth doped glasses and crystals for optical refrigeration

Wendy Marie Patterson

Wendy Patterson

Candidate

Physics and Astronomy

Department

This dissertation is approved, and it is acceptable in quality
and form for publication:

Approved by the Dissertation Committee:

Mansoor Sheik-Bahae , Chairperson

Markus Hehlen

James Thomas
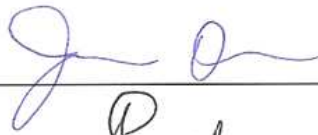
Sanjay Krishna

**SYNTHESIS AND EVALUATION OF RARE-EARTH DOPED
GLASSES AND CRYSTALS FOR OPTICAL REFRIGERATION**

BY

WENDY PATTERSON

B.S., The University of Alabama in Huntsville, 2000
M.S., The University of Alabama in Huntsville, 2002
M.S., The University of New Mexico, 2008

DISSERTATION

Submitted in Partial Fulfillment of the
Requirements for the Degree of

Doctor of Philosophy

Optical Science and Engineering

The University of New Mexico
Albuquerque, New Mexico

December, 2009

DEDICATION

Together with my family, we dedicate this work to the memory of my sweet baby brother. Words seem too simple express how much we love and miss you. Siempre.

.

ACKNOWLEDGMENTS

Though only my name appears on the cover of this dissertation, as we all know, science does not happen in a vacuum. Well, figuratively. Faculty, friends, and family members have helped me complete this dissertation and I would like to express my gratitude for their support and assistance. Traditionally, the Acknowledgements section of a Ph.D. dissertation remains a dry outlet for obligatory recognitions and eloquent denunciations but I give you neither, only my deepest sincerity. Given my propensity for verbosity, over-sentimentalism, and sarcasm (not to mention potty humor), I constantly struggle to purge this style from my scientific writings. Here I present my sincere gratitude, uncensored. If you cringe at this section, I hope you accept the remainder of the document to balance reason, logic and good science, and will forgive me in time.

First, I would like to thank my advisor at UNM, Dr. Mansoor Sheik-Bahae for his thought-provoking, constructive criticisms at different stages of my research. I am grateful to him for holding me to a high research standard and enforcing strict validations of the results. Without the support (financial and academic) and opportunities (allowing me to do research at LANL for 2.5 years) provided by Mansoor, I could not have pursued this research. I appreciate his patience with me throughout the years and especially his awareness of my female sensibilities (i.e., I'm a girl and my feelings get hurt easily). He has always given me great freedom and independence while pursuing this research. Many graduate students are not given the opportunity to develop their own individuality and self-sufficiency by being allowed to work with such independence. Essentially, no graduate student is fond of a hovering advisor and for that, I extend sincere gratitude.

For the second time in my life, after the summer of 2006, I was ready to quit graduate school and for the second time in my life, at the most opportune moment, I met someone who gave me another chance to prove myself. Before meeting with my LANL advisor, Dr. Markus Hehlen in August of 2006, I doubted my ability to finish this research at all, much less in a timely manner. Markus helped me outline an ambitious timetable for finishing that carried me through the next years. Markus has always shown faith in my research and abilities and has always been a strong advocate for me. As a scientist, he is someone I greatly admire and simultaneously envy ("WHY didn't I think of that?!"). He encouraged me to not only grow as an experimentalist and a chemist, but also as an independent thinker. He would always supply a near immediate reply to my sometimes (let's be honest, oftentimes) rambling, incoherent, late night emails. His generosity with his time throughout this endeavor has been unconditional and disarmingly cheerful.

I also thank my other committee members, Drs. Sanjay Krishna and James Thomas, for their valuable recommendations pertaining to this work. I feel that I had a uniquely supportive committee and I thank them for reading and providing feedback for my dissertation.

Gratitude is extended to many at LANL including Dr. Scott Greenfield, for allowing me to use both of his laser labs at LANL, without restriction, and offering

guidance with the equipment whenever needed. I also thank Dr. Richard Epstein, for being a mentor with respect to laser cooling specifically, and life generally - offering an optimistic perspective with his clever, insightful comments. I also thank Drs. Pete Stark and Tom Yoshida at LANL for their assistance with the ICP-MS samples.

To my research group – specifically to Denis Seletskiy who at the last minute helped me maintain my sanity. Had I been required to do that last experiment you so graciously helped me with, I would have certainly been committed.. and not to an institution of higher learning. Thank you Denis, sincerely. Daniel Bender might very well be the only graduate student I have known who never whines. This has not stopped me from whining in his presence, but it may have slowed me down somewhat. I also blame all errors in the manuscript on him, just because I can. We made it through the toughest years of our lives together and I am thankful for the many laughs we had, and continue to share. Thanks to Mike Hasselbeck, who made the "Babak Years" somewhat bearable and has always been there any time I ever asked for a favor, without exception.

As I discovered, the Ph.D. (even in a hard science) is less about academics and more about maintaining emotional/psychological stability in the face of adversity. For this, my outlet for pent-up frustrations occurred in my free time, primarily spent with friends. All types, all with varying political, cultural and academic backgrounds, all helping me in ways I didn't realize at the time, but appreciate now. I especially thank Anita and Kiran (as well as the Manne family). I still feel Anita is the only person in the world who understands the utter torture that is (was) the Ph.D. dissertation. She has seen more of my tears than anyone in Albuquerque, and I appreciate her friendship. Kiran's presence has always given me a sense of calm and often makes me reflect upon what is really important – maintaining life, without superficiality, ego and selfishness. Every time I was sick, every time I was hurt, every time I was sad, Daniel M. was there. He is truly a great friend. To my crazy Peruvian momma, Flor, and my beautiful friend, Roya. You girls really helped me on the big day and I will be there for both of you when you have yours! To friends who don't know why in the world I would pursue this but still think it's "cool", thanks for believing in me.

I reserve the last important bit of thanks for my immediate family. When others criticized my choice to pursue advanced academics, they have defended me, even without knowing what in the world it is I actually do. (Come to think of it, I haven't exactly figured this out myself.) So I thank my parents, Diane and Eddie, for their faith in me and allowing me to be as ambitious as I wanted my entire life. Love y'all!

I dedicate this dissertation to my baby brother, whose unfortunate death is a reminder to appreciate and celebrate my own. I am grateful for the 27 years I knew you and I hope you are as proud of me as I always have been of you.

"If we knew what it was we were doing, it would not be called research, would it?" - Albert Einstein

SYNTHESIS AND EVALUATION OF RARE-EARTH DOPED GLASSES AND CRYSTALS FOR OPTICAL REFRIGERATION

BY

WENDY PATTERSON

ABSTRACT OF DISSERTATION

Submitted in Partial Fulfillment of the
Requirements for the Degree of

Doctor of Philosophy

Optical Science and Engineering

The University of New Mexico
Albuquerque, New Mexico

December, 2009

SYNTHESIS AND EVALUATION OF RARE-EARTH DOPED GLASSES AND CRYSTALS FOR OPTICAL REFRIGERATION

by

Wendy Patterson

B.S., THE UNIVERSITY OF ALABAMA IN HUNTSVILLE, 2000
M.S., THE UNIVERSITY OF ALABAMA IN HUNTSVILLE, 2002
M.S., THE UNIVERSITY OF NEW MEXICO, 2008

Ph.D., OPTICAL SCIENCE AND ENGINEERING, THE UNIVERSITY OF NEW MEXICO, 2009

ABSTRACT

This research focused on developing and characterizing rare-earth doped, solid-state materials for laser cooling. In particular, the work targeted the optimization of the laser-cooling efficiency in Yb^{3+} and Tm^{3+} doped fluorides. The first instance of laser-induced cooling in a Tm^{3+}-doped crystal, BaY_2F_8 was reported. Cooling by 3 degrees Kelvin below ambient temperature was obtained in a single-pass pump geometry at $\lambda = 1855$ nm. Protocols were developed for materials synthesis and purification which can be applied to each component of ZBLANI:Yb^{3+}/Tm^{3+} ($ZrF_4 - BaF_2 - LaF_3 - AlF_3 - NaF - InF_3$: YbF_3/TmF_3) glass to enable a material with significantly reduced transition-metal impurities. A method for OH^- impurity removal and ultra-drying of the metal fluorides was also improved upon. Several characterization tools were used to quantitatively and qualitatively verify purity, including inductively-coupled plasma mass spectrometry

(ICP-MS). Here we found a more than 600-fold reduction in transition-metal impurities in a $ZrCl_2O$ solution. A non-contact spectroscopic technique for the measurement of laser-induced temperature changes in solids was developed. Two-band differential luminescence thermometry (TBDLT) achieved a sensitivity of ~7 mK and enabled precise measurement of the zero-crossing temperature and net quantum efficiency. Several Yb^{3+}-doped ZBLANI glasses fabricated from precursors of varying purity and by different processes were analyzed in detail by TBDLT. Laser-induced cooling was observed at room temperature for several of the materials. A net quantum efficiency of 97.39±0.01% at 238 K was found for the best ZBLANI:1%Yb^{3+} laser-cooling sample produced from purified metal-fluoride precursors, and proved competitive with the best commercially procured material. The TBDLT technique enabled rapid and sensitive benchmarking of laser-cooling materials and provided critical feedback to the development and optimization of high-performance optical cryocooler materials. Also presented is an efficient and numerically stable method to calculate time-dependent, laser-induced temperature distributions in solids, including a detailed description of the computational procedure and its implementation. The model accurately predicted the zero-crossing temperature, the net quantum efficiency, and the functional shape of the transients, based on input parameters such as luminescence spectra, dopant concentration, pump properties, and several well-characterized material properties.

TABLE OF CONTENTS

Chapter 1

Introduction

Historical overview of laser cooling and ZBLAN glass

In 1929 lasers had not yet been invented, but the concept of using light to cool solid objects was proposed by German physicist Peter Pringsheim [1]. His idea of a "cooling cycle" was based on the principle of fluorescence. Counterintuitive to the idea that radiation causes materials to heat is this concept of laser induced cooling, also referred to as optical refrigeration. For most materials, the application of intense radiation causes heating, even damage, such as is the case of lasers used to vaporize biological material and to cut metal. Optical refrigeration occurs when a material emits photons of higher average energy than those it absorbs. In the case of a solid, the extra energy comes from the absorption of phonons. In essence, heat energy is converted into light energy and carried out of the sample. This process is described in more detail in the Laser Cooling Fundamentals section of this manuscript as well as in the comprehensive book on laser cooling by Epstein and Sheik-Bahae [2].

Although it was initially thought that anti-Stokes fluorescence violated the second law of thermodynamics, Landau disproved this by assigning entropy to radiation [3]. Landau showed that entropy of a radiation field increases proportionally to its frequency bandwidth and the solid angle through which it propagates. In the case of laser cooling, the incident pump light is a laser which has a small bandwidth and is highly directional,

having almost no entropy. The fluorescence emitted, however, is considered broadband and omni-directional, therefore having large entropy. During laser cooling, incident laser light is converted into isotropic and broadband fluorescence, and we have therefore conserved the second law of thermodynamics. Application of the second and third laws of thermodynamics to the laser cooling process can be used to derive a fundamental limit of cooling. It was calculated that an upper limit of 20% of the pump radiation could be converted to cooling power given an impurity-free material [4].

Although the first successful attempt to apply these principles to experiment produced a mere 0.3 K of cooling [5], great success has recently been made where a YLF:Yb^{3+} crystal was cooled to 164 K and is predicted to cool as low as 105 K [6]. Many glasses and crystals doped with various rare-earth ions have shown laser cooling, with a comprehensive summary given Table 1. Rare earth doped ZBLAN glass, the workhorse of the laser cooling hosts, was previously commercially available in reasonably high purity and has favorable properties for laser cooling. Such glasses are no longer commercially available, necessitating the development of ultra-pure, rare earth doped, laser cooling grade ZBLAN for this research. These heavy-metal fluoride glasses were first discovered by Poulain et al. [7] who reported glass formation for a composition of 50% ZrF_4 – 25% BaF_2 – 25% NaF (mol%) in the mid 1970s. From these early results, ZBLAN glasses were developed by patient experimental trial and error. A relatively stable composition was determined to be around 53% ZrF_4 – 20% BaF_2 – 4% LaF_3 – 3% AlF_3 – 20% NaF. This is often referred to as the "standard" ZBLAN composition. Rare earth ions such as TmF_3 or YbF_3 can substitute for LaF_3 in the ZBLAN host and enable a variety of optical applications. Pure ZrF_4 does not exist in the vitreous form, and glass

modifiers such as NaF or BaF_2 are needed to provide charge neutrality in the interstices of the network. The NaF acts as a stabilizer reducing the tendency to crystallize. The addition of in situ oxidizers, such as InF_3, to ZBLAN is required in reducing atmospheres. However, these modifiers tend to decrease the glass stability. InF_3 concentrations of up to 2.5 mol% have been found to be effective in preventing the formation of black precipitates, which are recognized as reduced ZrF_4 species, while still allowing the formation of crystal-free glasses using standard melting techniques [8]. This modified ZBLANI glass was the focus of this research.

Table 1 Summary of rare-earth doped glasses and crystals that have exhibited laser induced cooling.

Dopant	Glasses	Crystals
Yb^{3+}	ZBLAN [5],[60]-[64]	YAG [73]
	BIGaZYT [65][66]	Y_2SiO_5 [73]
	CNBZn [65][66]	KPb_2Cl_5 [66]
	ABCYS [67]	LiY_2F_8 [75],[39]
		$KGd(WO_4)_2$ [37]
		$KY(WO_4)_2$ [72]
		BaY_2F_8 [74]
Tm^{3+}	ZBLAN [68]-[40]	BaY_2F_8 [76][77]
Er^{3+}	CNBZn [70][71]	KPb_2Cl_5 [70] [71]

Laser cooling fundamentals

The laser-cooling cycle is illustrated in Figure 1 (for the example of ZBLAN:Yb^{3+}) and begins when the properly tuned pump laser excites the dopant atoms from the top of the ground state multiplet to the bottom of the excited state multiplet. The

atoms thermalize within the upper and lower multiplets by absorbing vibrational energy (or phonons) from the host material. This thermalization process is represented in Figure 1 by the dashed, curved lines in the upper and lower multiplets. When an atom absorbs energy, it reaches an excited state. The new state is unstable, and the molecule must lose the extra energy. The atoms decay through fluorescence at an average energy greater than that of the pump. This process is known as anti-Stokes fluorescence. Therefore, by interacting with the molecular vibrations of the host, the Yb^{3+} ion can extract extra energy from the material. If emitted radiation contains more energy than was absorbed from the laser, the target loses energy and becomes colder. By repeating this process, the solid material sheds more and more thermal energy, leaving it cooler than its original state.
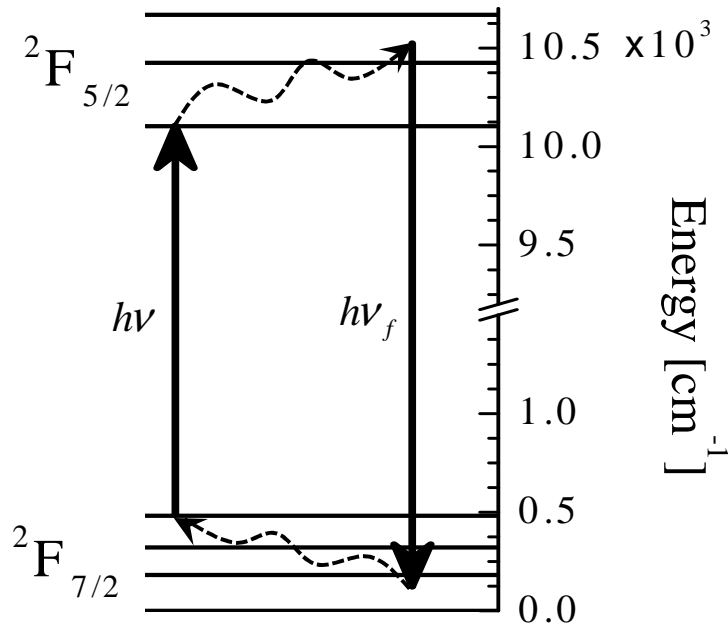
Figure 1   Schematic of energy levels in Yb^{3+}-doped ZBLAN showing the ideal case of laser cooling occurring between the two multiplets of Yb^{3+}. The dopant is excited by the pump laser at frequency ν from the top of the ground state multiplet ($^2F_{7/2}$) to the bottom of the excited state multiplet ($^2F_{5/2}$). Thermalization in both the upper and lower

multiplets (represented by the curved, dashed arrows) absorbs vibrational energy from the host. The energy emitted via fluorescence, $E_f = h\nu_f$, is greater than that absorbed and thereby the material is cooled.

Anti-Stokes fluorescence is a general process and has been observed in different states of matter such as organic laser dyes in an alcohol solution [9] and also dilute gases, where the de-exciting collision cross section is small [10]. Laser cooling in gases is defined by a reduction in translational kinetic energy versus a reduction in average thermal vibrations of the host material atoms, as is the case with solid state laser cooling. One may also use energy conservation to explain the heat loss from the target against the energy gain of the radiation. This applies to both cooling of solids and Doppler cooling of atoms. Solid state laser cooling (herein referred to as either laser cooling, laser induced cooling or optical refrigeration) involves excitation of an absorption band by a laser beam. Anti-Stokes fluorescence refers to the condition when significant absorption occurs at wavelengths longer than the average fluorescence energy. As an example, Figure 2 shows the absorption and emission spectra for a BaY_2F_8:Tm^{3+} crystal in E//b orientation. If the glass is illuminated in this overlapping wavelength region (hatched area), it will potentially emit photons of higher energy on average, than those it absorbs and the sample is cooled.
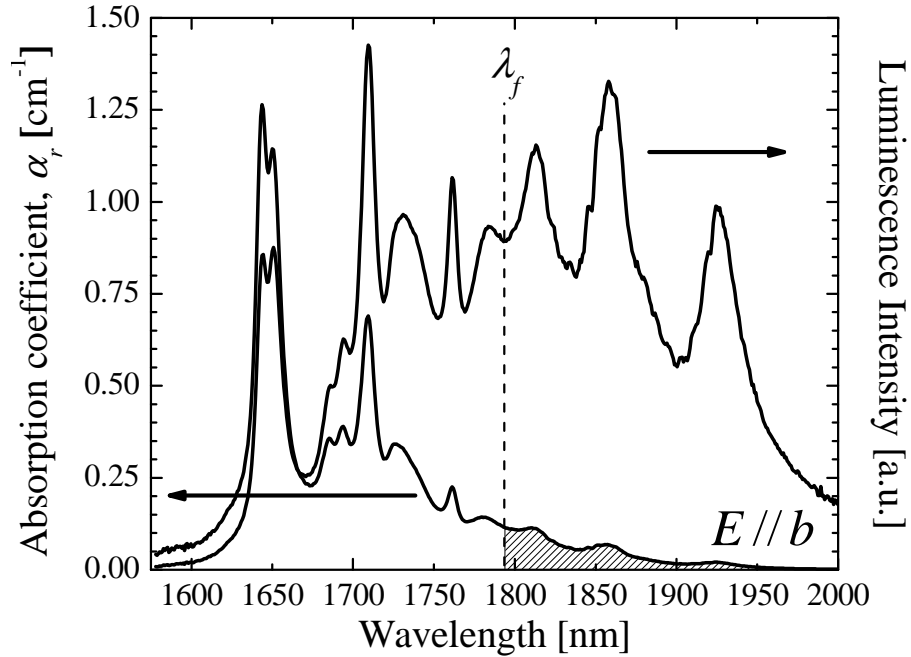
Figure 2 Absorption coefficient (left axis) overlapped with the luminescence intensity (right axis) for a BaY_2F_8:1.2% Tm^{3+} crystal at room temperature, oriented such that E//b. The hatched area is the "cooling tail", that is, the region that is probed for laser induced cooling. The dotted vertical line indicates the mean luminescence wavelength, $\lambda_f = 1793\,nm$. Pumping at wavelengths greater than λ_f will result in cooling for a sample exhibiting anti-Stokes fluorescence.

In order to understand why a material exhibiting anti-Stokes fluorescence is able to cool, we must also consider the timescales for the processes occurring in the excited state. For rare earth ions embedded in glass, absorption of phonons in the excited state happens quickly (on the order of ps [11]) compared to the timescale for radiative optical transitions (ms). This means that for any wavelength used to excite the dopant transition, the population distribution in the upper multiplet, where the spacing for the crystal-field levels is small (~200 cm^{-1}) relative to kT, reaches a local thermal equilibrium before relaxing to the ground state multiplet [12].

For this laser-cooling process, we can define an efficiency to tell us how efficient this cooling cycle is. This laser cooling efficiency is defined as [13],

$$\eta_{cool} = \frac{\eta\lambda - \lambda_f}{\lambda_f}, \tag{1}$$

where η is the net quantum efficiency of the rare-earth excited state containing all processes which quench the excited state of the dopant ion and λ and λ_f are the pump and mean fluorescence wavelengths, respectively. η is defined as

$$\eta(\lambda_p, T) = \eta_{abs}\eta_{ext}, \tag{2}$$

where η_{ext} describes the efficiency with which an excited ion produces a luminescence photon that escapes from the sample. The absorption efficiency, $\eta_{abs} = \alpha_r(\lambda)/(\alpha_r(\lambda) + \alpha_b)$, accounts for the fraction of excited photons that are engaged in cooling, where $\alpha_r(\lambda)$ is the resonant (e.g. Yb^{3+}) absorption at a given wavelength and α_b is the background absorption of the material, typically assumed to be independent of pump wavelength and temperature. Note that η is a function of both temperature and pump wavelength, largely through the absorption term, η_{abs}, but also due to the spectral overlap between the rare-earth ion emission and the impurity absorption. Further details regarding η have been covered extensively in the publication "Measurement of solid-state optical refrigeration by two-band differential luminescence thermometry", which is reproduced as Chapter 5 of this document. From Eq.(1), we see that as the laser input is tuned to longer wavelengths, the efficiency of the cooling process increases. This increase in cooling efficiency at longer wavelengths is offset by the fact that there is less dopant absorption as we move to longer wavelengths (see Figure 2), due to the thermal distribution of the ground state population. Additionally, parasitic background absorption (α_b) due to impurities further limits the desirable pump wavelength range. There exists

an optimal pump wavelength for a given temperature where these two cases are optimized. This is illustrated inFigure 3 where an optimal pump wavelength for a BaY_2F_8:Tm^{3+} crystal at room temperature is found to be ~1860 nm. Also, as the sample temperature decreases, absorption in the long wavelength tail will decrease due to reduced thermal broadening. As the temperature is lowered, the red shifting of the λ_f and the reduction of the resonant absorption (α_r) reduce the cooling efficiency. Therefore, as the sample is cooled, the optimal pump wavelength would also need to be decreased to maintain an optimal cooling efficiency. Hence, without a tunable pump source, optimal cooling could not be achieved throughout a cooling run from ambient down to low temperatures. There is a critical sample temperature where the heating and cooling are balanced. Here, $\eta_{cool} = 0$ and we can then determine η which is a qualitative measure of sample purity. Evaluation of laser cooling materials developed and synthesized at LANL is the focus of the publication "Preparation and characterization of high-purity metal fluorides for photonic applications", Chapter 3 of this document.
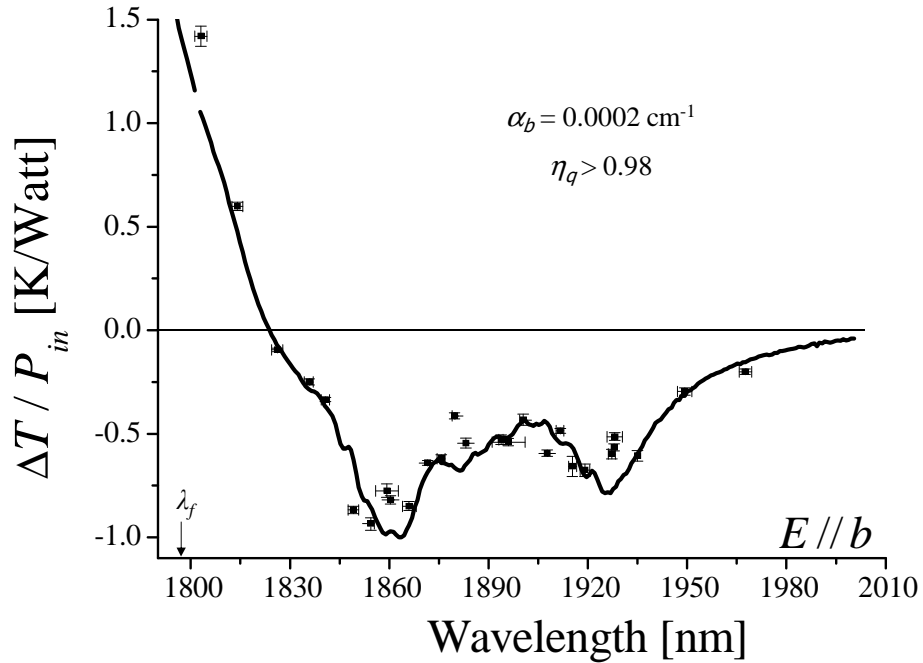
Figure 3 Change in temperature, ΔT (relative to a reference sample), normalized to input pump power, P_{in}, as a function of pump wavelength, λ, for a BaY_2F_8:1.2%Tm^{3+} crystal at room temperature, pumped in the E//b orientation. Here we are probing the "cooling tail" shown as the hatched region of Figure 2. Data points below the horizontal line indicate net cooling. The solid line is a fit to the data, described in the publication "Anti-Stokes luminescence cooling of Tm^{3+}-doped BaY_2F_8", reproduced as Chapter 2 of this document below. At some wavelength longer than λ_f, cooling begins and continues until background absorption (α_b) overwhelms the cooling at longer wavelengths.

Additionally, from Eq.(1) we can see that η_{cool} scales inversely with the dopant energy gap ($\Delta E = h\nu_f - h\nu$), giving a bit of insight into the desirable properties of a dopant ion for laser cooling. This is discussed more thoroughly in the Materials Selection section. Ultimately, cooling is limited by the fact that as we cool to lower temperatures, population in the manifolds is decreased due to the Boltzmann distribution. Throughout the remainder of this manuscript, the circumstances and necessary material characteristics desirable for optimizing laser cooling are described. This can be accomplished with

9

engineering techniques (with a few examples given in Figure 4), while the emphasis in

this research is in optimizing the laser cooling material.
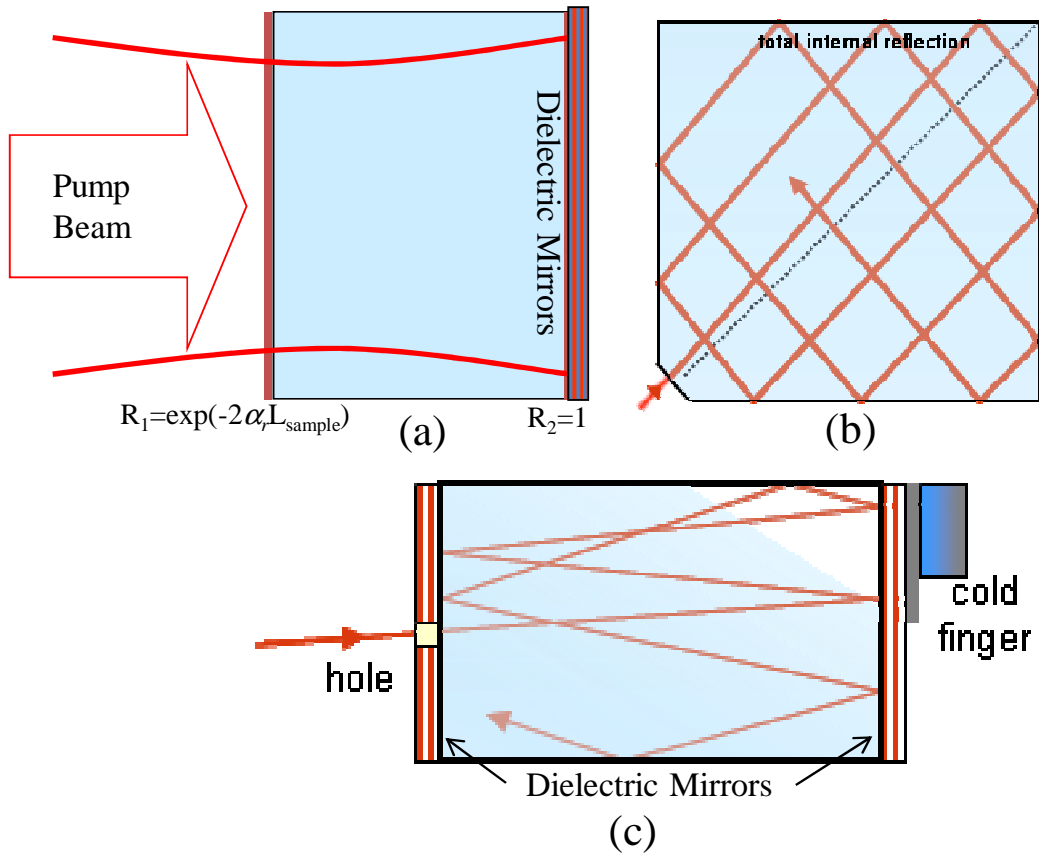
Figure 4 Engineering tactics designed to optimize the cooling power, P_{cool}, from a sample (blue) by increasing the absorption length, $\alpha_r L_{sample}$. The red lines represent the pump beam trajectories in three different schemes which have been employed to increase the absorbed power (P_{abs} from Eq.(3)). (a) Cavity enhanced cooling whereby the sample is contained in a resonator. (b) A monolithic optical maze, trapping incident light via total internal reflection. (c) High quality dielectric mirrors trap incident pump light fed through a small hole in a non-resonant cavity.

Motivation

Fluoride crystals and glasses are of interest to a wide range of photonic applications including optical fibers for high power or long-haul transmission [13]-[15], host materials for lasers and optical amplifiers [14],[16]-[19], scintillators [20],[21], upconversion phosphors [22], and optical refrigerators [2]. These applications take advantage of the high band gap energy and/or the low phonon energies (typically < 500 cm^{-1}) of fluorides. Specifically, fluoride-based fibers find application in low-loss communication links, CO_2 laser transmission for medical applications, thermal imaging and remote temperature monitoring and gas sensing [15]. Ultrapure fluorides are also needed for bulk optics for deep ultraviolet (UV) photolithography [23]. Field-deployable thorium nuclear clocks would also greatly benefit from pure fluoride precursors. These are potentially capable of $>1,000$ times higher accuracy over current atomic clocks used in GPS navigation systems [24]. One current limitation is residual absorption in the vacuum UV, which degrade the performance by reducing the transmittance near the 7.6 eV transition energy of thorium. The preparation of ultra-pure binary fluorides is therefore critical to enabling the desired performance of many fluoride optical materials.

One prominent advantage ZBLAN has over other glasses (such as silica) is superior infrared transmittance, covering a broad spectral range from 0.25 µm – 7 µm. Fluoride fibers have received the most attention for low-loss telecommunication applications because the theoretical limit for Rayleigh scattering is considerably lower than for silica-based glasses. This is due both to a higher energy UV absorption edge and better IR transparency. This spectral range can be extended even further into the IR by substitution of Hf for Zr, as well as by adding InF$_3$. Other characteristics that make ZBLAN attractive are its low refractive index, low dispersion, low phonon energy, and

low loss. In fact, ZBLAN has a theoretical attenuation coefficient of 0.002 db/km at 2.6 µm (compared to silica, given that the state-of-the-art is the Corning SMF-28 fiber, having 0.25 db/km attenuation at 1.55 µm). However, due to impurities and small crystallites [25], this low attenuation coefficient has not been achieved to date. These impurities are identified as transition metals (TMs) and hydroxyl ions, which have strong optical absorptions in the near IR and UV spectral regions [26]. In optical refrigerators, the impurity absorptions non-radiatively quench the optical excitation and cause unwanted heating that limits the laser-cooling performance (discussed in more detail in the Role of Impurities section). For optical refrigerators based on ZBLAN it was estimated, for example, that TM and OH^- impurities in excess of ~100 parts-per-billion (ppb) severely compromise the material performance [27]. Other applications have similarly stringent purity requirements. To date, the best commercially available ZBLAN glasses contain parts-per-million (ppm) impurity levels, which are inadequate in order to achieve the desired cryogenic performance. This is the primary motivation behind the materials synthesis development discussed in Chapter 3.

The principal application of laser cooling grade glasses or crystals, such as ZBLAN, is the realization of an all solid state optical cooler. Such a device would consist of a small diode laser used to excite a specially designed material in thermal contact with the load to be cooled. The primary application would be to cool radiation detectors and other sensitive electronic devices to cryogenic temperatures on earth, but especially in space [28] and detectors that have interband versus intersubband transitions. Such a solid state cooling device would be advantageous over current methods of cooling these electronics given that they (1) are vibration free, (2) are compact, given that sub-mm diode lasers

already exist, allowing a device having < 1 cm^3 volume and thus having a low total system mass, (3) have no fluids or moving parts, (4) have a potentially extremely long lifetime, due the long lifetime of laser diodes, (5) allow for possible remote laser pumping, (6) can withstand high g-forces, (7) do not require cryogenic fluids, (8) have a potential to cool to the ~100 K range, (9) use only photons as the cooling mechanism, no electrons, thus no electronic noise, (10) can withstand a high temperature environment, and (11) are low cost to manufacture.

Compared with thermoelectric coolers, solid state optical refrigeration devices would be more efficient when the difference between the hot and cold reservoir is large or below 190 K, where Peltier devices become severely inefficient [29]. The electrical connections required in Peltier devices limit both their reliability and the temperature differential at which they can operate. Although the majority of laser cooling experiments in the condensed phase to date have been performed at room temperature, applications where this form of cooling is likely to be more competitive versus other methods are predominately at low temperatures.

Yet another interesting potential application of solid state optical refrigeration might include cooling of interferometric gravitational wave detectors for the laser interferometer gravitational wave observatory (LIGO). Thermal noise is the current main limitation, as the project moves towards a low temperature system in order to improve the overall sensitivity curve of the detectors. Laser cooling could be used to obtain local cooling of the flexural points of the suspension wires of the interferometer mirrors, without adding any seismic noise [30],[31]. The cooling of amplifiers in MEMS gyroscopes for missile guidance systems is also a prospective application [32],[33] as

well as cooling of imaging sensors and quantum dot IR photodetectors [34]. The idea of creating a thermally balanced laser has been proposed by Bowman [35], whereby the heat produced by a laser gain material during lasing may be offset by the cooling from anti-Stokes fluorescence. This is feasible given that many laser cooling materials are also laser gain mediums. High critical temperature superconductors, such as YBCO [36], as well as compact SQUID magnetometers for geophysical and biomedical sensing might also benefit from application of an optical refrigerator.

Materials selection

Although a number of different types of materials are candidates for laser cooling in the condensed phase, the most successful combination to date involves rare-earth ions embedded in a transparent solid host (see Table 1). To achieve cooling, an appropriate ion embedded in a transparent host with minimal impurities is required. This section will discuss the ion and additional host properties required for laser cooling. Several groups have tried to find other materials suitable for cooling but even those which show promise from analysis of their absorption and emission spectra have either exhibited too low a quantum efficiency, or have excessive background absorption due to impurities [37].

The primary goal of this research was to develop a material capable of laser cooling to cryogenic temperatures. Although much effort has been dedicated to a number of engineering techniques which can be used to increase the absorbed power, P_{abs} (see Figure 4), this research was the first to explore material optimization to effect the largest temperature drop, ΔT, possible. The cooling power is given as,

$$P_{cool} = \eta_{cool} P_{abs},\tag{3}$$

where η_{cool} is defined above in Eq.(1) and P_{abs} is the absorbed power. In order to maximize ΔT (which is proportional to P_{cool}), we primarily seek to increase η_{cool}. Engineering methods used to increase the $P_{abs} = P_{in}[1-\exp((\alpha_b + \alpha_R)L_{sample})]$, via increasing the absorption length (αL_{sample}) have included, (1) shaping the material into a fiber [38], (2) making the sample a resonant [39] or non-resonant cavity [69], (3) trapping the light via total internal reflection [Figure 4 (b)], or (4) placing the cooling sample directly within a laser cavity [40], as summarized in Figure 4. The remainder of this section will outline material requirements for optimization of η_{cool}.

An ideal dopant-host pair should allow for effective ion-phonon coupling, which otherwise should not be large enough to result in multi-phonon relaxation. The energy gap law states that the non-radiative, multi-phonon emission rate, W_{nr} is inversely proportional to the exponential of energy difference (ΔE) between the excited and ground states,

$$W_{nr} \propto W_o \, e^{-a\,\Delta E}. \tag{4}$$

Here, W_o is a characteristic of the host material and is temperature dependent, ΔE is the energy gap of the dopant ion, and a is proportional to the phonon energy of the host. Figure 5 is a logarithmic plot of the non-radiative decay rate (Eq.(4)) for several potential host materials, as a function of ΔE [42]. Also shown are the absorption spectra for the relevant laser cooling transitions: ${}^3H_6 \rightarrow {}^3F_4$ for Tm^{3+} and ${}^3F_{7/2} \rightarrow {}^3F_{5/2}$ for Yb^{3+}. From Eq.(4) and Figure 5, we see that dopants with smaller energy gaps (Tm^{3+}) will generally be subject to higher non-radiative decay rates, due to more potential for interaction with host phonon modes. This dependence is due to phonon energy distributions that vary with

material composition and symmetry. For this reason, low phonon energy of the host material is desirable for laser cooling. As an example, the phonon energies in ZBLAN are significantly lower than in silica, thus a greater number of phonons need to interact simultaneously to thermally de-excite the electronic excited state of the dopant. This makes multi-phonon transitions, which reduce the optical quantum efficiency, much less likely in a ZBLAN host than in silica [43]. Other host materials, such as BIG (BaF_2-InF_3-GaF_3) which have transmission extending further into the IR, will have even lower phonon energy than ZBLAN [44].
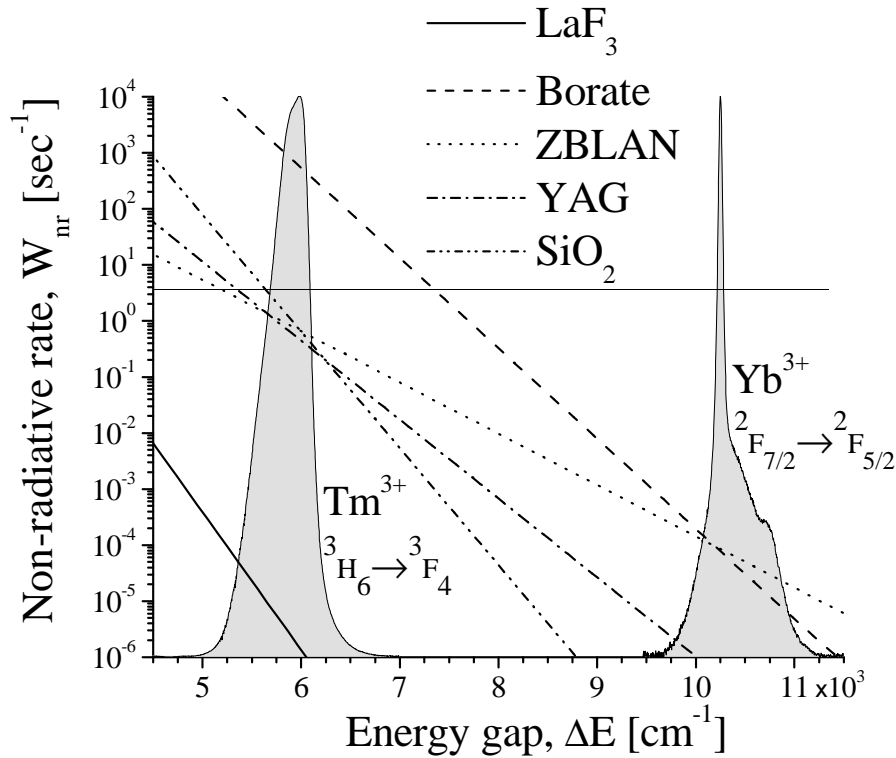
Figure 5 The relationship between the energy gap of the rare earth dopant (shown here with the absorption spectra of Tm^{3+} and Yb^{3+}) and the non-radiative decay rate, as given in Eq.(4) for various potential host materials. Here we can see, for example, that a ZBLAN host doped with Yb^{3+} will exhibit a lower non-radiative decay rate and thus a larger quantum efficiency compared to the same material doped with Tm^{3+}. The horizontal line represents the maximum non-radiative rate for cooling to occur at room temperature (assuming no background absorption). From this figure, we see that a Borate:Yb^{3+} sample has potential to cool whereas the efficiency in a Borate:Tm^{3+} sample is too low for laser cooling.

In order to allow for more cooling at lower temperatures, a narrow Stark splitting of the ground state multiplet is desired. A small ground state splitting results in a large population density in the upper Stark sublevels. This allows for a lower zero-crossing temperature, T_{ZCT} (also referred to as minimum achievable temperature), however, lower efficiency at room temperature. Other desirable properties of a laser cooling host material include: (1) high thermal conductivity, allowing for fast thermal diffusion, (2) low background absorption, as impurity/pump interactions reduce the cooling efficiency (discussed in detail in the Role of Impurities section), (3) high material hardness, which allows for better polish and direct deposition of optical coatings, (4) large absorption cross-section, allowing for a large absorption efficiency thus large η_{cool}, and (5) low thermal emissivity, giving higher transparency at thermal wavelengths (far-infrared) for a material less susceptible to radiative heat loading.

In addition to these material properties, structural properties can affect the degree of laser cooling. Many glasses and crystals have exhibited laser cooling. In glasses there is no long range order, thus the Stark splitting is not homogeneous as in a crystalline material where each rare-earth ion experiences an essentially identical Stark interaction. In the inhomogeneously broadened case of the glass, oscillator strength is not used efficiently; in a crystal, the oscillator strength is concentrated, resulting in sharp absorption peaks. The difficulty imposed by the more discrete transition energies, and regular structure, is that phonon energies supported in the crystal must match the difference in energy between transitions if absorption at one wavelength is to lead to emission at another, as required for cooling to occur.

When selecting a laser cooling material, the choice of dopant is equally important as the choice of host material. Typically, rare earth ions are chosen as they provide a broadened two level system with high quantum efficiency, as required. For this reason, materials that lase make good candidates for laser cooling, in general. The optically active *4f* electrons are well shielded from the surrounding environment by the filled *5s* and *5p* shells and as a consequence, the interaction between the electrons and the surrounding medium lattice phonons is very weak. This results in a narrow spread of the Stark structure (compared to transition metals, which involve *3d* electrons shielded only by two outer *4s* electrons) and thus sharper linewidths and greater absorption. Due to sufficient shielding, the spectra do not exhibit large variations from host to host, and many excited states have relatively low non-radiative decay rates. The rare earths of interest are the lanthanides which are chemical elements characterized by the filling of the *4f* shell. They are in the sixth period of the periodic table with atomic numbers varying from 58 to 71. The *4f* electrons have almost no contribution to the chemical valence, therefore the atom can easily lose three electrons, usually $5d^1$ and $6s^2$ to attain their most stable oxidization state as trivalent ions. Due to the practical experimental limitations and availability of tunable sources and spectrometers, practical choices for rare-earth dopants include Yb^{3+}, Tm^{3+}, and Er^{3+}.

According to the definition of the cooling efficiency (Eq.(1)), dopant ions with larger energy gaps will produce more efficient cooling. The energy levels for the two main dopant ions of interest, Tm^{3+} and Yb^{3+} are shown in Figure 6 where the primary transition used for laser cooling is emphasized. Thus doping with Tm^{3+} (having an energy gap of ~0.7 eV, versus ~1.25 eV for Yb^{3+}), for example should be nearly twice as

efficient. However, Yb^{3+} only has one excited state manifold, $^2F_{5/2}$. Therefore, excited state absorption (ESA) and cross-relaxation via concentration quenching are not issues. Both of these processes typically involve non-radiative energy transfers detrimental to laser cooling. ESA is possible for ions with multiple electronic levels, such as Er^{3+} or Tm^{3+}, whereas it is not possible for Yb^{3+}. Given the trade-offs between Tm^{3+} and Yb^{3+} discussed in this section, the superior dopant for laser cooling has yet to be established and research continues using both dopants.
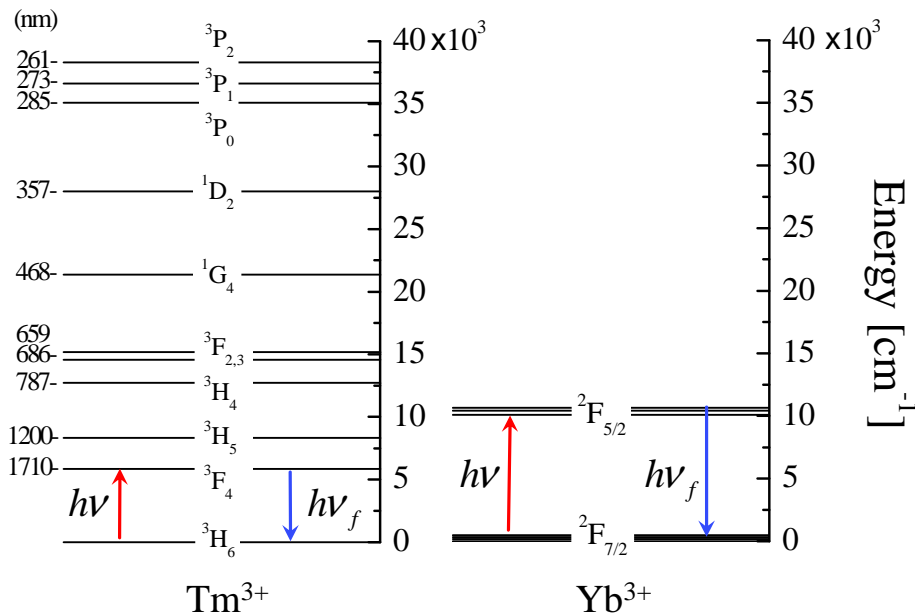
Figure 6 Calculated energy levels for ZBLAN:Tm^{3+} and ZBLAN:Yb^{3+}. The red arrows indicate the transition that is typically pumped to effect laser induced cooling. The blue arrows represent the anti-Stokes luminescence which carries away energy from host phonons enabling laser cooling. The ordinate axis for both systems are shown on equal scales for easy visual comparison. More detail on the $^2F_{7/2} \rightarrow {}^2F_{5/2}$ transition for Yb^{3+} is shown in Figure 1.

Role of impurities

In the context of laser cooling, an impurity is any species in the material that lowers the quantum efficiency of the excited state of the dopant ion. A great number of successful cooling cycles (each extracting only a few *kT* of heat) are required to compensate for each non-radiative event. A high quantum efficiency, indicating primarily radiative energy transfer, is therefore central to the operation of laser coolers. Competing processes that tend to introduce heating (and thus lower the cooling efficiency) are: (1) multi-phonon relaxation of the rare-earth excited state, (2) non-radiative energy transfer from the excited rare earth-ion to an nearby impurity, or (3) background absorption by an impurity.

The depopulation of an excited state can occur due to a radiative transition, where the energy is emitted as fluorescence, or by phonon assisted transitions, where the energy is taken up by the host material in the form of phonons. The lifetime of a metastable electronic state of a dopant ion can be reduced by decay processes which involve the simultaneous emission of several phonons. Such a process is a multi-phonon transition or relaxation. Multiple phonons are typically required for such transitions because the energy of a single phonon is not sufficient to match the difference in level energies. For example, multi-phonon relaxation of the $^3F_4$ excited state of the Tm^{3+} ion in a ZBLAN host would require ~ 6 phonons while multi-phonon relaxation of $^2F_{5/2}$ excited state of Yb^{3+} would require ~ 10 phonons for such a transition in the same host material. The process can be significantly reduced given the proper choice of a host material with low phonon energy (such as ZBLAN), as discussed in the Materials Selection section. In addition to this interaction between dopant and host phonon modes, multi-phonon relaxation can also occur due to excitation of impurities with high energy vibrational

modes or multi-relaxation processes following upconversion or cross-relaxation. Specifically, impurities with high energy vibrational modes can degrade material performance by introducing UV absorption enhancing multi-phonon relaxation rates of excited states [44], [45]. Any impurity with $\hbar \omega_{max} > 1000$ cm^{-1} can potentially introduce such a heat load that becomes competitive with optical cooling. Examples include oxygen-based impurities such as oxides, hydroxyl (OH$^-$) ions, and water as well as CO_2, C-H bonds and N-H bonds.

Transition metal (TM) ions have optical transitions in the UV and visible spectral regions [25], leading to undesired background absorption by direct absorption at the pump wavelength. Additionally, impurities can act as acceptors in a non-radiative energy transfer from the excited state of the dopant ion causing quenching of the rare earth excited state, even at trace levels [27], [44]. Examples include certain TMs as well as several rare-earth ions (Pr^{3+}, Sm^{3+}, Dy^{3+}, Ho^{3+}, Yb^{3+}, Er^{3+} and Tm^{3+}). For Yb^{3+}, impurities with optical absorption bands around 1 μm can act as acceptors in an energy transfer from the $^2F_{5/2}$ excited state followed by non-radiative relaxation of the excited impurity ion. Such impurities become particularly relevant as the dopant concentration is increased and energy migration through the dopant ions to those excitation traps becomes efficient. To illustrate this effect and determine which impurities are most deleterious to laser cooling, Figure 7 shows absorption cross-sections of several TMs adapted from France et al. [46] overlapped with the absorption spectra of Yb^{3+} and Tm^{3+} in ZBLAN. We can make several observations based on the spectral overlap between the dopant ion and these select TM ions. As compared to unwanted rare earths (which are likely present due to the difficulty in chemically separating similar species) transition metals are worst

for degrading cooling performance due to their comparatively large line widths, which overlap somewhat with the dopants. The rare earth impurities are not as problematic [47] due to their relatively narrow spectrum. The TMs will also lead to significant background absorption since the excitation pump source will also overlap with these ions. Here we can also see that a Tm^{3+} doped material might exhibit less heating from impurity absorption, as the spectral overlap is smaller compared with the overlap for Yb^{3+}. From this data, Hehlen et al. [27] concluded that the most problematic transition metals (in decreasing order of most to least problematic) include Cu^{2+}, Fe^{2+}, Co^{2+}, Ni^{2+}, V^{3+}, Ti^{3+}, and Cr^{3+}. They also calculated that in order to develop an all solid state cryocooler capable of laser cooling to 100 K, such transition metals and OH^- impurities would need to be reduced to 10 – 100 ppb total in the final host. In particular, they concluded that Cu^{2+} would have the most stringent requirement, and would need to be reduced to < 2 ppb. They estimated that even the best laser cooling glasses to date would require a further 20-30 fold reduction in impurities to achieve this goal. This finding was the basis for developing the capabilities that enable processing of ultra-pure ZBLAN glass at LANL. This process strategy is briefly discussed in the Fluoride Purification section and is compared to other methods of purifying the host material components. The details for the final purification strategy used can be found in the publication, "Preparation and Characterization of high-purity metal fluorides for photonic applications" reproduced as Chapter 3 of this document. Now that the most problematic impurities for laser cooling have been identified, a strategy for their removal can be explored as outlined in the following section, Fluoride Purification Methods.
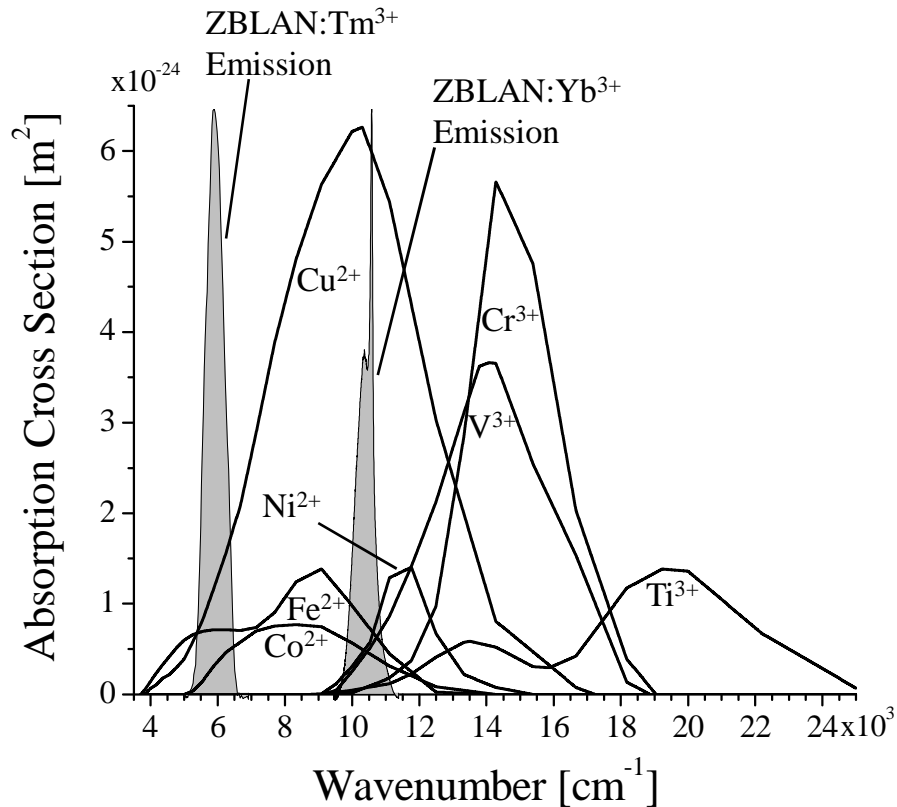
Figure 7 This figure illustrates the spectral overlap, and thus potential interaction or energy transfer between Tm^{3+} or Yb^{3+} ions with selected transition metal ions. All spectral data were taken at room temperature. The absorption cross sections of the transition metals were adapted from France et al.[46].

Fluoride purification methods

Many methods exist for reducing the TM impurities in some of the fluorides constituting ZBLAN glass, such as: (1) sublimation and distillation of ZrF_4, (2) normal freezing, (3) zone refining, (4) ion exchange and (5) re-crystallization [45],[48]. However, none of these methods reduce impurities to the desired ppb level, as fluorides are notoriously difficult to purify. Commercially prepared ZBLAN used for past laser cooling experiments utilized a clean-up approach whereby oxidizing methods were used

during glass synthesis to remove OH⁻ impurities. The use of CF_4, NF_3, SF_6, Cl_2, CCl_4, or O_2 reactive gas atmospheres during melting has been widely used [49],[50], however, such methods are not acceptable for many high purity glass applications such as laser cooling, as they re-contaminate the final glass with unwanted species. For example, the use of CCl_4 will result in the introduction of Cl⁻ impurities into the melt by the replacement of trace quantities of OH⁻ with Cl⁻ so that the anion stoichiometry is unknown. In other words, the glass fluoride stoichiometry would then be incomplete. The added Cl⁻ also produces a higher crystallization tendency and, in extreme cases, may lead to reduced resistance to attack from environmental moisture. Electrochemical purification of the fluoride melts was also previously performed as a clean-up method for the transition metals (TMs) [44]. However, this technique is not capable of reducing the impurities to the ppb regime required for efficient laser cooling. While the slow growth of fluoride *crystals* can reduce the concentration of some of these impurities, fluoride *glasses* generally contain all of the impurities that were present in the melt from which they were quenched. More recent developments in fluoride purification include vapor phase processes, which appear attractive due to the success of chemical vapor deposition (CVD) in purifying silica for fiber technology. Some preliminary results appear to be encouraging. However, the practical achievement of fluoride glasses through CVD appears difficult due to the high evaporation temperature of several of the fluoride glass components [51]-[53]. Although reasonable success has been reported in reducing TMs in ZrF_4, no strategy has been identified to reduce impurities to the desired levels for all components in ZBLAN glass. It is universally regarded that new synthesis processes are needed for the achievement of very pure ZBLAN glass.

In this research, we have developed a streamlined approach which targets undesirable TM ions in all components of ZBLANI:Yb^{3+}/Tm^{3+}. Our method utilizes a bottom-up approach, where we start with the purest precursors commercially available and further purify them before converting them to the appropriate fluoride. Our synthesis strategy focuses on purification and preparation of individual fluoride starting materials under well-defined, tightly-controlled atmospheric conditions before they are mixed to form ZBLANI glass. In this work, we aim to significantly reduce problematic TM impurities down to the ppb level using a well established technique, chelate assisted solvent extraction. Our approach is to exploit a single chelate/organic solvent system suitable for the individual purification of all ZBLANI:Yb^{3+}/Tm^{3+} components in order to minimize the development effort and to simplify processing, allowing future scale-up for producing larger quantities of materials. The system consisting of ammonium-pyrrolidine-dithio-carbamate (APDC) as the chelate and methyl-isobutyl-ketone (MIBK) as the organic solvent is well developed and used in analytical chemistry for heavy metal trace analysis [54]-[58]. Ling et al. used the APDC/MIBK system to reduce Co^{2+}, Ni^{2+}, and Cu^{2+} to < 5 ppb and Fe^{2+} to < 10 ppb in zirconium solutions [54]. The APDC/MIBK system is ideal for the removal of the specific TMs that are detrimental to laser cooling while not affecting the metal ions of the glass components. Solvent extraction uses a chelate that preferentially binds only to specific metal ions in the aqueous phase, forming a hydrophobic complex. The resulting metal-chelate complexes are extracted from the aqueous into a second, immiscible organic phase. By extracting only the aqueous phase, the desired metal ions are retained and the unwanted TM ions are removed with the organic phase. Although the ratio of metal ions extracted to the organic phase to those

metal ions in the aqueous phase is high for TM ions in the APDC/MIBK system [55],[57],[58], three sequential extraction steps were performed to ensure a nominal reduction of the target impurities by at least a factor of 10^3. Further details on these methods and the glasses produced for this research are contained in the article "Preparation and characterization of high-purity metal fluorides for photonic applications" (given as Chapter 3 of this document). In addition to the removal of TMs, this research also developed methods to remove OH^- and water from fluoride precursor materials. This is outlined in detail in Chapter 3 of this manuscript. These methods can be extended to purification of a variety of host glasses and crystals and is not limited to ZBLANI:Yb^{3+}/Tm^{3+}. Other materials of interest are currently under investigation, including the crystalline YLF:Yb^{3+} which has shown great potential [6].

Manuscript organization

The bulk of this document, Chapters 2-5, consists of peer-reviewed journal articles either published or in the process of submission to high-impact journals in optics and materials science. The purpose of this Introduction chapter was to relate all of these journal articles, and provide more details on important topics touched on throughout the various articles. Specifically, the motivation for this research and the materials selection sections have been expanded. Note that the citations within each chapter are referenced at the end of the given chapter, with each chapter having its own bibliography.

Much of the motivation behind this research lies in the unavailability of commercially available laser cooling grade materials. For this reason, we initially began to seek sources of rare-earth doped, pure host materials under development by other

research groups. One of our collaborators at the University of Pisa has the capability of a making a very high purity, high quality BaY_2F_8 crystal. The first paper given in Chapter 1 shows successful laser induced cooling for the first Tm^{3+}-doped crystal, BaY_2F_8. It was found that this material has similar favorable properties to ZBLAN, making it a good host material for laser cooling. However, due to limited availability and the need to control the strict purity requirements, it was deemed necessary to synthesize our own laser cooling grade materials. This lead to the research presented in Chapter 3, where capabilities were developed to synthesize and purity fluoride precursor materials for synthesis of ultra-pure, rare earth doped ZBLANI glass. This chapter provides all the details necessary to produce a laser-cooling grade glass. In developing a figure of merit for evaluating laser cooling materials, it was necessary that the method test an intrinsic property of the material, related at least qualitatively to the amount of impurities present in the material. This method must also be insensitive to surface preparation methods and re-absorption effects, sensitive to temperature changes as small as tens of mK, practical over a wide range of sample temperatures, and be relatively expedient. Two such interrelated figures of merit were selected, the zero crossing temperature, T_{ZCT} and the net quantum efficiency, η. An experimental method, two band differential luminescence thermometry (TBDLT), was developed to determine T_{ZCT} which can in turn, be used in conjunction with the temperature depended luminescence spectra to find η. Chapter 5, "Measurement of solid-state optical refrigeration by two-band differential luminescence thermometry" describes in detail how these two parameters were obtained. Given the feedback from this experiment, we were able to make several iterations of our ultra-pure laser cooling material, with each iteration resulting in improvement of the glass as described in

Chapters 3 and 5. During this TBDLT experiment, temperature dependent transients are recorded and analyzed to determine T_{ZCT}. In order to predict the functional form of the experimental data, it was necessary to correctly model the thermal processes occurring in the ZBLANI:Yb^{3+} system. This is presented in Chapter 4, "Model of laser-induced temperature change in solid-state optical refrigerators". This model can be easily adapted to other glass host materials, and could be extended to crystals as well. This work presents the first attempt to predict laser cooling transients, based on material and experimental parameters, before undertaking a costly and time consuming experiment.

REFERENCES

[1]   P. Pringsheim, "Zwei Bemerkungen über den Unterschied von Lumineszenz – und Temperaturstrahlung," Z. Phys. **57**, 739 (1929).

[2]   R. I. Epstein and M. Sheik-Bahae, eds., in *Optical Refrigeration. Science and Applications of Laser Cooling of Solids*, (Wiley, Weinheim, 2009), pp. 1-28.

[3]   L. Landau, "On the thermodynamics of photoluminescence," J. Phys. (Moscow) **10**, 503 (1946).

[4]   C. E. Mungan, "Radiation thermodynamics with applications to lasing and fluorescent cooling," Am. J. Phys **73** [4], 315-322 (2005).

[5]   R. I. Epstein, M. I. Buchwald, B. C. Edwards, T. R. Gosnell, and C. E. Mungan, "Observation of laser-induced fluorescent cooling of a solid," Nature, London **377**, 500-503 (1995).

[6]   D. V. Seletskiy, S. D. Melgaard, S. Bigotta, A. Di Lieto, M. Tonelli, R. I. Epstein, and M. Sheik-Bahae, "Demonstration of an Optical Cryocooler," in *Conference on Lasers and Electro-Optics/International Quantum Electronics Conference*, OSA Technical Digest (CD) (Optical Society of America, 2009), paper IPDA9.

[7]   M. Poulain, J. Lucas, and P. Brun, "Verred fluores au tetrafluorure de zirconium. Proproetes optiques d'un verre dope au Nd^{3+}," Mat. Res. Bull **10**, 243 (1975).

[8]   B. T. Hall, L. J. Andrews and R. C. Folweiler, "Method for preparing fluoride glasses," U.S. Patent 4,946,490 (1989).

[9]   C. Zander and K. Drexhage, "Cooling of a dye solution by anti-Stokes fluorescence," in *Advances in Photochemistry*, Vol. 20, D. C. Neckers, D. H. Volman, and G. V. Bunau, eds. (John Wiley, New York, 1995), pp. 59-68.

[10]   S. Chu, C. Cohen-Tannoudji, and W. D. Philips, Nobel Prize in Physics for the development of methods to cool and trap atoms with laser light (1997).

[11]   W. J. Miniscalo, in *Rare Earth Doped Fiber Lasers and Amplifiers*, M. J. F. Digonnet, ed., (Marcel Dekker, New York, USA, 1993).

[12]   J. T. Verdeyen, *Laser Electronics*, Prentice Hall Series in Solid State Physical Electronice, 3rd ed. (Prentice Hall, New Jersey, 1995).

[13]   M. Sheik-Bahae and R. I. Epstein, "Optical refrigeration," Nature Photonics **1**, 693–699 (2007).

[14]   S. Sudo, "Progress in Optical Fiber Amplifiers," in *Current Trends in Optical Amplifiers and their Applications*, T. P. Lee ed., (World Scientific, New Jersey, 1996), pp. 19-21.

[15]   T. G. Brown, "Optical fibers and fiber-optic communications," in *Fiber Optics Handbook: Fiber, devices and systems for optical communications*, M. Bass and E. W. Van Stryland, eds., (McGraw-Hill, NY, 2002), pp. 1-49.

[16]   S. Bedo, M. Pollnau, W. Luthy, and H. P. Weber, "Saturation of the 2.71 um laser output in erbium-doped ZBLAN fibers," Opt. Commun. **116,** 81–86 (1995).

[17]   X. Zhu and R. Jain, "Numerical analysis and experimental results of high-power Er/Pr:ZBLAN 2.7 um fiber lasers with different pumping designs," Applied Optics **45** [27], 20 (2006).

[18]   T. Sakamoto, M. Shimizu, M. Yamada, T. Kanamori, Y. Ohishi, Y. Terunuma, and S. Sudo, "35 dB gain Tm-doped ZBLAN fiber amplifier operating at 1.65 um," *Tech. Digest of CLEO/Pacific Rim* PD2.12, (July 1995).

[19]   B. Pedersen, W. J. Miniscalo, and R. S. Quimby, "Optimization of Pr^{3+}:ZBLAN fiber amplifiers," IEEE Photonics Technol. Lett **4** [5], 446-448 (1992).

[20]   D. F. Anderson, "Cerium fluoride: a scintillator for high-rate applications," Nucl. Instrum. Methods Phys. Res. **A287** [3], 606-612 (1990).

[21]   E. Auffray, D. Bouttet, I. Dafinei, J. Fay, P. Lecoq, J. A. Mares, M. Martini, G. Maze, F. Meinardi, B. Moine, "Cerium doped heavy metal fluoride glasses, a possible alternative for electromagnetic calorimetry," Instrum. Methods Phys. Res. **A380** [3], 524-536 (1996).

[22]   J. Freek Suijver, "Upconversion Phosphors," in *Luminescence: From Theory to Applications*, C. Ronda ed., (Wiley-VCH, Weinheim, 2008), pp. 133-175.

[23]   T. M. Bloomstein, M. W. Horn, M. Rothschild, R. R. Kunz, S. T. Palmacci and R. B. Goodman, "Lithography with 157 nm lasers," J. Vac. Sci. Technol. B **15**, 2112 (1997).

[24]   E. Peik and C. Tamm, "Nuclear laser spectroscopy of the 3.5 eV transition in Th-229," Euro-phys. Lett. **61**, 181 (2003).

[25]   K. Fujiura, S. Sakaguchi, Y. Ohishi and Y. Terumnuma, "Formation Reaction of ZrO_2 Scatterers in ZrF_4-Based Fluoride Fibers," J. Am. Ceram. Soc. **71**, 460 (1988).

[26]   S. Mitachi, T. Miyashita and T. Manabe, "Preparation of fluoride optical fibers for transmission in the mid-infrared," Physics and Chemistry of Glasses **23**, 196-201 (1982).

[27]   M. P. Hehlen, R. I. Epstein, and H. Inoue, "Model of laser cooling in the Yb^{3+}-doped fluorozirconate glass ZBLAN," Phys. Rev. B **75** [14], 144302 (2007).

[28]   B. C. Edwards, J. E. Anderson, R. I. Epstein, G. L. Mills and A. J. Mord, "Demonstration of a solid-state optical cooler: An approach to cryogenic refrigeration," Journal of Applied Physics **86**, 6489-6493 (1999).

[29]   R. Frey, F. Micheron, and J. P. Pocholle, "Comparison of Peltier and anti-Stokes optical coolings," J. Appl. Phys. **87**, 4489–4498 (2000).

[30]   T. Uchiyama, D. Tatsumi, T. Tomaru, M. E. Tobar, K. Kuroda, T. Suzuki, N. Sato, A. Yamamoto, T. Haruyama, T. Shintomi, "Cryogenic cooling of a sapphire mirror-suspension for interferometric gravitational wave detectors," Physics Letters A **242** [4-5], 211-214 (1998).

[31]   F. Bondu, J. Vinet, "Mirror thermal noise in interferometric gravitational-wave detectors," Physics Letters A **198** [2], 74-78 (1995).

[32]   V. K. Varadan and V. V. Varadan, "Microsensors, microelectromechanical systems (MEMS), and electronics for smart structures and systems," Smart Mater. Struct. **9**, 953-972 (2000).

[33]   W. P. Platt, B. R. Johnson, "Cryogenic inertial micro-electromechanical system (MEMS) device," U. S. Patent 6,487,864 (2002).

[34]   S. Tsao, H. Lim, W. Zhang, and M. Razeghi, "High operating temperature 320 x 256 middle-wavelength infrared focal plane array imaging based on an InAs/InGaAs/InAlAs/InP quantum dot infrared photodetector," Appl. Phys. Lett. **90**, 201109 (2007).

[35]   S. R. Bowman, "Lasers without internal heat generation," IEEE J. Quant. Elect. **35**, 115–122 (1999).

[36]   T. P. Sheahen, "Refrigeration," in *Introduction to high-temperature superconductivity* (Plenum Press, NY, 1994).

[37]   S. R. Bowman and C. E. Mungan, "New materials for optical cooling," App. Phys. B **B71**, 807 (2000).

[38]   T. R. Gosnell, "Laser cooling of a solid by 65 K starting from room temperature," Opt. Lett. **24**, 1041-1043 (1999).

[39]   D. Seletskiy, M. P. Hasselbeck, M. Sheik-Bahae, R. I. Epstein, S. Bigotta, and M. Tonelli, "Cooling of Yb:YLF using cavity enhanced resonant absorption," Proc. SPIE 6907, 69070B (2008).

[40]   C. W. Hoyt, W. Patterson, M. P. Hasselbeck, M. Sheik-Bahae, R. I. Epstein, J. Thiede, and D. Seletskiy, "Laser cooling thulium-doped glass by 24K from room temperature," Trends in Optics and Photonics **89**, QThL4 (2003).

[41]   B. Heeg, M. D. Stone, A. Khizhnyak, G. Rumbles, G. Mills, P. A. DeBarber, "Experimental demonstration of intracavity solid-state laser cooling of Yb^{3+}:ZrF_4-BaF_2-LaF_3-AlF_3-NaF glass," Phys. Rev. A **70**, 21401 (2004).

[42]   L. Wetenkamp, G. F. West, and H. Tobben, "Optical properties of rare earth-doped ZBLAN glasses," Journal of Non-Crystalline Solids **140**, 35-40 (1992).

[43]   B.M. Walsh, N.P. Barnes, "Comparison of Tm^{3+}:ZBLAN and Tm^{3+}:silica fiber lasers; Spectroscopy and tunable pulsed laser operation around 1.9 µm," App. Phys. B: Lasers and Optics **78** [3], 325-333 (2004).

[44]   D. R. MacFarlane, Z. Zhou and P. J. Newman, "Differential pulse voltammetry studies of heavy metal fluoride melts," Journal of Applied Electrochemistry **34**, 197–204 (2004).

[45]   B. E. Kinsman and R. Hanney, "Preparation and purification of metal fluorides for crystals and glasses," Adv. Matls. for Opt. and Elect. **5**, 109-115 (1995).

[46]   P. W. France, S. F. Carter, J. M. Parker, "Oxidation states of 3d transition metals in ZrF_4 glasses," Phys. Chem. Glasses **27**, 32 (1986).

[47]   P. Goldner and M. Mortier, "Effect of rare earth impurities on fluorescent cooling in ZBLAN glass," J. of Non-Cyrst.Solids **284** [1-3], 249-254 (2001).

[48]   D. R. MacFarlane, P. J. Newman and A. Voelkel, "Methods of purification of zirconium tetrafluoride for fluorozirconate glass," J. Am. Ceram. Soc. **85** [6], 1610-12 (2002).

[49]   A. M. Mailhot, A. Elyamani, and R. E. Riman, "Reactive atmosphere synthesis of sol-gel heavy metal fluoride glasses," J. Mater. Res. **7** [6], 1534-1540 (1992).

[50]   M. G. Drexhage, C. T. Moynihan, B. Bendow, E. Gbogi, K. K. Chung, and M. Boulos, "Influence of processing conditions on IR edge absorption in fluorohafnate and fluorozirconate glasses," Mater. Res. Bull **16**, 943-947 (1981).

[51]   M. Jardin, J. Guery, and C. Jacoboni, "Preparation in vapour state of fluoride glass components by a chemical vapour deposition process," J. Non-Cryst. Solids **184**, 204-208 (1995).

[52]   Y. Nishida, K. Fujiura, H. Sato, S. Sugawara, K. Kobayashi and S. Takahashi, "Preparation of ZBLAN fluoride glass particles by chemical vapor deposition process," Jpn. J. Appl. Phys. Part 2 **31** [12A], 1692-1694 (1992).

[53]   K. Fujiura, Y. Ohishi, M. Fujiki, T. Kanamori, S. Takahashi, "Process for the preparation of fluoride glass and process for the preparation of optical fiber perform using the fluoride glass," U.S. Patent 5,071,460 (1991).

[54]   Z. Ling, Z. Chengshan, D. Gaozian, and W. Kangkang, "ZrOCl$_2$ for fluoride glass preparation," J. Non-Cryst. Solids **140**, 331-334 (1992).

[55]   H. Malissa, E. Schöffmann, "Über die Verwendung von substituierten Dithiocarbamaten in der Mikroanalyse," Mikrochim. Acta **1**, 187 (1955).

[56]   J. D. Kinrade, J. C. Van Loon, "Solvent extraction for use with flame atomic absorption spectrometry," Anal. Chem. **46**, 1894 (1974).

[57]   R. R. Brooks, M. Hoashi, S. M. Wilson, and R. Zhang, "Extraction into methyl isobutyl keytone of metal complexes with ammonium pyrrolidine dithiocarbamate formed in strongly acidic media," Analytica Chimica Acta **217**, 165-170 (1989).

[58]   M. Arnac, G. Verboom, "Solubility product constants of some divalent metal ions with ammonium pyrrolidine dithiocarbamate," Anal Chem. **46**, 2059 (1974).

[59]   M. Hehlen, "Novel materials for laser refrigeration," Proc. SPIE 7228, 72280E (2009).

[60]   J. Thiede, J. Distel, S.R. Greenfield, R.I. Epstein, "Cooling to 208 K by optical refrigeration," Appl. Phys. Lett. **86**, 154107 (2005).

[61]   T. R. Gosnell, "Laser cooling of a solid by 65 K starting from room temperature," Opt. Lett. **24** 1041 (1999); B. C. Edwards, J. E. Anderson, R. I. Epstein, G. L. Mills, A. J. Mord, "Demonstration of a solid-state optical cooler: An approach to cryogenic refrigeration," J. Appl. Phys. **86**, 6489 (1999).

[62]   X. Luo, M. D. Eisaman, T. R. Gosnell, "Laser cooling of a solid by 21K starting from room temperature," Optics Lett. **23**, 639 (1998).

[63]   C. E. Mungan, M. I. Buchwald, B. C. Edwards, R. I. Epstein, T. R. Gosnell, "Laser Cooling of a Solid by 16 K Starting from Room Temperature," Phys. Rev. Lett. **78**, 1030 (1997).

[64]   A. Rayner, M. E. J. Friese, A. G. Truscott, N. R. Heckenberg, H. Rubinsztein-Dunlop, "Laser cooling of a solid from ambient temperature," J. Modern Optics **48**, 103 (2001).

[65]   J. Fernandez, A. Mendioroz, A. J. Garcia, R. Balda and J. L. Adam, "Anti-Stokes laser-induced internal cooling of Yb^{3+}-doped glasses," Phys. Rev. B **62**, 3213 (2000).

[66] J. Fernandez, A. Mendioroz, R. Balda, M. Voda, M. Al-Saleh, A. J. Garcia-Adeva, J. L. Adam, and J. Lucas, "Origin of laser-induced internal cooling of Yb^{3+}-doped systems," Proc. SPIE **4645**, 135 (2002).

[67] J. V. Guiheen, C. D. Haines, G. H. Sigel, R. I. Epstein, J. Thiede, W. M. Patterson, "Yb^{3+} and Tm^{3+}-doped fluoroaluminate glasses for anti-Stokes cooling", Phys. Chem. Glasses **47**, 167 (2006).

[68] C. W. Hoyt, M. Sheik-Bahae, R. I. Epstein, B. C. Edwards, J. E. Anderson, "Observation of Anti-Stokes Fluorescence Cooling in Thulium-Doped Glass," Phys. Rev. Lett. **85**, 3600 (2000).

[69] C. W. Hoyt, M. P. Hasselbeck, M. Sheik-Bahae, R. I. Epstein, S. Greenfield, J. Thiede, J. Distel, J. Valencia, "Advances in laser cooling of thulium-doped glass," J. Opt. Soc. Am. B **20**, 1066 (2003).

[70] J. Fernandez, A. J. Garcia-Adeva and R. Balda, "Anti-Stokes Laser Cooling in Bulk Erbium-Doped Materials," Phys. Rev. Lett. **97**, 033001 (2006).

[71] A. Garcia-Adeva, R. Balda, J. Fernandez, "Anti-Stokes laser cooling in erbium-doped low phonon materials," Proc. SPIE 6461, 646102 (2007).

[72] C. E. Mungan, S. R. Bowman, T. R. Gosnell, "Solid-state laser cooling of ytterbium-doped tungstate crystals," *2000 International Conference on Lasers*, 4-8 Dec. 2000, Albuquerque, NM, USA.

[73] R. I. Epstein, J. J. Brown, B. C. Edwards, A. Gibbs, "Measurements of optical refrigeration in ytterbium-doped crystals," J. Appl. Phys. **90**, 4815 (2001).

[74] S. Bigotta, D. Parisi, L. Bonelli, A. Toncelli, A. Di Lieto, M. Tonelli, "Laser cooling of Yb^{3+}-doped BaY_2F_8 single crystal," Opt. Mater. **28**, 1321 (2006).

[75] S. Bigotta, A. Di Lieto, D. Parisi, A. Toncelli, M. Tonelli, "Single fluoride crystals as materials for laser cooling applications," Proc. SPIE 6461, E1 (2007).

[76] W. M. Patterson, M. P. Hasselbeck, M. Sheik-Bahae, S. Bigotta, D. Parisi, A. Toncelli, M. Tonelli, R. I. Epstein, J. Thiede, "Observation of optical refrigeration in Tm^{3+}:BaY_2F_8," Lasers and Electro-Optics (CLEO), 16-21 May 2004, San Francisco, CA, USA.

[77] W. Patterson, S. Bigotta, M. Sheik-Bahae, D. Parisi, M. Tonelli, R. I. Epstein, "Anti-Stokes luminescence cooling of Tm^{3+}-doped BaY_2F_8," Optics Express **16**, 1704 (2008).

[78] A. Mendioroz, J. Fernandez, M. Voda, M. Al-Saleh, R. Balda, A. J. Garcia-Adeva, "Anti-Stokes laser cooling in Yb^{3+}-doped KPb_2Cl_5 crystal," Opt. Lett. **27**, 1525 (2002).

Chapter 2

Anti-Stokes luminescence cooling of Tm^{3+}doped BaY$_2$F$_8$

Wendy Patterson[1], **Stefano Bigotta**[2], **Mansoor Sheik-Bahae**[1], **Daniela Parisi**[2], **Mauro Tonelli**[2], **and Richard Epstein**[3]

[1] *Optical Science and Engineering Program, Department of Physics and Astronomy, University of New Mexico, Albuquerque, NM 87131*
[2] *INFN - Sez. di Pisa, Largo B. Pontecorvo 3, 56127 Pisa, Italy NEST - Scuola Normale Superiore, Piazza dei Cavalieri 7, 56126 Pisa, Italy*
[3] *Los Alamos National Laboratory, Los Alamos, NM 87545*

Abstract: We report laser-induced cooling with thulium-doped BaY$_2$F$_8$ single crystals grown using the Czochralski technique. The spectroscopic characterization of the crystals has been used to evaluate the laser cooling performance of the samples. Cooling by 3 degrees below ambient temperature is obtained in a single-pass geometry with 4.4 Watts of pump laser power at λ = 1855 nm.

1. Introduction

Laser cooling of solids is receiving increased attention because it can be the foundation of compact, rugged, efficient, and reliable cryo-coolers [1]. This concept — sometimes referred to as optical refrigeration — uses anti-Stokes fluorescence to remove thermal energy from a condensed matter system, thereby reducing its net temperature. A laser beam excites the material in its low energy absorption tail, i.e. below the mean fluorescence photon energy, ν_f. Optical excitations thermalize with the lattice by absorbing phonons; these excitations then recombine at wavelengths blue-shifted from the pump light, with a cooling efficiency of $\eta_c = (\nu - \nu_f) / \nu$.

The first experimental demonstration was made in 1995, in which a cw titanium sapphire laser (λ = 1015 nm) pumped Yb^{3+} atoms doped in a heavy-metal-fluoride glass

(ZBLAN) leading to a net temperature reduction of about 0.3 degrees [2]. The cooling record has since been pushed to an absolute temperature of 208 K using Yb^{3+}:ZBLAN corresponding to a temperature drop of ~ 88 degrees below the ambient [3]. Laser-cooled solids have now entered the temperature regime of high-performance thermoelectric coolers, with the potential to attain cryogenic temperatures. It has been predicted that laser-cooling of direct-gap semiconductors such as GaAs may allow realization of absolute temperatures approaching 10 K [4].

There has been an ongoing effort to explore other rare-earth dopants and hosts because they can have advantages compared to Yb^{3+}:ZBLAN glass. Early work focused on Yb^{3+}-doped glasses and crystals due the small excited-state absorption. An important milestone was the observation of laser cooling in the presence of excited state absorption using Tm^{3+}:ZBLAN [5]. The Tm^{3+}:ZBLAN material system also provides an approximate two-fold increase in quantum efficiency, which scales inversely with excitation energy. Largely due to its inherently higher efficiency, Tm^{3+}:ZBLAN holds the current record for cooling power (i.e. radiative heat lift) of ~ 70 mW. In 2006, laser cooling of an erbium-doped KPb$_2$Cl$_5$ crystal and CNBZn glass was reported [6]. This is a significant result because the cooling transition in erbium is accessible to high-power laser diodes.

Here, we present results from laser cooling experiments with Tm^{3+}-doped BaY$_2$F$_8$. To the best of our knowledge, this is the first time a Tm^{3+}-doped single crystal showed net cooling. This crystalline host offers many important advantages compared to ZBLAN that make it attractive for laser cooling applications [7]. First, it has lower phonon energy (45 meV compared to 72 meV) which reduces the rate of deleterious non-

radiative decay via a multi-phonon emission pathway. This leads to higher quantum efficiency. It also has greater transparency at thermal wavelengths (far-infrared) that make it less susceptible to radiative heat loading. We estimate the emissivity to be $\varepsilon \approx$ 0.77 compared to 0.89 for ZBLAN. Additionally, the thermal conductivity is $\sim$ 7 times higher than ZBLAN. A fourth advantage we note is the higher material hardness of the BaY$_2$F$_8$ host which allows for better polish and direct deposition of optical coatings. Moreover, it is significantly less hygroscopic than ZBLAN [8]. The Stark splitting in the ground state manifold is greater than Tm^{3+}:ZBLAN, which limits the absolute minimum achievable temperature, but has the advantage of increasing efficiency at room temperature. Although BaY$_2$F$_8$ has less favorable conductivity and hardness compared to the widely used YAG laser crystal, its superior optical properties and quantum efficiency make it a better choice for laser cooling [7].

2. Experimental

2.1. Crystal growth

Crystal growth was carried out at the Physics Department of the University of Pisa in a Czochralski furnace with resistive heating. With this apparatus, BaY$_2$F$_8$ single-crystals with nominal doping of 1.2% thulium have been grown by adding suitable amounts of BaTm$_2$F$_8$. To avoid OH$^-$ contamination, the fluoride starting materials are purified at AC Materials (Orlando, FL) and the growth process carried out in a high-purity (99.999%) argon atmosphere. During growth, the rotation rate of the sample is 5 rpm, the pulling rate 0.5 mm/h, and the temperature of the melt is in the range 987-995ºC. The furnace is also equipped with a computer controlled apparatus for diameter control. The average

size of the BaY$_2$F$_8$ crystals was about 15 mm in diameter and 55 mm in length. The crystals are of good optical quality and appear to be free of cracks. The crystals were analyzed using the X-ray Laue technique, verifying their monocrystalline structure and crystallographic axis orientation. The crystals are cut in small samples with edges along *b* and *c* axes because they are the most important orientations for optical applications. The faces are polished to high optical quality using alumina suspensions.

2.2. Spectroscopic set-up

The measurement of the room temperature absorption coefficient has been performed by means of a spectrophotometer (*VARIAN CARY 500 Scan*) operating in the range 250–3200 nm, with typical resolution near 0.1 and 1 nm in the visible and in the NIR, respectively. The room temperature fluorescence spectra of the 3F4 → 3H6 transition were performed with the aim to measure the mean fluorescence wavelength (λ_f) and to derive a better estimate for the absorption coefficient in the long wavelength tail of the absorption spectra. The pump source was a tunable cw Ti:Al$_2$O$_3$ laser, pumped by an Ar$^+$ laser. The fluorescence signal is detected perpendicular to the pump laser direction to avoid spurious pump scattering. The luminescence was chopped then focused by a monochromator with 25 cm focal length, equipped with a 300 gr/mm grating; the resolution of the measurement was 1.2 nm. To record the spectra in various sample orientations, a Glan-Thomson polarizer is placed in front of the input slit of the monochromator. The signal was filtered by a silicon filter, detected by a liquid nitrogen cooled InSb detector, fed into pre-amplifiers, processed by a lock-in amplifier and subsequently stored on a PC.

2.3. Laser cooling

We excited the sample using a high power, singly-resonant, optical parametric oscillator (OPO) based on periodically-poled LiNbO$_3$ [9]. The OPO is synchronously pumped by 80 ps (FWHM) mode-locked pulses from a Nd3+:YAG laser at a wavelength of 1.064 μm with a repetition rate of 76 MHz, delivering up to 20W. The OPO output is tunable between 1.7–2.1 μm with power in the range of 4–6Watts. However, when the OPO is operating at high power and near degeneracy (2.128 μm), there is a tendency towards several resonant oscillations, together with the undesirable features of frequency and mode instability [13]. As a result, the signal bandwidth can be as large as tens of nanometers. The insertion of two etalons within the OPO cavity significantly stabilized and reduced the bandwidth of the signal radiation to within the limitations of the spectrometer (≈ 1 nm). The room temperature reference sample is placed in a vacuum chamber (~10^{-5} Torr) suspended by two glass microscope slides in order to minimize heat load from thermal conduction. The pump light makes a single pass through the sample. The change in temperature is measured relative to the reference sample using a micro-bolometer camera (Raytheon 2000AS) which views the sample through an IR-transparent window (NaCl). The camera was calibrated against a precision silicon temperature diode in a separate measurement by placing the sample in a variable temperature cryostat. The data were stored by a frame grabber card on a PC as 8-bit pixel image files.

3. Spectroscopic and cooling results

BaY$_2$F$_8$ is a biaxial crystal, and therefore requires six spectra to be fully characterized. Transitions between 3F4→3H6 levels in Tm^{3+} ions, however, are dominated by the

electric-dipole term and, as a result, it is not necessary to take the orientation of the magnetic field into account. Additionally, the polarized spectroscopic properties of Tm^{3+}doped BaY$_2$F$_8$ are readily available in the literature [11]. For the aim of this work, it is sufficient to show the spectroscopic measurements carried out along the *E // b* polarization, i.e. the one used for our laser cooling experiments, even if we used all three polarization components in order to derive the mean fluorescence wavelength, λ_f. Luminescence and absorption data for Tm^{3+}:BaY$_2$F$_8$ are shown in Fig. 1, which displays appreciable absorption at wavelengths longer than $\lambda_f = 1793$ nm (shaded region to the right of the solid vertical line). The presence of absorption beyond λ_f (by at least *kT*) is a key requirement for cooling. We note that crystalline hosts exhibit sharper spectral features, as compared to amorphous materials, due to the regular periodic structure of their atoms. These larger peaks in the target absorption region can be used advantageously in a laser cooling experiment.
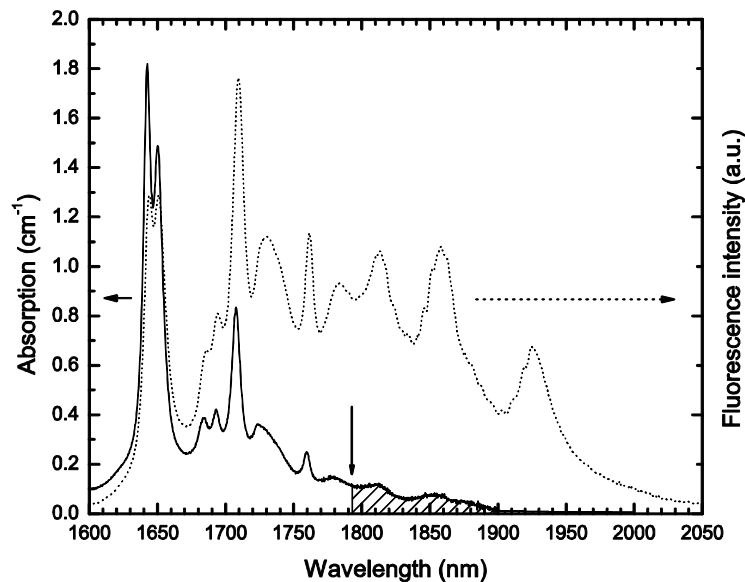
Fig. 1. *E // b* absorption (solid curve) and emission (dotted curve) spectra for our 1.2% Tm^{3+}:BaY$_2$F$_8$ sample. The solid vertical line indicates the mean fluorescent wavelength at λ_f = 1793 nm. In a laser cooling experiment, excitation takes place on the long wavelength side of this line in the shaded absorption region.

In order to exactly predict the expected temperature drop and determine the cooling efficiency, the value of the absorption coefficient in the long-wavelength tail must be known with high precision. Given that the absorption coefficient in the region of interest for laser cooling applications is usually very small when obtained using transmission spectroscopy, it is common practice to derive the absorption coefficient from the emission spectra using a reciprocity relation [12].

Generalizing the expression found in the cited work for the case of anisotropic crystals, we obtain:

$$\sigma_{abs}^{\gamma} = \frac{Z_u}{Z_l} \sigma_{em}^{\gamma} \exp\left[\left(\frac{hc}{\lambda} - E_{ZPL}\right)/kT\right] \propto \lambda^5 I^{\gamma}(\lambda) e^{hc\lambda/kT} \qquad (1)$$
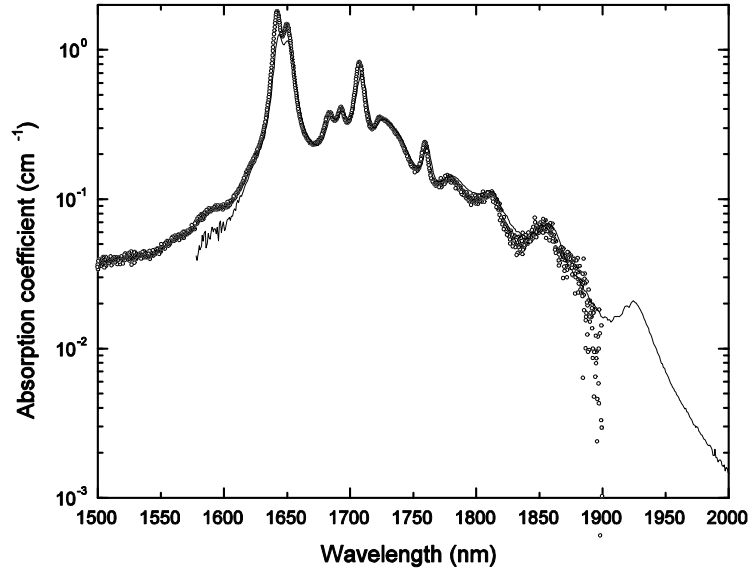
Fig. 2. *E // b*-polarized absorption spectrum of 1.2% Tm^{3+}:BaY$_2$F$_8$. The open circles represent the data obtained with the spectrometer, while the solid line indicates the

absorption derived from the emission spectrum using the reciprocity relation shown in the text.

where σ_{abs}^{γ}, σ_{em}^{γ} and $I^{\gamma}(\lambda)$ are the absorption and emission cross sections and the intensity of the fluorescence emission for the γ polarization; Z_u and Z_l are the partition functions for the upper and the lower electronic levels and E_{ZPL} is the energy of the zero phonon line. The values obtained by inserting the emission intensity data (normalized to the spectrometer absorption coefficient at large absorption) were over an order of magnitude above the noise level of our instrument. As shown in Fig. 2, the data obtained from reciprocity are in excellent agreement with those acquired with the spectrometer, and they give a better signal-to-noise ratio for $\alpha < 10^{-1}$ cm^{-1}. The discrepancy between the two curves at the largest peak (1650 nm) can be easily ascribed to the re-absorption process which decreases the luminescence intensity and hence the inferred absorption coefficients.

The change in temperature (relative to a reference sample) is recorded as a function of time for a given pump wavelength, and subsequently fitted to a single exponential decay, whereby the maximum temperature change at a given pump wavelength can be inferred. On average, a sample will take approximately 40 minutes to reach its equilibrium cooling or heating state. This wavelength-dependent temperature change (ΔT) normalized to pump power (P) is shown in Fig. 3 for the $E \mathbin{/\mkern-5mu/} b$ orientation of the crystal. We correlate the two minima at ~1850 and ~1925 nm with the presence of absorption peaks around these wavelengths for the $E \mathbin{/\mkern-5mu/} b$ polarization. This experimental data is analyzed quantitatively by fitting with the following relation [5]:

$$\frac{\Delta T}{P} \sim \kappa \left[\alpha_B + \alpha_R(\lambda)(1-\eta_q) - \alpha_R(\lambda)\eta_q \frac{\lambda - \lambda_F}{\lambda_F} \right] \tag{2}$$

where α_B is the wavelength-independent background absorption coefficient, $\alpha_R(\lambda)$ is the resonant absorption data shown in Fig. 2, η_q is the non-unity quantum efficiency coefficient to account for deleterious fluorescence quenching, and κ takes into account the geometry of the sample and the vacuum chamber as well as thermo-dynamic factors (i.e. the radiative heat transfer). The constant coefficients η_q and α_B and κ are adjusted to fit the heating/cooling data. We find $\eta_q \approx 0.98$, $\alpha_B \approx 2\times10^{-4}$ cm^{-1} for *E // b* and $\kappa = 723$ cmK/W for the data presented in Fig. 3. It is worth noting that the experimental value of κ is lower than the theoretical value. This can be ascribed to stray light circulating in the vacuum chamber due to the spurious reflections of the pump beam which can inadvertently heat the sample. A more refined pumping scheme could reduce the spurious reflections inside the vacuum chamber and hence enhance the cooling efficiency. Our configuration produced a maximum temperature drop of 3.2 degrees, at a wavelength of 1855 nm, given 4.4 W of pump power.

For practical applications, an estimate of the cooling efficiency, i.e. the ratio of the absorbed and the cooling power, is crucial. The absorbed power can be easily estimated using the Lambert-Beer law:

$$P_{abs} = P_{in}(1-e^{-\alpha\ell}) \tag{3}$$
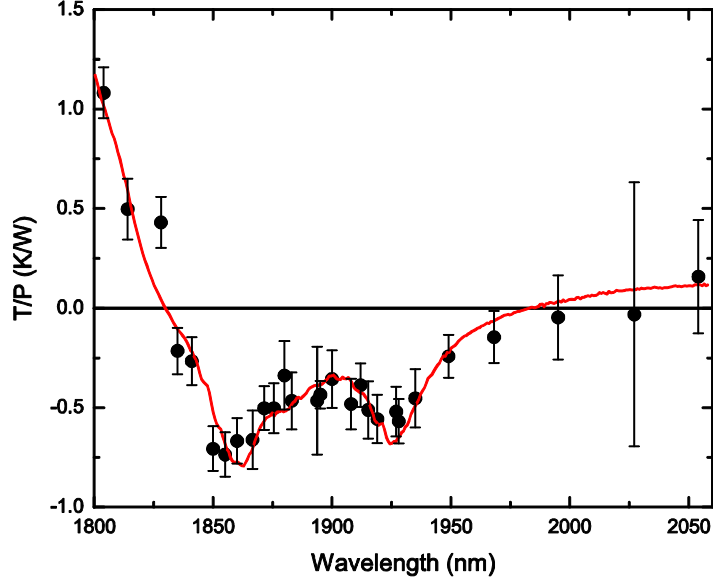
Fig. 3. Wavelength-dependent temperature change normalized to pump power for BaY$_2$F$_8$ doped 1.2% Tm^{3+} for *E // b*. Data points below the horizontal reference line indicate net cooling. The solid curve is a fit as described in the text.

where ℓ is the length of the crystal, α is the total absorption coefficient and P_{in} is the incident power on the sample. The cooling power can be obtained from general thermodynamical considerations. In fact, at equilibrium the cooling power must balance the incoming power. If we consider that the only heat load on the sample is due to the radiation from the vacuum chamber, we can write:

$$P_{cool} = P_{heat} = \varepsilon_S \sigma A (T_C^4 - T_S^4) \tag{4}$$

where T_s is the temperature of the sample, T_c is the vacuum chamber temperature, ε_s is the emissivity of the host material, A is the surface area of the sample, and σ is the Stefan-Boltzmann constant. The cooling efficiency, η_{cool}, is then obtained by dividing Eq. 4 by 3. Shown in Fig. 4 are both the theoretical and the experimental cooling efficiency versus pump wavelength for the 1.2% Tm^{3+}:BaY$_2$F$_8$ crystal when pumped in the *E // b* polarization. A maximum cooling efficiency of η_{max} = 3.4% has been observed at 1934

44

nm. The slope attained at $\lambda = 1855$ nm is -0.74 deg/Watt which compares favorably to the best previously reported values of $\eta_{max} = 3\%$ and -0.73 deg/Watt for Tm^{3+}:ZBLAN [10]. The discrepancy between the theoretical and experimental data at wavelengths longer than ~ 1950 nm can be ascribed to the low absorption coefficient in this region (hence, the large error bars).
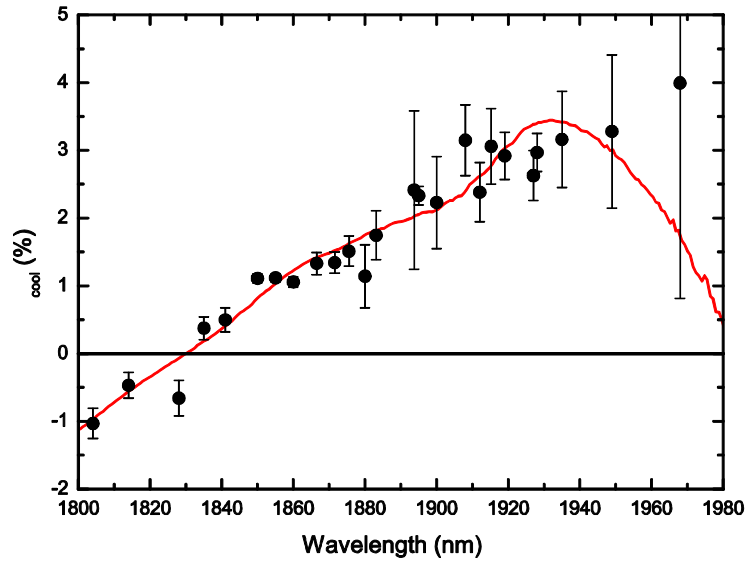
Fig. 4. Cooling efficiency as a function of the pump wavelength for the 1.2% Tm^{3+}-BaY$_2$F$_8$ crystal. The theoretical prediction (solid line) and experimental data (dots) are shown for *E // b*.

Note that the maximum cooling efficiency occurs at 1934 nm, while the maximum temperature drop occurs at 1855 nm. In the ideal case with no impurities,η *cool* increases with increasing wavelength [2]. This is clearly visible in Fig. 4 for wavelengths up to 1934 nm, beyond which the impurity absorption dominates and the cooling efficiency decreases. According to Eq. 2, the temperature drop for a given pump power is proportional to the product of α_R (Fig. 2) and η_{cool} (Fig. 4). Since with increasing

wavelength, α_R decreases and η_{cool} increases, ΔT/P (Fig. 3) forms a minimum which is found at 1855 nm.

A similar analysis was performed also for the $E \perp b,c$ polarization. The results, not shown here, are comparable with that observed for the $E \mathbin{//} b$ polarization and are in good agreement with theoretical values.

4. Conclusion

In summary, we report the first observation of laser cooling with Tm^{3+}:BaY$_2$F$_8$. This crystalline host has shown net cooling when doped with the rare-earth ions Yb^{3+} and Tm^{3+} which allows for pumping at distinctly different wavelengths. BaY$_2$F$_8$ possesses a range of properties that compare favorably with ZBLAN glass in laser cooling applications.

References and links

[1]   *Laser Cooling of Solids*, edited by Richard I. Epstein, Mansoor Sheik-Bahae, Proc. SPIE **6461** (Bellingham, Washington, 2007).

[2]   R.I. Epstein, M.I. Buchwald, B.C. Edwards, T.R. Gosnell, C.E. Mungan, "Observation of laser-induced fluorescent cooling of a solid," Nature **377**, 500–502 (1995).

[3]   J. Thiede, J. Distel, S.R. Greenfield, R.I. Epstein, "Cooling to 208 K by optical refrigeration," Appl. Phys. Lett. **86**, 154107 (2005).

[4]   M. Sheik-Bahae, R. Epstein, "Can laser light cool semiconductors?," Phys. Rev. Lett. **92**, 247403 (2004).

[5]   C.W. Hoyt, M. Sheik-Bahae, R.I. Epstein, B.C. Edwards, J.E. Anderson, "Observation of anti-Stokes fluorescence cooling in thulium-doped glass," Phys. Rev. Lett. **85**, 3600–3603 (2000).

[6]   J. Fernandez, A. J. Garcia-Adeva, R. Balda, "Anti-Stokes laser cooling in bulk erbium-doped materials," Phys. Rev. Lett. **97**, 033001 (2006).

[7]   S. Bigotta, D. Parisi, L. Bonelli, A. Toncelli, M. Tonelli, A. Di Lieto, "Spectroscopic and laser cooling results on Yb3+-doped BaY2F8single crystal," J. Appl. Phys. **100**, 013109 (2006).

[8]   J.M. Parker, Annu. Rev. Mater. Sci. "Fluoride glasses," **19**, 21–41 (1989).

[9]   C.W. Hoyt, M. Sheik-Bahae, M. Ebrahimzadeh, "High-power picosecond optical parametric oscillator based on periodically poled lithium niobate," Opt. Lett. **27**, 1543–1545 (2002).

[10]   C.W. Hoyt, M.P. Hasselbeck, M. Sheik-Bahae, R. Epstein, S. Greenfield, J. Thiede, J. Distel, J. Valencia, "Laser cooling in thulium-doped glass," J. Opt. Soc. Am. B **20**, 1066–1074 (2003).

[11]   F. Cornacchia, D. Parisi, C. Bernardini, A. Toncelli, and M. Tonelli, "Efficient, diode-pumped Tm3+:BaY2F8vibronic laser," Opt. Express **12**, 1982–1989 (2004).

[12]   R. I. Epstein, J. J. Brown, B. C. Edwards and A. Gibbs, "Measurements of optical refrigeration in ytterbiumdoped crystals," J. Appl. Phys. **90**, 4815–4819 (2001).

[13]   K. Puech and L. Lefort and D. C. Hanna, "Broad tuning around degeneracy in a singly resonant synchronously pumped parametric oscillator by means of a diffraction grating," J. Opt. Soc. Am. B **16**, 1533–1538 (1999).

Chapter 3

Preparation and Characterization of High-Purity Metal Fluorides for Photonic Applications

W.M. Patterson[,1], M. Sheik-Bahae[1], R.I. Epstein[2], P. C. Stark[2], T. M. Yoshida[2], M.P. Hehlen[2]*

[1]   800 Yale Blvd. NE, Albuquerque, NM 87131

[2]   Los Alamos National Laboratory, Los Alamos, NM 87545, USA

wendy.patterson@gmail.com

High-purity fluorides for optical refrigeration.

We present a chelate-assisted solvent-extraction method that can be applied to every component of ZBLANI:Yb^{3+} (ZrF$_4$ – BaF$_2$ – LaF$_3$ – AlF$_3$ – NaF – InF$_3$: YbF$_3$) glass to enable a material with significantly reduced transition-metal impurities. In addition, an advanced method for the precipitation of the respective binary fluorides and the removal of oxide and OH- impurities is described. Several characterization tools are used to

quantitatively and qualitatively verify the reduction of both transition metal and hydroxyl ions. First, the concentrations of several problematic transition-metal impurities in the zirconium precursor were measured at various stages of the purification process using inductively-coupled plasma mass spectrometry (ICP-MS). Chelate-assisted solvent extraction was found to be successful in reducing transition-metal concentrations in a $ZrCl_2O$ solution from 72,500 to ~100 parts-per-billion (ppb). Second, laser-induced cooling in bulk ZBLANI:Yb^{3+} samples was used as a sensitive probe for ppb-level impurities. Laser cooling was observed at room temperature for ZBLANI:Yb^{3+} samples fabricated from purified metal fluoride precursors, confirming the results of the ICP-MS analysis and demonstrating the effectiveness of the purification methods in an optical material. The high-purity metal fluorides synthesized by the methods presented here are expected to enable a number of high-performance optical materials, including solid-state optical refrigerators and deep-ultraviolet transparent crystals.

Introduction

Fluoride crystals and glasses are of interest to a wide range of photonic applications including bulk optics for deep ultraviolet (UV) photolithography [1], optical fibers for high power or long-haul transmission [2],[3], host materials for lasers and optical amplifiers [2],[4]-[7], scintillators [8],[9], upconversion phosphors [10], and solid-state optical refrigerators [11]. These applications take advantage of the high band gap energy and/or the low optical phonon energies (typically <500 cm^{-1}) of fluorides. The attractive

intrinsic properties of fluorides, however, can be substantially degraded by the presence of impurities. Transition metal ions have optical transitions in the UV and visible spectral regions [12],[13], leading to undesired background absorption as well as non-radiative quenching of excited states even at trace levels. Furthermore, oxygen-based impurities such as oxides, hydroxyl (OH^-), and water can degrade material performance by introducing UV absorption [14],[15] and high-energy vibrational modes that enhance multi-phonon relaxation rates of excited states [16]-[21]. While the slow growth of fluoride crystals can reduce the concentration of some of these impurities, fluoride glasses generally contain all of the impurities that were present in the melt from which they were quenched. Solid-state optical refrigerators, also known as laser coolers, have particularly demanding purity requirements. For the fluorozirconate glass ZBLAN (ZrF_4 – BaF_2 – LaF_3 – AlF_3 – NaF), for example, it was estimated that transition- metal and OH^- impurities in excess of ~100 parts-per-billion (ppb) severely compromise material performance [22]. Other applications have similarly stringent purity requirements. The preparation of high-purity binary fluorides is therefore critical to enabling the desired performance of many fluoride optical materials.

There currently exists no comprehensive method for the purification and synthesis of ultra-pure metal fluorides. The chemical inertness and fairly high melting temperatures of fluorides prevent the use of many of the standard purification methods. While some successes have been achieved by sublimation and distillation of ZrF_4 as well as zone refining [23],[24], these are not applicable to many of the metal fluorides of interest. The use of CF_4, NF_3, SF_6, Cl_2, CCl_4, or O_2 reactive gas atmospheres during melting has been widely used to reduce oxide impurities [25],[26], however, such methods are not

acceptable for many high purity glass applications as they can re-contaminate the final glass with unwanted species. More recent developments include vapor phase processes, which appear attractive due to the success of chemical vapor deposition (CVD) in purifying silica for fiber technology. Some preliminary results appear to be encouraging [27]-[29]. However, the practical achievement of fluoride glasses through CVD appears difficult due to the high evaporation temperature of several of the fluoride glass components. A comprehensive purification strategy must, therefore, target the chemistry *before* the formation of the metal fluoride. One such method is chelate-assisted solvent extraction (CASE). In this process, a chelate is used to bind to undesired metal ions in an aqueous phase and to transfer the metal-chelate complexes into a second organic phase. Chelate-assisted solvent extraction is widely used in analytical chemistry to pre-concentrate heavy metals for trace analysis [30]-[33]; alternatively, it can be used to remove metal ions from the aqueous phase to achieve purification. Ling et al. have used the latter approach with ammonium-pyrrolidine-dithio-carbamate (APDC) as the chelate and methyl-isobutyl-ketone (MIBK) as the organic phase to reduce Co, Ni, and Cu to < 5 ppb and Fe to < 10 ppb in zirconium solutions [33].

Our approach is to exploit a single chelate/organic solvent system suitable for the individual purification of all components of the laser-cooling glass ZBLANI:Yb^{3+} (ZrF_4 – BaF_2 – LaF_3 – AlF_3 – NaF – InF_3 – YbF_3), in order to minimize the development effort and to simplify processing. The APDC/MIBK system is ideal for the removal of the specific transition metals that are detrimental to laser cooling while not affecting the metal ions of the glass components.

In this paper, we (1) expand CASE to the purification of main group elements (Zr, Ba, Al, Na, In) and the rare earths (La, Yb, Tm), (2) advance the method to include the precipitation and ultra-drying of the resulting binary metal fluorides, and (3) quantitatively verify the impact of reduced impurities in an optical refrigerator material. We begin the Materials Synthesis section with a detailed description of all processing steps used to produce ultra-pure ZBLANI:Yb^{3+} glass. As a measure of our ability to successfully remove both transition metal and hydroxyl ions, we use several characterization tools to quantitatively and qualitatively verify purity, detailed in the Experimental section. These include ICP-MS where the zirconium precursor solutions are analyzed for quantities of particular transition metal ions of interest. We also outline measurements on the bulk ZBLANI:Yb^{3+} samples, where we test for optical refrigeration.

Materials Synthesis

Figure 1 shows a flow chart outlining the general steps used to produce ultra-pure ZBLANI:Yb^{3+} glass.
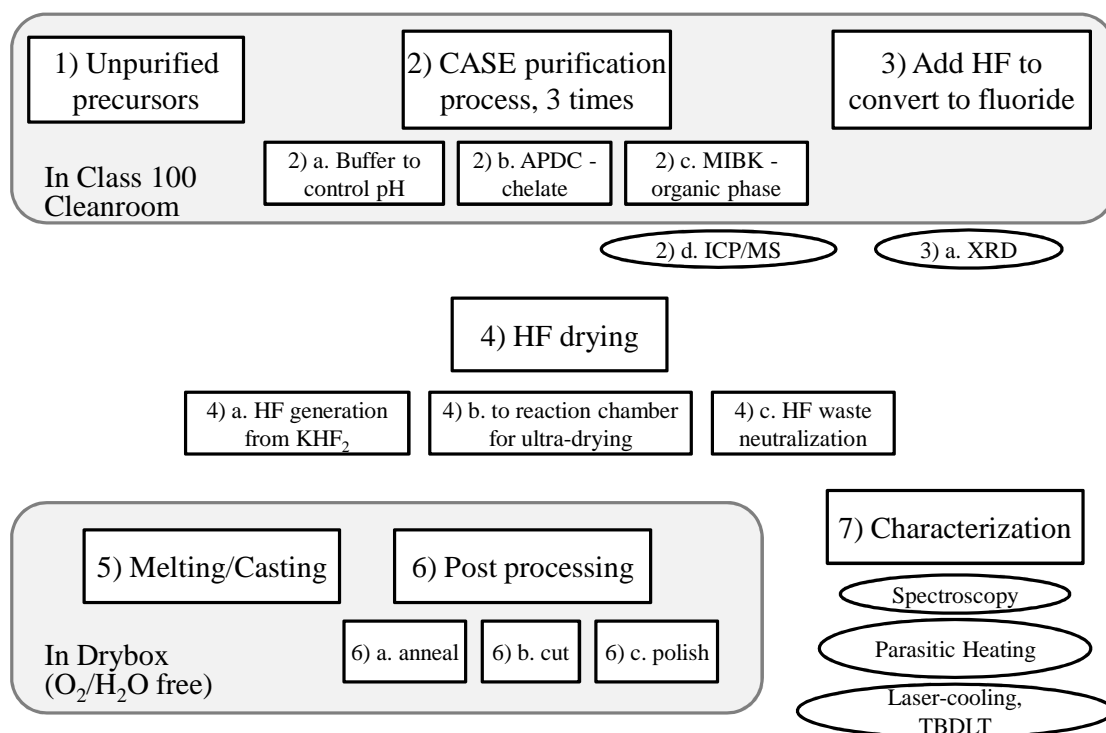
Figure 1. Outline of the major steps for reduction of transition metals and oxidic impurities in an effort to produce ultra-pure ZBLANI:Yb^{3+} glass. The boxes represent material synthesis steps while the ovals indicate various characterization tools.

Hydrofluoric acid and hydrogen fluoride gas: The following procedures involve experimentation with concentrated hydrofluoric acid and hot hydrogen fluoride gas. These substances are toxic and can pose a severe health hazard if not handled properly.

High-Purity Reagents and Clean Processing: Hydrofluoric acid (49%), nitric acid (69%), and hydrochloric acid (33%) were doubly-distilled and trace-metal grade (GFS Chemicals, Veritas). The ultra-high purity (UHP) water was obtained from Inorganic Ventures. Methyl-isobutyl-ketone (also known as 4-Methyl-2-pentanone or MIBK) was from Acros Organics, electronic grade. All processing steps were carried out in a fume hood inside a Class 100 clean room environment. Acid evaporations were

performed in a distillation still constructed entirely from perfluoroalkoxy (PFA) resin (Savillex Corp.) and operated inside a fume hood in the clean room. The evaporation side of the still was heated to 190 °C by a temperature-controlled heating jacket. The PFA evaporation tube was wrapped in an aluminum sleeve before inserting it into the heating jacket to allow for more even heat distribution. Performing acid evaporations in the still reduced the risk of recontamination by keeping the solutions enclosed during the lengthy evaporation process. Furthermore, the still safely contained the highly corrosive acidic fumes and allowed for easy and proper disposal of the acidic distillate. All vessels and utensils used in the following processing steps were cleaned by leaching them in dilute nitric acid at elevated temperatures for several days before use. This released undesirable ions potentially trapped within the matrix of the polymer which might have contaminated the solutions.

Preparation of APDC Chelate Solution: The ammonium-pyrrolidine-dithio-carbamate (APDC) chelate (Acros Organics) was stored at 4 °C until needed for solvent extraction. A 1% solution of APDC in UHP H_2O was prepared daily by dissolving 1 g of APDC in 100 mL of water and filtering through a < 0.2 µm pore size Nylon syringe filter.

Preparation of Buffer Solution: Proper extraction of unwanted transition metal impurities required a stable pH of the aqueous solution in the range of 2.5 - 5.5 [31]-[33]. This was achieved by use of a buffer solution typically prepared by dissolving 50 g of ammonium acetate (Fluka, 99.995%) in 100 mL of UHP water and adding acetic acid to adjust the pH to ~ 4.5.

Chelate-Assisted Solvent Extraction (CASE): 5 mL of the 1% APDC solution was added to the buffered (see below) aqueous solution of the metal ion to be purified. The mixture was briefly shaken. 35 mL of MIBK was added, and the two-phase system was shaken vigorously for 1 minute. After letting the system equilibrate for 10 minutes, the bottom aqueous phase was collected and the organic phase was discarded. This extraction procedure was repeated three times. The final aqueous phase was collected in poly-tetrafluoroethylene (PTFE) beakers. Separate PTFE beakers were used for each metal ion to prevent cross-contamination.

Zirconium fluoride (ZrF₄): 41 g of $ZrCl_2O \cdot xH_2O$ (Alpha Aesar, Puratronic®, 99.9985%) were dissolved in 68 g UHP water. The pH of this solution was increased by boiling the solution and continuously adding water (typically ~350 mL total) over the course of 24 hours to reach a pH of ~1, thus reducing the amount of buffer needed to adjust the pH for the subsequent solvent extraction. This step was important as excess buffer interfered with the final precipitation of zirconium fluoride. The volume of the solution was ~65 mL after this step. 60 g of buffer solution was added to adjust the pH to > 2, preferably ~2.5, and the solution was filtered through a < 0.2 µm Nylon syringe filter to remove larger particulates. The filtered solution was transferred into a separatory funnel for CASE (see above). During solvent extraction, the organic phase progressed from yellowish to colorless with each successive extraction step. After three extractions, the last aqueous phase was combined with 28 g of hydrofluoric acid to form a slurry of zirconium fluoride precipitates which was evaporated to dryness (see above) over 12 hours. The product was $ZrF_6(NH_4)_3$ which was decomposed to $ZrF_4 \cdot H_2O$ (see below).

Barium Fluoride (BaF$_2$): 10 g of BaCO$_3$ (Strem Chemicals, Puraterm, 99.999%) were dissolved in 30 g of hydrochloric acid. The acid was added very slowly in order to control the violent release of CO$_2$. The milky solution was evaporated to dryness over 7 hours. The resulting BaCl$_2$ was dissolved in 34.5 g of UHP water, and 33 g of the buffer solution was added to reach a pH of ~3.8. The buffered aqueous solution was filtered through a < 0.2 µm pore size syringe filter directly into the separatory funnel for solvent extraction (see above). The color of the organic phase progressed from light yellow to colorless by the last extraction. The final aqueous phase was collected, and 42.5 g of hydrofluoric acid was added. A thick opaque slurry of BaF$_2$ could be isolated by carefully decanting the excess hydrofluoric acid after allowing the precipitates to settle for several hours.

Lanthanum Fluoride (LaF$_3$): To 2.9 g of La$_2$O$_3$ (Metall Rare Earth Limited, 99.9999%) 38 g of doubly distilled HNO$_3$ was added very slowly to dissolve the oxide and to form lanthanum nitrate. It was necessary to very slowly add the nitric acid in order to control the violent reaction with the lanthanum oxide powder. The entire solution was transferred to the evaporation tube and evaporated to dryness over the course of 10 hours. The resulting lanthanum nitrate was dissolved in 27 g of UHP water. Next, 18.5 g of the prepared buffer solution was added, raising the pH to 3.3. This buffered solution was filtered with a Nylon syringe filter into the separatory funnel for solvent extraction. After three extractions, the last aqueous phase was collected into a designated PTFE beaker. It was found that the rate at which the HF acid was added affected the LaF$_3$ crystallization dynamics. Therefore, the HF acid was added very slowly while the solution was stirred with a PTFE stir bar at 550 rpm. This method favored the formation of LaF$_3$ and

suppressed the competing precipitation of ammonium compounds. The excess HF was easily decanted from the resulting white slurry.

Aluminum Fluoride, (AlF$_3$): The synthesis of AlF$_3$ began with the addition of 27 g of UHP water to 6 g of aluminum chloride hexahydrate (Alfa Aesar, Puratronic®, 99.9995%). A significant amount of buffer, typically more than 50 g, was required to reach a pH of >2.8. This buffered chloride solution was filtered into a separatory funnel for purification. The organic phase progressed from a light yellow tint to colorless by the third extraction. Following purification, the last aqueous phase was collected and 40.6 g of HF acid was added to form visible precipitates. These precipitates did not settle, and thus the entire solution had to be evaporated in the evaporation tube during the course of 8 hours.

Sodium Fluoride (NaF): 7 g of Na$_2$CO$_3$ (Sigma-Aldrich, 99.999%) were dissolved in 32 g of UHP water. 73 g of buffer solution was added to raise the pH to ~5. This solution was filtered and purified via CASE three times as usual. After collecting the last aqueous phase from the third solvent extraction step, 40.5 g of HF acid was added to the solution to precipitate the NaF. The excess HF acid was easily decanted.

Indium Fluoride (InF$_3$): 7.7 g of indium metal (Alfa Aesar, Puratronic®, 99.9999%) was placed in a glass beaker, and 100 g of HNO$_3$ was *very* slowly poured over the metal. It was imperative that this step occurred as slowly as possible to control the violent generation of NO$_x$ gas and to avoid boiling of the acid. This resulting solution was evaporated to dryness in the evaporation tube over the course of 12 hours to obtain indium nitrate. 32 g of UHP water was added to form a milky solution the pH of which was raised to ~2.5 by adding 25 g of buffer solution. This solution was then purified by

solvent extraction as usual. Following the third purification, the last aqueous phase was collected in a PTFE beaker, 25.4 g of HF acid were added, and this solution evaporated to dryness over 12 hours. The resulting $(NH_4)_3InF_6$ was decomposed to yield InF_3 as described below.

Ytterbium Fluoride (YbF₃): 2.5 g of Yb_2O_3 (Metall Rare Earth Limited, 99.9999%) were combined with 35.5 g of HNO_3, resulting in a milky solution which was dried in the evaporation tube for 8 hours to yield ytterbium nitrate. 22 g of UHP water was added to the nitrate and allowed to sit for 1 hour until the powder was dissolved. 21.3 g of buffer solution was then added to raise the pH to ~3.6. This solution was filtered with a Nylon syringe filter into the separatory funnel followed by the usual three steps of solvent extraction. The aqueous phase of the last purification step was collected in a PTFE beaker, and 21.3 g of HF acid was added to precipitate the fluoride which was recovered by decanting the excess HF.

Decomposition and washing: Two of the metals, Zr^{4+} and In^{3+}, formed $(NH_4)_3ZrF_6$ and $(NH_4)_3InF_6$, respectively, by reaction with the NH_4Ac buffer solution rather than directly precipitating as metal fluoride. These compounds were decomposed in a large glassy carbon crucible on a hot plate in the fume hood. The $(NH_4)_3ZrF_6$ compound was slowly heated to 370 °C and the $(NH_4)_3InF_6$ to 460 °C to effect the decomposition and evaporation of ammonium fluoride (NH_4F) and the formation of the respective metal fluoride. The NH_4Ac buffer did not compete with the fluoride formation for the other metal ions.

All fluorides were subjected to a series of washing and drying steps to remove residual buffer, excess acid, or non-fluoride, water soluble compounds. Each fluoride was washed

by adding ~30 mL of UHP water and sonicating the slurry for 0.5 - 1 hour. The insoluble fluoride settled and the excess water was decanted, a procedure that was repeated three times. The product was dried in a PTFE beaker on a hot plate at 190 °C to remove excess water.

Drying of fluorides in hydrogen fluoride (HF) gas: The fluorides obtained above were subjected to drying and fluorination by treating them in HF gas at elevated temperatures using a custom HF gas drying apparatus adapted from Burkhalter et al. [34] and Krämer et al. [35]. The apparatus was designed to allow for drying of two fluoride samples per drying run. For this purpose, the fluorides were transferred to glassy carbon boats in the clean room and inserted into a sealed, corrosion-resistant tube, constructed from Inconel Alloy 600 steel. The Inconel tube was further lined with a glassy carbon tube to protect the fluorides from potential vessel corrosion residues. The drying tube was connected to the HF gas drying apparatus via PFA tubing and inserted into a horizontal tube furnace.

HF gas was produced by decomposing KHF_2 in a separate vertical tube furnace. During a typical 19 hour drying run, 25.6 g of HF gas was produced by decomposing 100 g of previously dried KHF_2 (dried at 190 °C for > 60 hours in vacuum) in a glassy carbon crucible by heating it to 390 °C at 135 °/hr, to 440 °C at 4.5 °/hour, and to 480 °C at 8.3 °/hour. A mass-flow controller (Aalborg, GFC17) maintained a constant flow of semiconductor grade argon (Ar) to provide a ~7 vol% average HF concentration. The Ar/HF gas mixture was injected into the drying tube, which was heated to 300 °C. Excess Ar/HF gas emerging from the drying tube was bubbled through a saturated calcium hydroxide solution that quantitatively removed HF by precipitation of CaF_2. The entire

system was contained in a fume hood. Each metal fluoride was subjected to this drying and fluorination step before being used as a starting material for glass synthesis.

Glass formation and post-processing: The dried fluorides were transferred into an argon drybox in the sealed drying tube. The metal fluorides were weighed, mixed, and transferred to a glassy carbon crucible and covered with a glassy carbon lid. A typical batch size was 4 g, and typical glass compositions are shown in Table 1. The melting crucible was inserted into a computer-controlled chamber furnace which was preheated to 750 ^{o}C. The melt remained in the furnace for up to 5 hours to completely dissolve all components. The melt was subsequently cooled to 550 ^{o}C at 10 ^{o}/minute before the crucible was removed from the furnace and the melt was cast into a platinum mold at room temperature.

Table 1. Composition of the ZBLANI:Yb^{3+} glass samples fabricated in this study. Also shown are vendor-quoted purities of the respective commercial metal fluorides as well as the various chlorides, carbonates, and oxides (along with their vendor quoted purities) that were used as starting materials for the CASE process.

	Z ZrF_4	**I** InF_3	**B** BaF_2	**L** LaF_3	**A** AlF_3	**N** NaF	**Yb** YbF_3
Typical sample stoichiometry (mol%)	53	2.5	20	3	3	17.5	1
Purity of comm. fluoride (%)	99.5	99	99.99	99.9	99.9	99.5	99.9
Commercial starting material	$ZrOCl_2 \cdot 8H_2O$	In	$BaCO_3$	La_2O_3	$AlCl_3 \cdot 6H_2O$	Na_2CO_3	Yb_2O_3
Quoted purity (%)	99.9985	99.9999	99.999	99.99993	99.99956	99.997	99.99992

The resulting glass was annealed in the mold to relieve internal stress and to improve mechanical durability and optical homogeneity. Annealing consisted of heating the glass to just below the glass transition temperature of 250 ºC at 2 º/minute, holding for 1 hour, and cooling to room temperature at a slow rate of 0.2 º/minute.

The glass samples were to undergo a variety of optical characterization techniques, many of them discussed in the Experimental Section. Surface contaminants and imperfections cause heating when exposed to either direct or scattered radiation in the optical experiments. In order to distinguish internal or bulk heating from such surface heating, a polish of extremely high quality was necessary. To prepare a sample for optical characterization, the annealed glass was cut into a rectangular parallelepiped with an ethylene glycol-cooled diamond saw. The two parallel sides designated to receive the pump laser beam were polished to optical quality, while the other sides were polished to transparency. A "wet polish" was necessary to obtain the desired optical finish. To that effect, dried aluminum oxide particles, ranging in diameter from 12 µm down to 0.05 µm, were suspended in emulsions of water-free ethylene glycol and glycerin. The viscosity of the suspensions was controlled by adjusting the amount of glycol. The polishing compounds were prepared daily to ensure that the suspensions did not coagulate and form larger than expected particles that were found to scratch the surface. The sample was wax mounted on a hand held polishing assembly and manually polished with the slurry spread over a fine textured, non-abrasive, polishing cloth until the desired optical finish was obtained. The final samples were stored in the argon drybox until optical testing. Before use, the samples were sonicated in optical grade methanol for several hours then gently cleaned with lens paper.

Table 2 summarizes the glasses synthesized over the course of this development effort and provides comments on sample preparation conditions. Sample No. 1 was fabricated from commercially available metal fluoride precursors (with purities as given in Table 1) without conducting any further purification, except the mandatory ultra-drying and fluorination of metal fluoride precursors in hot hydrogen fluoride gas. Without this ultra-drying step, significant crystallization of the glasses occurred yielding a glass unfit for optical characterization. Samples No. 2, 3, and 4 represent various stages during the CASE process development. Sample No. 5 is identical to Sample No. 4, except for a higher 2 mol% Yb^{3+} concentration. For Sample No. 6, sublimated ZrF_4 (rather than solvent extracted ZrF_4) was provided by the University of Bern. The other glass components were identical to the fluorides used to prepare Sample No. 4. Sample No. 7 is a commercial ZBLAN:2%Yb^{3+} sample procured from IPG Photonics that has shown good laser cooling performance, and it was used as a point of reference in this study.

Table 2. Summary of the Yb^{3+}-doped fluorozirconate samples synthesized and characterized in this study.

Sample Number	Yb^{3+} (mol%)	ZBLANI composition (mol%)	Sample descriptions and preparation notes
1	1	54–21–3.5–3.5–16.5–0.5	Produced from commercial metal fluoride precursors without further purification. Some bulk scattering.
2	1	54–21–3.5–3.5–16–1	First generation CASE. Some bulk scattering.

3	1	53–20–3–3–17.5–2.5	Second generation CASE. Improved melting/casting scheme. Excellent optical quality.
4	1	53–20–3–3–17.5–2.5	Third generation CASE. Modified HF gas drying process. Excellent optical quality.
5	2	53–20–2–3–17.5–2.5	Same as No. 4 but with 2% Yb^{3+} doping.
6	1	53–20–3–3–17.5–2.5	Same as No. 4 but ZrF_4 was purified by sublimation rather than solvent extraction.
7	2	Unknown	Commercial ZBLAN sample from IPG Photonics.

Experimental Section

ICP-MS Characterization: A Thermo Electron Corporation Element II high-resolution magnetic sector inductively-coupled plasma mass spectrometer (ICP-MS) was used to measure trace metals at various stages during the CASE process. This ICP-MS has a high sensitivity (low parts-per-trillion, ppt) with a linearity over nine orders of magnitude. The purification of Zr^{4+} was chosen as a representative example. Samples were collected immediately before CASE, after each of the CASE steps, and for the UPH water. All samples were digested using hydrogen peroxide and 1:2 $HCl:HNO_3$, then diluted 20-fold to reduce interference of the ammonium acetate buffer with the ICP-MS. The instrument was calibrated using certified [63]Cu, [56]Fe, [59]Co, [58]Ni, [60]Ni, [51]V, [52]Cr, [55]Mn, and [64]Zn standards. The total concentration of each metal was obtained by scaling the measured isotope by its terrestrial abundance. In order to eliminate sample matrix effects

and to account for variations in background readings, 1 ppb of In was added to each sample as an internal standard.

   Powder X-ray Diffraction*:* The phase purity of each metal fluoride was verified by a commercial Rigaku X-ray Diffractometer (XRD) (see Figure 2).
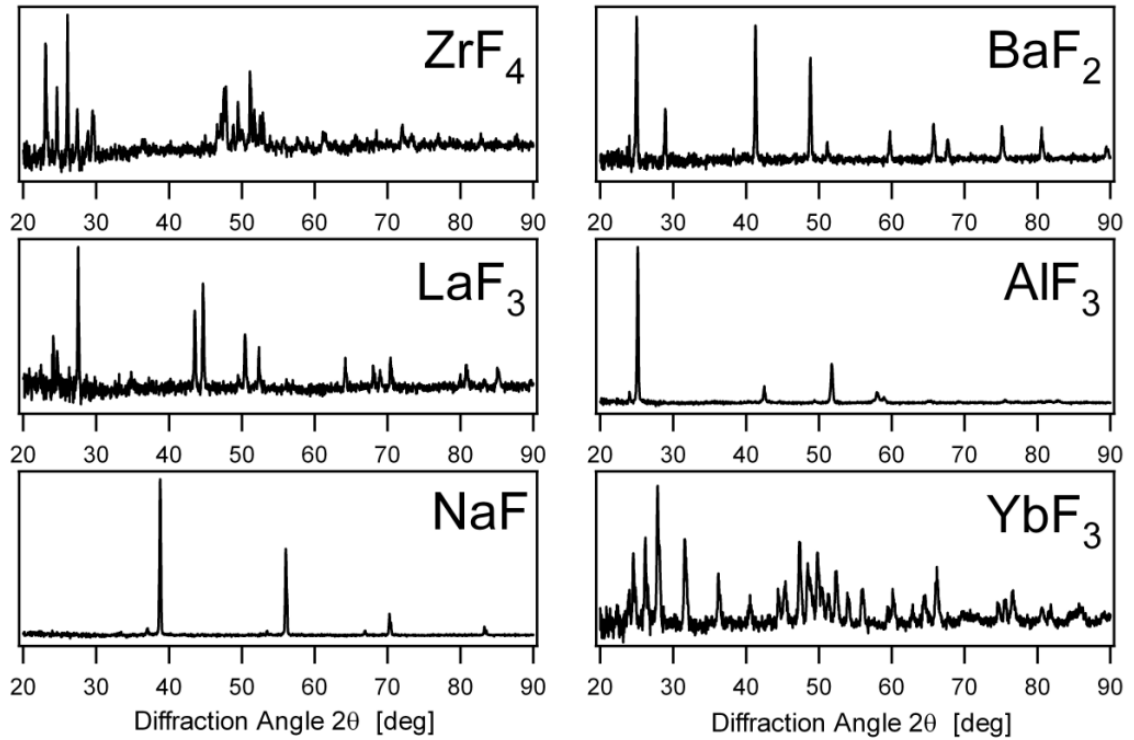
Figure 2. Powder x-ray diffraction for each of the individual fluorides used to fabricate ZBLAN:Yb^{3+}.

   Laser Cooling*:* Two band differential luminescence thermometry (TBDLT) was used to measure local laser-induced cooling or heating in ZBLANI:Yb^{3+} samples and is described in detail elsewhere [36],[37]. TBDLT monitors the luminescence from a sample and deduces laser-induced temperature changes from changes in the spectral distribution, achieving a ~7 mK sensitivity in rare-earth doped materials. Two bands in the luminescence spectrum are optically selected by interference filters that, in

combination with large-core optical fibers and highly amplified, balanced photodetectors, achieve improved optical throughput and higher sensitivity compared to earlier DLT studies. The experiment consists of turning on the laser for a period of time and monitoring the temperature change that occurs due to intrinsic cooling or heating processes, followed by turning off the laser for a period of time for the sample to thermalize back to the ambient temperature. This sequence is repeated, and the signals are averaged over many cycles. The slope of the transient signal is correlated to the laser induced temperature change. The TBDLT technique allows examination of the reduction in efficiency of the laser cooling process due to presence of impurities.

The TBDLT characterization included six Yb^{3+}-doped ZBLANI samples produced in our laboratory (Samples No. 1-6) and a commercial 2% Yb^{3+}-doped ZBLAN sample (IPG Photonics; Sample No. 7) which had shown substantial laser cooling in earlier experiments (see Table 2). The TBDLT parameter, ϑ, which is a quantity proportional to the change in temperature, was measured at room temperature for all six samples. The rate of laser-induced cooling is a measure of the amount of impurities in the material and thus a benchmark for the effectiveness of the purification process.

Results and Discussion

Materials Synthesis: Our strategy for the synthesis of ultra-pure metal fluorides consists of (1) removing transition metal impurities from an aqueous phase by chelate-assisted solvent extraction (CASE) and precipitation of the metal fluoride, (2) removing residual oxidic impurities (such as water, OH^-, and oxides) by drying and fluorination of the "wet" metal fluorides in hot hydrogen fluoride (HF) gas, followed by (3) glass

synthesis in a controlled environment. It is this second drying and fluorination step that enables the preceding aqueous CASE process. Furthermore, the aqueous phase in the CASE process offers many choices for starting materials, as long as the compound can be dissolved and is of relatively high purity. Together, CASE and drying/fluorination in HF gas constitute a purification method that is applicable to the synthesis of a wide range of metal fluorides.

In the present case of purification and synthesis of ZrF_4, BaF_2, LaF_3, AlF_3, NaF, InF_3, YbF_3 for the fabrication of ZBLANI:Yb^{3+} laser cooling glass, we chose metal oxides, carbonates, and chlorides as commercial starting materials (see Table 1). Even the purest commercial starting materials, however, typically contained ppm-level contaminations. For example, a ZBLANI:Yb^{3+} glass prepared from the commercial starting materials in Table 1 without further purification is estimated to have ~16 ppm of transition-metal contamination in the final glass, an impurity level that exceeds the 10 - 100 ppb target by factors of 10^2 - 10^3. Additional purification by CASE was therefore necessary to produce metal fluorides having the < 100 ppb transition-metal impurity levels needed for optical refrigeration.

While purification of an aqueous phase by CASE is effective in reducing transition metals, it always yields metal fluorides with residual oxidic impurities which can be equally detrimental in many applications, including optical refrigeration. Treatment of metal fluorides in hot HF gas is effective in removing these oxidic impurities by two mechanisms: (1) surface water and water of crystallization evaporate from the fluorides as they are heated, and (2) remaining hydroxides and oxides, which are thermodynamically less stable than the respective fluoride react with HF to form the

metal fluoride by releasing water. The initial glasses synthesized and evaluated in this paper (Samples 1-3, see Table 2) were made from fluorides which were dried in HF gas at an unnecessarily high temperature of 550 °C [35]. We found that metal fluorides exposed to HF at this temperature had a grayish tint, and a brownish gelatinous residue emerged from the output port of the drying vessel during the HF process. These residues were likely a result of corrosion of the Inconel Alloy 600 parts and the glassy carbon inserts. We have found that lowering the drying temperature to 300 °C eliminated these corrosion residues and resulted in white metal fluoride powders. This lower HF process temperature is also supported by results reported by Kwon et al. who have shown that finely powdered CeO_2, Nd_2O_3, and SrO can be quantitatively converted to the respective fluorides by exposure to 33 vol% HF in argon at 300 °C in less than 1 hour [38]. We therefore expect the drying/fluorination in our apparatus (19 hours at 300 °C in ~7 vol% HF in argon; see the Materials Synthesis Section) to be highly effective in removing oxidic impurities.

All glass fabrication steps - including melting, casting, quenching, and annealing - were carried out inside an argon filled drybox, equipped with HEPA filters, containing less than 0.1 ppm of O_2 and < 0.6 ppm H_2O. Such an inert atmosphere was necessary to suppress the formation of oxides during melting of the fluoride glass. Oxides can increase multiphonon absorption, increase the tendency of glass to crystallize, increase light scattering, and decrease chemical durability [39]. A practical limit for the ZBLAN:Yb^{3+} melting temperature is set by the volatilization rate of ZrF_4, which sublimes at 600°C. Preheating the furnace was necessary to prevent excess sublimation of ZrF_4 from the batch of precursor fluoride powders before melting occurred. The optimized melting and

68

annealing schedule described in the Materials Synthesis Section yielded mechanically rugged samples of excellent optical quality.

Effectiveness of Chelate-Assisted Solvent Extraction: ICP-MS was used to quantify the effectiveness of removing transition-metal impurities (Cu, Fe, Co, Ni, V, Cr, Mn, Zn) from the aqueous metal-ion solutions. Zirconium was chosen as the relevant test case because the final product, ZrF_4, amounts to more than half of the final ZBLANI glass composition. The UHP water, which was used extensively throughout the CASE process, was also analyzed for transition-metal impurities, both to verify its purity and to establish a point of reference. None of the measured transition-metal ions were detected in the UHP water within the detection limits of the ICP-MS. We also analyzed the doubly distilled acids, the buffer solution, and the hydrogen peroxide used in the CASE process and ICP-MS sample preparation. Transition metal concentrations in these reagents were found to be negligible, indicating that any significant transition-metal impurities detected in the solutions were introduced by the $ZrCl_2O$ starting material.

Figure 3 shows the concentrations of each of the transition metal impurities (on a log-scale, in ppb) at various stages of the zirconium solution purification process. The "Before CASE" sample was the buffered aqueous $ZrCl_2O$ solution taken directly before the first CASE step. This initial $ZrCl_2O$ solution was substantially contaminated, having a total of ~72,500 ppb of the measured transition metals, the majority of which was Fe. The remaining three samples shown in Figure 3 were taken after each of the three successive solvent extraction steps. In most cases, each solvent extraction step reduced the transition metal concentration. The extraction coefficients (percentage of impurity removed per step) for the first CASE step were found to be 99.3% (Mn), 98.7% (Fe), Co

(98.3%), 98.0% (Ni), 95.6% (Cr), 94.1% (Zn), and 84.5% (V). These values are consistent with earlier reports of solvent extraction using the APDC chelate in a water/MIBK two-phase system [31],[40],[41]. These extraction coefficients also illustrate that at least two extraction steps are needed to reduce the initial concentration by 10^3 for most transition metals. It is also noteworthy that the apparent extraction coefficients were generally lower for the second and third extraction steps (where applicable), indicating that possible recontamination masked the effect of the chelate at concentrations < 50 ppb. This is seen for Zn and Cr, for which a slight increase in the concentration (although still < 35 ppb) after the third extraction step was observed.
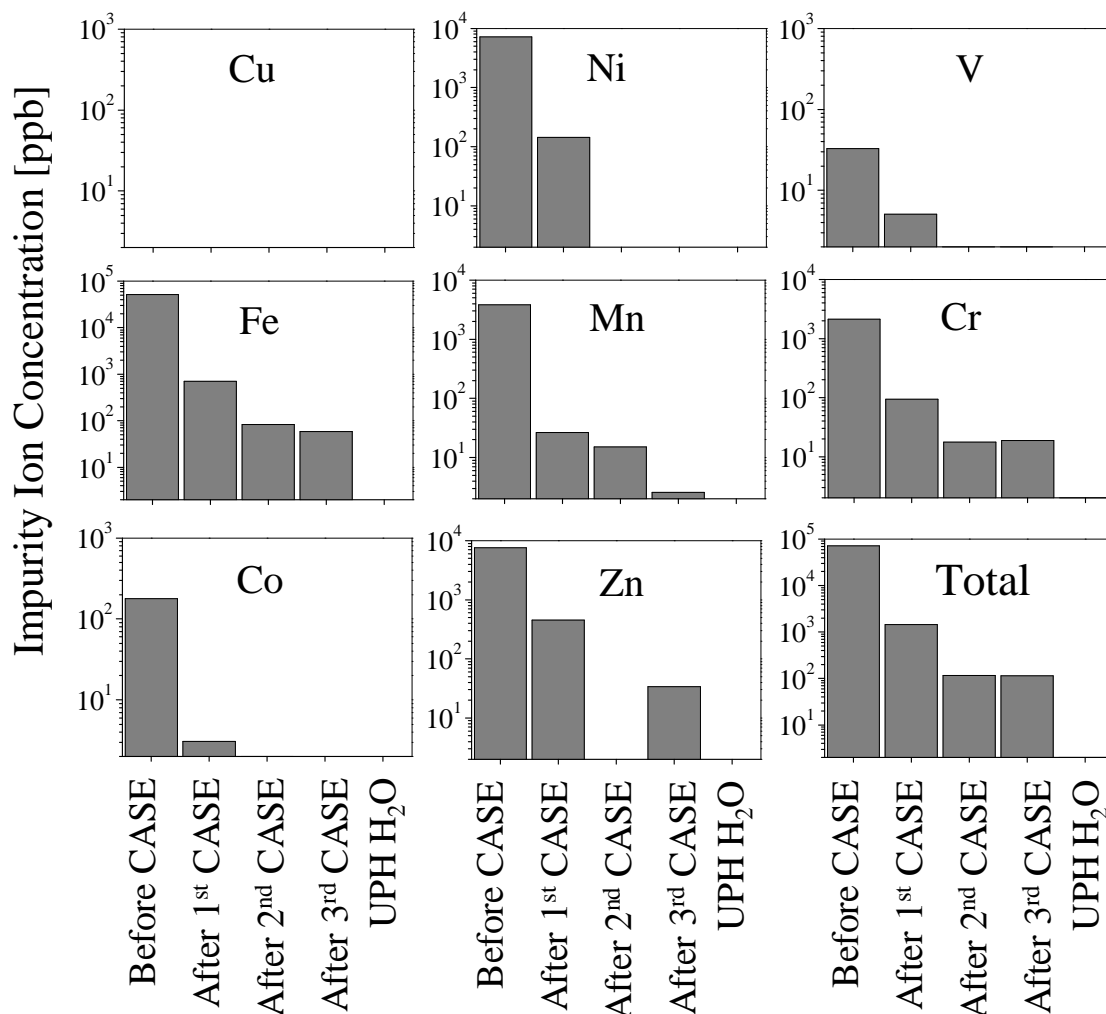
Figure 3. Results from ICP-MS analysis of the chelate assisted solvent extraction (CASE) purification of a $ZrCl_2O$ solution. Reference standards were prepared for 8 transition metal ions known to be deleterious to numerous applications which rely on ultra-pure fluorides. The solution was analyzed before CASE, and after each successive CASE step. Note the different axis scales for the various graphs.

Overall, the first CASE step was able to reduce the total concentration of the measured transition metals from ~72500 ppb to ~1400 ppb, with the residual impurities consisting primarily of Fe, but also Zn and Cr. The second CASE step further reduced the total impurity concentration from ~1400 ppb to ~100 ppb. The third CASE step did not reduce

impurity levels any further and appears to be ineffective. Hydrofluoric acid was added to the aqueous solution after the third CASE step to precipitate $ZrF_6(NH_4)_3$ which was then decomposed to $ZrF_4.H_2O$ (see the Materials Synthesis Section). The residual transition metal impurities in the final zirconium solution (see Figure 3) are therefore considered to be representative of the purity in the final fluoride $ZrF_4.H_2O$ (before HF gas drying/fluorination). The impurity level of ~100 ppb compares favorably with the estimated maximum impurity level of 10-100 ppb required for efficient optical refrigerator materials.

Table 3. Transition metal concentration (ppb) in a $ZrCl_2O$ solution before and after CASE. This data is presented as a series of bar graphs in Figure 3.

	Cu	Fe	Co	Ni	V	Cr	Mn	Zn	Total
Before CASE	0	51600	177	7130	32.8	2140	3820	7640	72500
After 1st CASE	0	711	3.09	143	5.07	93.9	26.4	454	1440
After 2nd CASE	0	83.0	0.078	0	0.695	17.5	15.1	0	116
After 3rd CASE	0	58.5	0	0	1.10	18.6	2.56	33.9	115
UHP H_2O	0	0	0	0	0	0.147	0	0	0.147

Laser Cooling: Laser cooling removes thermal energy from a solid by anti-Stokes fluorescence and thereby reduces its temperature. A comprehensive introduction to laser refrigeration has been given elsewhere [11]. Impurities can introduce several

undesirable processes that cause internal heating and therefore degrade the laser cooling performance. The primary quenching mechanism is by non-radiative energy transfer from the excited laser cooling ion (e.g. Yb^{3+}) to transition metal impurities (such as Cu^{2+}, Fe^{2+}, Co^{2+} and Ni^{2+}) which subsequently decay non-radiatively. Furthermore, impurities with high-energy vibrational modes (such as OH^- and H_2O) can quench the excited state of the laser cooling ion via multi-phonon relaxation. Finally, impurities can also directly absorb at the pump wavelength causing heating in the form of background absorption. Reducing transition metal and oxidic impurities suppresses these impurity-induced undesired decay channels and thus improves the laser cooling performance. The TBDLT characterization method (see the Experimental Section) provides a measure of the laser-cooling efficiency of a material and, therefore, an indirect measure of the aggregate impurity concentration.

Each sample listed in Table 2 was characterized by TBDLT to measure the degree of laser cooling via the parameter ϑ (see Figure 4). Sample No. 1 clearly illustrates that even the best commercial metal fluorides have insufficient purity to enable laser cooling; this sample showed substantial laser-induced heating even at room temperature. The use of CASE purification of precursor materials, sufficiently high InF_3 oxidizer concentration, optimized hydrogen fluoride drying, and sufficiently long melting times, provided a substantial improvement of laser cooling performance (successive implementation of these processes in samples No. 2, 3, and 4). The 1% Yb^{3+} concentration of Sample No. 4 was increased to 2% in Sample No. 5, which resulted in substantial heating. The rate of energy migration among Yb^{3+} ions increases with increasing Yb^{3+} concentration, and some of the excitations can find impurity sites where non-radiative relaxation takes place. This process is more efficient in the 2% sample (No.

5) compared to the 1% sample (No. 4), and the fact that sample No. 5 showed substantial heating is direct evidence for the presence of transition metal and/or oxidic impurities. Also note that the use of ZrF_4 purified by sublimation (at the University of Bern; sample No. 6) resulted in a sample that cooled, albeit not as much as the best sample fabricated from precursors purified by the CASE process.
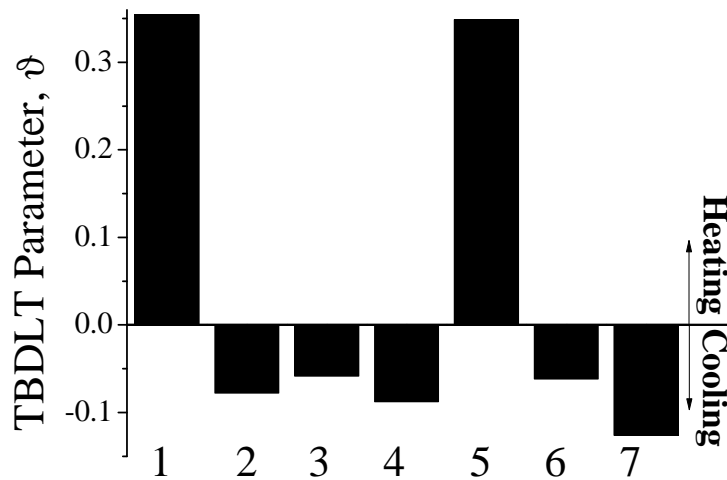
Figure 4. TBDLT parameter at 300 K measured for each of the samples in Table 2. ϑ is proportional to the laser-induced change in temperature, where a positive and negative TBDLT parameter corresponds to laser-induced heating and cooling, respectively. Samples 2-4 exhibited laser cooling, indicating that the CASE purification and HF drying/fluorination were successful in significantly reducing transition-metal and oxidic impurities.

Conclusions

A comprehensive purification method suited for all of the ZBLANI:Yb^{3+} glass constituents had not yet been reported and was presented here. We show that chelate assisted solvent extraction (CASE) using APDC as a chelate and MIBK/water as a two-

phase system is effective in removing relevant transition metal impurities from a $ZrCl_2O$ solution. The transition metal contamination was reduced by almost a factor of 10^3, and a residual transition metal concentration of ~100 ppb was achieved. Subsequent drying and fluorination of the resulting metal fluorides in hot hydrogen fluoride (HF) gas has proven effective in removing residual oxidic impurities, as confirmed by laser cooling measurements. Current work is focused on optimization of CASE with the APDC chelate and on finding other chelates/solvent systems with improved characteristics. The suite of processes presented here is applicable to the preparation of a wide range of ultra-pure binary fluorides, and it established a foundation for the growth of a variety of fluoride crystals and glasses for demanding photonic applications.

ACKNOWLEDGMENTS

REFERENCES

[1]   T. M. Bloomstein, M. W. Horn, M. Rothschild, R.R. Kunz, S.T. Palmacci, R.B. Goodman, "Lithography with 157 nm lasers," J. Vac. Sci. Technol. B **15**, 2112 (1997).

[2]   S. Sudo, "Progress in Optical Fiber Amplifiers," in *Current Trends in Optical Amplifiers and their Applications*, T. P. Lee ed., (World Scientific, New Jersey, 1996) pp. 19-21.

[3]   T. G. Brown, in *Fiber Optics Handbook: Fiber, devices and systems for optical communications*, M. Bass and E. W. Van Stryland, eds., (McGraw-Hill, NY, 2002), Chapter 1: Optical fibers and fiber-optic communications, pp. 1-49.

[4]   S. Bedo, M. Pollnau, W. Luthy, and H. P. Weber, "Saturation of the 2.71 um laser output in erbium-doped ZBLAN fibers," Opt. Commun. **116,** 81–86 (1995).

[5]   X. Zhu and R. Jain, "Numerical analysis and experimental results of high-power Er/Pr:ZBLAN 2.7 um fiber lasers with different pumping designs," Applied Optics **45** [27], 20 (2006).

[6]   T. Sakamoto, M. Shimizu, M. Yamada, T. Kanamori, Y. Ohishi, Y. Terunuma, and S. Sudo, "35 dB gain Tm-doped ZBLAN fiber amplifier operating at 1.65 um," *Tech. Digest of CLEO/Pacific Rim* PD2.12, July 1995.

[7]   B. Pedersen, W. J. Miniscalo, and R. S. Quimby, "Optimization of Pr^{3+}:ZBLAN fiber amplifiers," IEEE Photonics Technol. Lett **4** [5], 446-448 (1992).

[8]   D. F. Anderson, "Cerium fluoride: a scintillator for high-rate applications," Nucl. Instrum. Methods Phys. Res. **A287** [3], 606-612, 1990.

[9]   E. Auffray, D. Bouttet, I. Dafinei, J. Fay, P. Lecoq, J. A. Mares, M. Martini, G. Maze, F. Meinardi, B. Moine, "Cerium doped heavy metal fluoride glasses, a possible alternative for electromagnetic calorimetry," Instrum. Methods Phys. Res. **A380** [3], 524-536, 1996.

[10]   J. Freek Suijver, in *Luminescence: From Theory to Applications*, C. Ronda ed., (Wiley-VCH, Weinheim, 2008), Chapter 6: Upconversion Phosphors, pp. 133-175.

[11]   R. I. Epstein and M. Sheik-Bahae, eds., in *Optical Refrigeration. Science and Applications of Laser Cooling of Solids*, (Wiley, Weinheim, 2009).

[12] Y. Ohishi, S. Mitachi, T. Kanamori and T. Manabe, "Optical Absorption of 3d Transition Metal and Rare Earth Elements in Zirconium Fluoride," Phys. Chem. Glasses **24** [5], 135 (1983).

[13] S. Mitachi, T. Miyashita and T. Manabe, "Preparation of fluoride optical fibres for transmission in the mid-infrared," Phys. Chem. Glasses **23**, 196-102 (1982).

[14] E. O. Gbogi, K. H. Chung, and C. T. Moynihan, "Surface and Bulk-OH infrared absorption in ZrF_4- and HfF_4-based Glasses," Commun. Amer. Ceram. Soc. **C-51**, (1981).

[15] P. W. France, S. F. Carter, J. R. Williams, K. J. Beales, "OH absorption in fluoride glass infrared fibers," Electron. Lett. **20**, 607 (1984).

[16] P. C. Schultz, L. J. B. Vacha, C. T. Moynihan, B. B. Harbison, K. Cadien, and R. Mossadegh, "Hermetic Coatings for Bulk Fluoride Glasses and Fibers," Mater. Res. Soc. Symp. Proc. **19**, 343 (1987).

[17] H. Poignant, "Role of impurities in halide glasses," NATO ASI Series E **123**, 35 (1987).

[18] P. Kaiser, A. R. Tynes, H. W Astle, A.D. Pearson, W. G. French, R. E. Jaeger, A. H. Cherin, "Spectral losses of unclad vitreous silica and soda-lime-silicate fibers," J. Opt. Soc. Am. **63**, 1141 (1973).

[19] P. W. France, S. F. Carter, J. R. Williams, "Absorption in fluoride glass infrared fibers," J. Am. Ceram. Soc. **67**, C243 (1984).

[20] M. Poulain, M. Saad, "Absorption loss due to complex anions in fluorozirconate glasses," J. Lightwave. Tech. **LT-2**, 599 (1984).

[21] J. M. Jewell, J. Coon, J. E. Shelby, "The extinction coefficient for CO_2 dissolved in a heavy metal fluoride glass," Mat. Sci. Forum **32–33**, 421 (1988).

[22] M. P. Hehlen, R. I. Epstein, and H. Inoue, "Model of laser cooling in the Yb^{3+}-doped fluorozirconate glass ZBLAN," Phys. Rev. B **75** [14], 144302 (2007).

[23] D. R. MacFarlane, P. J. Newman and A. Voelkel, "Methods of purification of zirconium tetrafluoride for fluorozirconate glass," J. Am. Ceram. Soc. **85** [6], 1610-12 (2002).

[24] B. E. Kinsman and R. Hanney, "Preparation and purification of metal fluorides for crystals and glasses," Adv. Matls. for Opt. and Elect. **5**, 109-115 (1995).

[25]   A. M. Mailhot, A. Elyamani, and R. E. Riman, "Reactive atmosphere synthesis of sol-gel heavy metal fluoride glasses," J. Mater. Res. **7** [6], 1534-1540 (1992).

[26]   M. G. Drexhage, C. T. Moynihan, B. Bendow, E. Gbogi, K. K. Chung, and M. Boulos, "Influence of processing conditions on IR edge absorption in fluorohafnate and fluorozirconate glasses," Mater. Res. Bull **16**, 943-947 (1981).

[27]   M. Jardin, J. Guery, and C. Jacoboni, "Preparation in vapour state of fluoride glass components by a chemical vapour deposition process," J. Non-Cryst. Solids **184**, 204-208 (1995).

[28]   Y. Nishida, K. Fujiura, H. Sato, S. Sugawara, K. Kobayashi and S. Takahashi, "Preparation of ZBLAN fluoride glass particles by chemical vapor deposition process," Jpn. J. Appl. Phys. Part 2 **31** [12A], 1692-1694 (1992).

[29]   K. Fujiura, Y. Ohishi, M. Fujiki, T. Kanamori, S. Takahashi, "Process for the preparation of fluoride glass and process for the preparation of optical fiber perform using the fluoride glass," U.S. Patent 5,071,460 (1991).

[30]   D. Bertrand, J. Guery, C. Jacoboni, "Fe, Co, Ni, Cu trace metal analysis in ZBLAN fluoride glasses," J. Non-Cryst. Solids **161,** 32 (1993).

[31]   R. R. Brooks, M. Hoashi, S. M. Wilson, and R. Zhang, "Extraction into methyl isobutyl keytone of metal complexes with ammonium pyrrolidine dithiocarbamate formed in strongly acidic media," Analytica Chimica Acta **217**, 165-170 (1989).

[32]   J. D. Kinrade, J. C. Van Loon, "Solvent extraction for use with flame atomic absorption spectrometry," Anal. Chem. **46**, 1894 (1974).

[33]   Z. Ling, Z. Chengshan, D. Gaozian, and W. Kangkang, "$ZrOCl_2$ for fluoride glass preparation," J. Non-Cryst. Solids **140**, 331-334 (1992).

[34]   R. Burkhalter, I. Dohnke, J. Hulliger, "Growing of Bulk Crystals and Structuring Waveguides of Fluoride Materials for Laser Applications," Progress in Crystal Growth and Characterization of Materials **42**, 1-64 (2001).

[35]   K. W. Krämer, D. Biner, G. Frei, H.U. Güdel, M.P. Hehlen, S.R. Lüthi, "Hexagonal sodium yttrium fluoride based green and blue emitting upconversion phosphors", Chem. Mater., **16**, 1244-1251 (2004).

[36]   W. M. Patterson, M. P. Hehlen, , R. I. Epstein, M. Sheik-Bahae, "Synthesis and evaluation of ultra-pure rare-earth-doped glass for laser refrigeration," Proc. SPIE 7228, 72280C (2008).

[37]   M. P. Hehlen, W. M. Patterson, R. I. Epstein, "Synthesis of ultrapure ZBLAN glass for laser refrigeration," Proc. SPIE 6907, 69070A (2008).

[38]   S. W. Kwon, E. H. Kim, B. G. Ahn, J. H. Yoo, H. G. Ahn, "Fluorination of metals and metal oxides by gas–solid reaction," J. Ind. Eng. Chem. **8**, 477 (2002).

[39]   M. Poulain, J. Lucas, and P. Brun, "Verred fluores au tetrafluorure de zirconium. Proproetes optiques d'un verre dope au Nd^{3+}," Mat. Res. Bull **10**, 243 (1975).

[40]   H. Malissa, E. Schöffmann, "Über die Verwendung von substituierten Dithiocarbamaten in der Mikroanalyse," Mikrochim. Acta **1**, 187 (1955).

[41]   M. Arnac, G. Verboom, "Solubility product constants of some divalent metal ions with ammonium pyrrolidine dithiocarbamate," Anal Chem. **46**, 2059 (1974).

Chapter 4

Model of laser-induced temperature changes in solid-state optical refrigerators

W.M. Patterson[*,1], M. Sheik-Bahae[1], R.I. Epstein[2], M.P. Hehlen[2]

[1]   800 Yale Blvd. NE, Albuquerque, NM 87131

[2]   Los Alamos National Laboratory, Los Alamos, NM 87545, USA

[*]   Corresponding Author: wendy5@unm.edu, 505-277-3301

Abstract

We present an efficient and numerically stable method to calculate time-dependent, laser-induced temperature distributions in solids and provide a detailed description of the computational procedure and its implementation. This study combines the two-dimensional heat equation with laser-induced heat generation and temperature-dependent luminescence. The time-dependent optical response of a system is obtained numerically by the Crank-Nicolson method. This general model is applied to the specific case of optical refrigeration in ytterbium (Yb^{3+}) doped fluorozirconate glass (ZBLAN). The laser-induced temperature change upon optical pumping and the respective transient

luminescence response are calculated and compared to experimental data. The model successfully predicts the zero-crossing temperature, the net quantum efficiency, and the functional shape of the transients. We find that the laser-cooling transients have a fast and a slow component that are determined by the excited-state lifetime of the luminescent ion and the thermal properties of the bulk, respectively. The tools presented here may find application in the design of a wide range of optical and opto-electronic devices.

I. Introduction

Thermal processes in luminescent materials are a critical factor determining the performance of solid state optical refrigerators [1], laser gain materials [2], display and lamp phosphors [3], solid-state lighting devices [4]-[6], luminescent biomarkers [7]-[9], and fiber lasers and amplifiers. Light-induced heating also plays a key role in laser ablation [10], photothermal therapy [11]-[13], laser-induced damage of tissue, and thermal lensing. While the fundamental aspects of this problem are readily comprehended from the basic heat equation, actual calculations of time-dependent laser-induced temperature gradients are more challenging and often require advanced numerical tools and considerable computational power[14],[15]. The concept of laser-induced heating in general has been studied extensively [16]-[18], but no comprehensive model of laser-induced heat diffusion and its effect on luminescence in bulk solids exists.

This paper presents an efficient and numerically stable method to calculate time-dependent laser-induced temperature distributions in solids and provides a detailed description of the computational procedure and its implementation. In addition, we

81

introduce a temperature dependent material property, in this case luminescence from a rare-earth ion, and show that the respective transient response of the system upon optical pumping is predicted correctly by the model. To our knowledge, this study is the first to combine the heat equation with temperature-dependent luminescence in order to predict the time-dependent optical response of a system. The tools presented here may find application in the design of a wide range of optical and opto-electronic devices.

As an example, we apply the method to optical refrigeration in the Yb^{3+} doped fluorozirconate glass ZBLAN (ZrF_4-BaF_2-LaF_3-AlF_3-NaF). The development of laser-cooling materials and devices has made significant progress over the past decade [19], [1]. The focus has been primarily on the study of a variety of rare-earth doped materials and ways to fabricate them in the exceedingly high purity and optical quality required for laser cooling applications. However, a quantitative description of the dynamics of laser-induced cooling is still needed and is critical for the characterization of laser-cooling materials as well as for the design and performance optimization of actual optical cryocooler devices. The relaxation of excited rare-earth ions in solids involves both radiative and non-radiative processes. The non-radiative processes are exothermic in most rare-earth doped materials, that is, net heat is deposited into the host, and the material heats as a result of laser excitation. Both radiative and non-radiative processes also occur in laser-cooling materials; but here, the net result of the non-radiative processes is endothermic, and the material cools as a result of laser excitation. Two-band differential luminescence thermometry (TBDLT), a technique that measures laser-induced changes in the luminescence spectrum in the time domain to infer subtle changes in internal sample temperature [19], builds on transient laser-induced temperature

82

changes and serves as a test of the model developed in this study. We show that the model correctly predicts the time-dependence of the TBDLT signal and finds that the transients have a fast and a slow component that are determined by the excited-state lifetime of the luminescent ion and the thermal properties of the bulk, respectively.

In Section II, the two-dimensional heat equation is introduced, laser-induced internal thermal processes in a two-level system are incorporated, and a formal description of TBDLT is presented. Section III applies the model to laser cooling in ZBLAN:Yb^{3+} glass and compares the calculated performance with experimental TBDLT transients.

II.   Model of Time-Dependent Laser-Induced Heating in Solids

Consider a rectangular solid sample that is excited by a single-mode laser focused into the center of the bulk material. If scattering can be neglected, laser-induced radiative and non-radiative processes will occur over the focused range of the laser, that is over $2z_R$ in the longitudinal direction, where $z_R = \omega_0^2 \pi / \lambda_p$ is the Rayleigh range. Temperature changes in the longitudinal direction over the Rayleigh range will be minimal, and the three-dimensional system can be approximated by a two-dimensional (2D) transverse slab with thickness $2z_R$. We will first present the well-known 2D heat equation, describe the numerical method for solving the respective differential equations (Section II.A), and subsequently introduce laser-induced heating (Section II.B). Section III.C introduces a formal description of two-band differential luminescence thermometry

(TBDLT) that will be used as example and validation of the model developed in this section.

A.   The 2D Heat Equation and the Crank-Nicolson Method

The diffusion of heat is governed by the heat equation, which follows from the Fourier Law and conservation of energy. The Fourier Law,

$$\vec{\phi}_q = -\kappa \nabla T, \tag{1}$$

states that the local heat flux $\vec{\phi}_q$ is proportional to the temperature gradient ∇T. Note that the thermal conductivity, κ, generally varies with temperature and direction in anisotropic materials, in which case κ becomes a tensor. In the following we shall ignore both these dependencies. Assuming that no work is being performed, the change in internal energy per unit volume, ΔQ, is proportional to the change in temperature, ΔT, that is

$$\Delta Q = C_p \rho \Delta T. \tag{2}$$

We now assume that the specific heat capacity, C_p, and the mass density, ρ, are both independent of temperature. In the absence of internal heat generation, the change in internal energy must be accounted for entirely by heat flux across the boundaries, and therefore the change in internal heat and the heat flow across the boundary must be equal. This yields the heat equation, which in the 2D case is given by

$$\frac{\partial T(x,y,t)}{\partial t} = \frac{\kappa}{C_p \rho} \left[\frac{\partial^2 T(x,y,t)}{\partial x^2} + \frac{\partial^2 T(x,y,t)}{\partial y^2} \right]. \tag{3}$$

In Eq.(3), $T(x,y,t)$ is the temperature (in K) at time t (in s) and location (x, y) (in m), κ is the thermal conductivity (in W m^{-1} K^{-1}), ρ is the mass density (in kg m^{-3}), and C_p is the

specific heat capacity (in J kg^{-1} K^{-1}). The heat equation is a second-order partial differential equation (PDE), specifically it is a parabolic PDE. Note that this equation does not account for internal heat generation, which is added as a source term later in this section (Eq.(7)) when the equation is solved using the Crank-Niholson formalism.

The heat equation can only be solved analytically in a few cases and usually must be evaluated numerically, especially in two and three dimensional problems. Several explicit and implicit numerical methods exist for this purpose. Explicit methods calculate the state of the system $Y(t+\Delta t)$ at a later time $t+\Delta t$ from the state of the system $Y(t)$ at the current time t, that is $Y(t+\Delta t)=F(Y(t))$. Implicit methods on the other hand solve an equation that contains both the current and the later state of the system, that is $G(Y(t),Y(t+\Delta t))=0$. Explicit methods are easier to implement than implicit methods, however they often fail because the PDEs tend to be unstable unless Δt is chosen to be extremely small, which makes explicit methods slow and sensitive to round off errors. In contrast, implicit methods require upfront computation that is usually more than offset by their advantages of unconditional stability and larger time steps.

The Crank-Nicolson (CN) scheme is an implicit method [21] that is a particularly powerful approach for numerically solving parabolic PDEs such as the heat equation. It is a second order method that is implicit in time and that is numerically stable. In the 2D case on a uniform Cartesian coordinate grid, the heat equation in the CN-scheme becomes [21]

$$
\begin{aligned}
(1+2\mu)T_{i,j}^{n+1} &- \left(\frac{\mu}{2}\right)\left(T_{i+1,j}^{n+1}+T_{i-1,j}^{n+1}+T_{i,j+1}^{n+1}+T_{i,j-1}^{n+1}\right) \\
&= (1-2\mu)T_{i,j}^{n} + \left(\frac{\mu}{2}\right)\left(T_{i+1,j}^{n}+T_{i-1,j}^{n}+T_{i,j+1}^{n}+T_{i,j-1}^{n}\right),
\end{aligned}
\tag{4}
$$

where $T_{i,j}^n$ is the temperature at time step n and at grid location (i, j). μ is the dimensionless Courant-Friedrichs-Lewy (CFL) number for the two-dimensional case and is given by [22]

$$\mu = \frac{\kappa \Delta t}{\rho C_p (\Delta d)^2},$$

(5)

where Δd is the lattice constant of the Cartesian square grid that comprises N x N cells. These quantities are illustrated in Figure 1. Equation (4) can be written in matrix notation as

$$\left[\mu^{n+1}\right]\left[T^{n+1}\right] = \left[\mu^n\right]\left[T^n\right],$$

(6)

where $\left[T^{n+1}\right]$ and $\left[T^n\right]$ are one-dimensional matrices of length N^2 containing the temperatures at locations (i, j) for time step $n+1$ and n, respectively. $\left[\mu^{n+1}\right]$ and $\left[\mu^n\right]$ are two-dimensional matrices of size N^2 x N^2 that contain the $1 \pm 2\mu$ and $\pm \mu/2$ factors in Eq.(4) as well as the boundary conditions (see Section II.A.2). In the presence of internal thermal processes (e.g. laser-induced heating or cooling) with power P, $\Delta Q = P \Delta t$ of thermal energy will be deposited into the material during the time interval Δt. According to Eq.(2), this will raise the temperature by $\Delta T = \Delta Q / C_p \rho = P \Delta t / C_p \rho$. The temperature at time step $n+1$ can now be found by multiplying Eq.(6) with the inverse of matrix $[\mu^{n+1}]$, and adding the effect of this additional heat source such that

$$\left[T^{n+1}\right] = \left[\mu^{n+1}\right]^{-1}\left[\mu^n\right]\left[T^n\right] + \left[\Delta T^n\right].$$

(7)

$$\left[T^{n+1} \right] = \left[\mu^{n+1} \right]^{-1} \left[\mu^{n} \right] \left[T^{n} \right]$$

	T_{11}^{n+1}	T_{21}^{n+1}	..	T_{i1}^{n+1}
T_{11}^{n}	T_{21}^{n}	..	T_{i1}^{n}	
T_{12}^{n}	T_{22}^{n}			
:				T_{NN}^{n+1}
T_{1j}^{n}			T_{NN}^{n}	

Figure 1 Definition of quantities for the Crank-Nicolson method in a two-dimensional square grid.

$[\mu^{n+1}]$ and $[\mu^{n}]$ are constant for a given system if κ and C_p in Eq.(5) are assumed to be independent of temperature. If that is a good approximation, $[\mu^{n+1}]^{-1}[\mu^{n}]$ can be computed up front, and the method then proceeds efficiently from one time step to the next by the simple matrix multiplication of Eq.(7) (see Figure 1), yielding the time-dependent spatial temperature distribution. The following subsections describe the structure of the μ–matrices, the implementation of boundary and initial conditions, and the choice of time step in the numerical evaluation of Eq.(7).

1. Structure of the μ-Matrices

The μ-matrices in Eq.(7) are sparse and have a band-diagonal structure with non-zero elements only on the diagonal and on two diagonals on either side. The bandedness is a result of the heat flow being local, i.e. heat only flowing between neighboring cells. A sparse matrix with a band-diagonal structure is computationally easier to invert than a

dense matrix; however, we have not taken advantage of this property in the numerical implementation used in this study and have used a standard matrix inversion routine.

Let us denote the diagonal and off-diagonal elements of the μ - matrices in Eq.(4) by a_0 and a_1, respectively. For the $[\mu^{n+1}]$ and $[\mu^n]$ matrices, these elements then become:

$$
\begin{aligned}
a_0^{n+1} &= 1 + 2\mu & a_1^{n+1} &= -\mu/2 & (a) \\
a_0^{n} &= 1 - 2\mu & a_1^{n} &= \mu/2 & (b).
\end{aligned}
\tag{8}
$$

To illustrate the structure of the resulting μ-matrices, let us consider a simple 2D-system consisting of 4×4 cells. The right hand side of Eq.(6) can be explicitly written as shown in **Figure 2** using the definitions in Eq.(8) (b). The matrix structure of the left-hand side of Eq.(6) is identical but uses the elements defined in Eq.(8) (a). Note that the μ-matrix consists of N rows of N rows, i.e. it has one row for every cell of the N x N Cartesian grid.

$$\begin{pmatrix} a_0^n & a_1^n & . & . & a_1^n & . & . & . & . & . & . & . & . & . & . & . \\ a_1^n & a_0^n & a_1^n & . & . & a_1^n & . & . & . & . & . & . & . & . & . & . \\ . & a_1^n & a_0^n & a_1^n & . & . & a_1^n & . & . & . & . & . & . & . & . & . \\ . & . & a_1^n & a_0^n & . & . & . & a_1^n & . & . & . & . & . & . & . & . \\ a_1^n & . & . & . & a_0^n & a_1^n & . & . & a_1^n & . & . & . & . & . & . & . \\ . & a_1^n & . & . & a_1^n & a_0^n & a_1^n & . & . & a_1^n & . & . & . & . & . & . \\ . & . & a_1^n & . & . & a_1^n & a_0^n & a_1^n & . & . & a_1^n & . & . & . & . & . \\ . & . & . & a_1^n & . & . & a_1^n & a_0^n & . & . & . & a_1^n & . & . & . & . \\ . & . & . & . & a_1^n & . & . & . & a_0^n & a_1^n & . & . & a_1^n & . & . & . \\ . & . & . & . & . & a_1^n & . & . & a_1^n & a_0^n & a_1^n & . & . & a_1^n & . & . \\ . & . & . & . & . & . & a_1^n & . & . & a_1^n & a_0^n & a_1^n & . & . & a_1^n & . \\ . & . & . & . & . & . & . & a_1^n & . & . & a_1^n & a_0^n & . & . & . & a_1^n \\ . & . & . & . & . & . & . & . & a_1^n & . & . & . & a_0^n & a_1^n & . & . \\ . & . & . & . & . & . & . & . & . & a_1^n & . & . & a_1^n & a_0^n & a_1^n & . \\ . & . & . & . & . & . & . & . & . & . & a_1^n & . & . & a_1^n & a_0^n & a_1^n \\ . & . & . & . & . & . & . & . & . & . & . & a_1^n & . & . & a_1^n & a_0^n \end{pmatrix} \begin{pmatrix} T_{1,1}^n \\ T_{2,1}^n \\ T_{3,1}^n \\ T_{4,1}^n \\ T_{1,2}^n \\ T_{2,2}^n \\ T_{3,2}^n \\ T_{4,2}^n \\ T_{1,3}^n \\ T_{2,3}^n \\ T_{3,3}^n \\ T_{4,3}^n \\ T_{1,4}^n \\ T_{2,4}^n \\ T_{3,4}^n \\ T_{4,4}^n \end{pmatrix}$$

Figure 2 Structure of the matrices on the right side of Eq.(6) for the example of a 4×4 Cartesian grid. Zero elements are represented by dots for clarity.

2.   **Boundary Conditions and Initial Conditions**

One can choose either Dirichlet boundary conditions, that hold the boundary at a given temperature, or Neumann boundary conditions, that hold the boundary at a given heat flow rate (e.g. imperfect insulation). Here we choose Dirichlet boundary conditions which place the system in a bath with infinite heat capacity and a fixed temperature, i.e. the temperature of the cells around the perimeter of the N x N system does not change. Specifically, these are the cells in the top row, bottom row, left column, and right column of the N x N Cartesian grid (see Figure 1). The matrix elements for these cells have to be modified to ensure constant temperature. Specifically, the first and last N rows of the above μ - matrix (see Figure 2) correspond to the top and bottom row of the N x N

Cartesian grid, respectively, and the respective diagonal elements are replaced by 1 and the respective off-diagonal elements by 0. In each of the other blocks of N rows, the first row and last row correspond to the left and right column of the N x N Cartesian grid, respectively; again, the respective diagonal elements are replaced by 1 and the respective off-diagonal elements by 0 to ensure constant temperature. With these boundary conditions, the matrix structure of the right side of Eq.(6) (see Figure 2) is modified to the structure shown in Figure 3.

$$
\left(
\begin{array}{cccc:cccc:cccc:cccc}
1 & . & . & . & . & . & . & . & . & . & . & . & . & . & . & . \\
. & 1 & . & . & . & . & . & . & . & . & . & . & . & . & . & . \\
. & . & 1 & . & . & . & . & . & . & . & . & . & . & . & . & . \\
. & . & . & 1 & . & . & . & . & . & . & . & . & . & . & . & . \\
\hdashline
. & . & . & . & 1 & . & . & . & . & . & . & . & . & . & . & . \\
. & a_1^n & . & . & a_1^n & a_0^n & a_1^n & . & . & a_1^n & . & . & . & . & . & . \\
. & . & a_1^n & . & . & a_1^n & a_0^n & a_1^n & . & . & a_1^n & . & . & . & . & . \\
. & . & . & . & . & . & . & 1 & . & . & . & . & . & . & . & . \\
\hdashline
. & . & . & . & . & . & . & . & 1 & . & . & . & . & . & . & . \\
. & . & . & . & . & a_1^n & . & . & a_1^n & a_0^n & a_1^n & . & . & a_1^n & . & . \\
. & . & . & . & . & . & a_1^n & . & . & a_1^n & a_0^n & a_1^n & . & . & a_1^n & . \\
. & . & . & . & . & . & . & . & . & . & . & 1 & . & . & . & . \\
\hdashline
. & . & . & . & . & . & . & . & . & . & . & . & 1 & . & . & . \\
. & . & . & . & . & . & . & . & . & . & . & . & . & 1 & . & . \\
. & . & . & . & . & . & . & . & . & . & . & . & . & . & 1 & . \\
. & . & . & . & . & . & . & . & . & . & . & . & . & . & . & 1 \\
\end{array}
\right)
\left(
\begin{array}{c}
T_{1,1}^n \\
T_{2,1}^n \\
T_{3,1}^n \\
T_{4,1}^n \\
T_{1,2}^n \\
T_{2,2}^n \\
T_{3,2}^n \\
T_{4,2}^n \\
T_{1,3}^n \\
T_{2,3}^n \\
T_{3,3}^n \\
T_{4,3}^n \\
T_{1,4}^n \\
T_{2,4}^n \\
T_{3,4}^n \\
T_{4,4}^n \\
\end{array}
\right)
$$

Figure 3 Structure of the matrices on the right side of Eq.(6) for the example of a 4×4 Cartesian grid and using the Dirichlet boundary conditions of Section II.A.2. Zero elements are represented by dots for clarity.

Initial conditions are provided in the temperature vector $T_{i,j}^0$ for all grid locations (i, j) at $t = 0$. This initial temperature distribution can be arbitrary. However it is important to note that the temperature of the perimeter cells of the N x N Cartesian grid will be held constant at their respective $T_{i,j}^0$ value by the boundary conditions defined above.

3.   Choice of Time Step

The numerical stability of the CN method does not depend on the size of the time step Δt [21]. However, there is an upper limit for Δt. Note in Eq.(8) that the diagonal elements should be sufficiently close to 1. Rather than choosing Δt, it is preferable to fix μ and calculate Δt from Eq.(5), that is,

$$\Delta t = \frac{\mu \rho C_p (\Delta d)^2}{\kappa}. \tag{9}$$

With proper choice of μ, this approach guarantees numerical stability and the maximum possible Δt for the given system. The range of $\mu = 0.1...0.2$ has proven to be a practical choice.

B.   2D Heat Equation with Laser-Induced Heating or Cooling

In order to calculate $[T^{n+1}]$ in Eq.(7), we must first obtain the rate of internal heat generation, *P*. Assume a two-level system that is optically pumped and that can decay radiatively and non-radiatively. The fraction, ε, of the laser excitation energy is converted to heat (non-radiative relaxation) while the fraction, $1-\varepsilon$, undergoes radiative

relaxation as either stimulated or spontaneous emission. Note that stimulated emission is, by definition, resonant with the laser and does not generate any heat. The rate of internal heat generation, $P(x, y, t)$, is therefore proportional to the spontaneous emission rate according to

$$P(x, y, t) = n_2(t) A N_a V \varepsilon \frac{hc}{\lambda_p}, \tag{10}$$

where $n_2(t)$ is the upper level population, A is the spontaneous decay rate, and N_a is the number density of absorbers. In the Crank-Nicolson scheme, the excited volume V in Eq.(10) corresponds to the volume of one cell, $V = 2z_R(\Delta d)^2$, where $2z_R = 2\pi w_0^2 / \lambda_p$ is the confocal parameter for a Gaussian beam.

Following the analysis of a two-level system allowing for saturation by van Dijk [24], the upper level normalized population is given by

$$n_2(t) = \frac{w_a}{gw_a + A} \left\{ 1 - \exp\left[-(gw_a + A)t \right] \right\}, \tag{11}$$

for continuous constant pumping and the initial condition $n_2(0) = 0$. In Eq.(11) we have made use of the fact that the Einstein coefficients for absorption (B_{12}) and stimulated emission (B_{21}) are related by $B_{21} / B_{12} = g_1 / g_2$ and have introduced $g = 1 + (g_1 / g_2)$, where g_1 and g_2 are the degeneracies of the lower and upper level, respectively. The degeneracy is completely lifted in the low coordination symmetries of the glasses studied here, and we therefore assume $g_1 = g_2$ for our computations. In Eq.(11), the absorption rate constant w_a is given by

$$w_a(\lambda, T) = \frac{\sigma_a(\lambda, T)\lambda_p}{hc} I_P(x, y, t), \tag{12}$$

where $I_P(x, y, t)$ is the laser irradiance (in W m^{-2}) and $\sigma_a(\lambda, T)$ is the absorption cross section (in m^{-2}). Note that in steady state ($t \to \infty$) and for high irradiance ($I_P \to \infty$) we have $w_a \to \infty$ and $n_2 \to 1/2$, i.e. at most half of the absorbers can be excited. This properly accounts for saturation and is consistent with the fact that sustained inversion cannot be achieved in a two-level system under adiabatic conditions [25]. The irradiance at a Crank-Nicolson cell at location (x, y) is given by

$$E(x, y, t) = P_o(t) \frac{\phi(x, y)}{(\Delta d)^2},$$

(13)

where the incident laser power $P_o(t)$ (in Watts) is chosen to be a step function at $t = t_0$. The normalized transverse spatial laser power distribution, $\phi(x, y)$, in Eq.(13) is assumed to be Gaussian, i.e.

$$\phi(x, y) = \frac{2(\Delta d)^2}{\pi w_0^2} \exp\left(-2r^2 / w_0^2\right),$$

(14)

where $r^2 = x^2 + y^2$. Equation (14) places the center of the Gaussian beam at the origin. To ensure energy conservation, the physical size of the Crank-Nicolson grid has to be chosen such that it substantially contains the Gaussian beam profile, i.e.

$$\int_0^{N\Delta d/2} \phi(r) dr \approx 1.$$

(15)

C.   Model of Differential Luminescence Thermometry in Solid-State Optical Refrigerators

By far, the most widely studied solid-state optical refrigerator system is Yb^{3+}-doped into the fluorozirconate glass ZBLAN [1]. The schematic in Figure 4 illustrates the concept of solid-state laser cooling using Yb^{3+}. A pump laser is tuned to a wavelength (λ_p) that is longer than the mean luminescence wavelength ($\bar{\lambda}_f$), and the energy difference corresponds to the amount of heat that is extracted as heat from the solid for each excitation/emission cycle. The respective laser-cooling efficiency of this ideal case is given by $\eta_{cool} = (\lambda_p - \bar{\lambda}_f)/\bar{\lambda}_f$. Note that the thermal population of the crystal field levels in the excited state is temperature dependent, causing $\bar{\lambda}_f$ to red-shift and η_{cool} to decrease as temperature decreases.
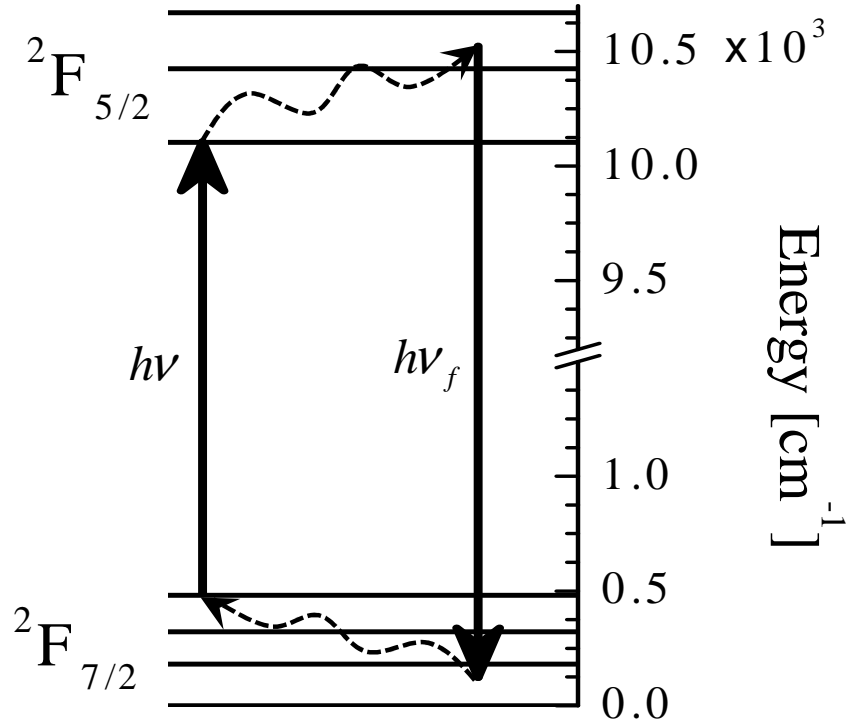
Figure 4 Schematic of energy levels in Yb^{3+}-doped ZBLAN showing the ideal case of laser cooling occurring between the two multiplets of Yb^{3+}. The dopant is excited by the pump laser from the top of the ground state multiplet ($^2F_{7/2}$) to the bottom of the excited state multiplet ($^2F_{5/2}$). Vibrational energy is absorbed from the host during thermalization in both multiplets and, as a result, the material cools.

In a real system, the excited state may have a net quantum efficiency, $\eta(T, \lambda_p)$, that is less than unity because of non-radiative processes occurring as a result of interactions with impurities as well as background absorption due to direct absorption of pump energy by the impurities. Note that η is a function of both temperature and pump wavelength primarily due to its dependence on the resonant absorption, but also due to the spectral overlap between the rare-earth ion emission and the impurity absorption [27]. Incorporating these effects, the cooling efficiency thus becomes

$$\eta_{cool}(T) = \frac{\eta(T, \lambda_p)\lambda_p - \overline{\lambda}_f(T)}{\overline{\lambda}_f(T)}. \tag{16}$$

As the temperature is lowered, $\bar{\lambda}_f$ red-shifts, η_{cool} decreases, and there is a temperature at which laser-induced heating and laser-induced cooling are exactly balanced, i.e. $\eta_{cool} = 0$. This temperature is referred to as the *zero-crossing temperature* (T_{ZCT}), and it can be used as a relative measure of the concentration of impurities and the overall quality of a laser cooling material. The net quantum efficiency at T_{ZCT} can thus be calculated from $\eta(T_{ZCT}, \lambda_p) = \bar{\lambda}_f(T_{ZCT})/\lambda_p$. At temperatures above T_{ZCT}, $\eta_{cool} > 0$ and heat is extracted from the solid, while below T_{ZCT}, $\eta_{cool} < 0$ and there is net heating of the solid. The corresponding laser-induced rate of cooling or heating is given by Eq.(10). The factor ε in Eq.(10) corresponds to the negative cooling efficiency (i.e. heat generation) of Eq.(16). Thus, in the context of optical refrigeration of solids, laser-induced internal cooling is simply considered as negative heating, $\varepsilon = -\eta_{cool}$.

Laser-induced temperature changes inside a solid can be measured by observing the subtle changes that occur in the material's luminescence spectrum as the laser is turned on. This technique is known as differential luminescence thermometry (DLT); specifically, we have developed two-band differential luminescence thermometry (TBDLT) as a sensitive, non-contact method to characterize laser-induced temperature changes in solids [20]. TBDLT infers changes in the local sample temperature from changes in the luminescence spectrum that occur during the laser-induced cooling process, and it provides a temporally and spatially resolved temperature measurement that allows for rapid performance screening of laser-cooling samples. Here, a brief description of TBDLT is presented, and it will be used in Section III to validate the model developed in Sections II.A. and II.B.

The luminescence spectrum of Yb^{3+} in ZBLAN glass is at a wavelength near 1 μm. As shown in **Figure 6**, it consists of two wavelength regions for which the luminescence intensity increases (A, C) and two wavelength regions for which the luminescence intensity decreases (B, D) as the temperature is raised. Regions A and D are spectrally fairly broad and can be easily selected by commercial bandpass interference filters. The TBDLT method chooses these two bands, A and D, and detects changes in their relative intensity to obtain a measure of the associated internal temperature change. At a given location (x, y) with temperature $T_{x,y}$, the TBDLT signal is defined as

$$\xi(T_{x,y},t) = \frac{I_A^*(T_{x,y},t) - I_D^*(T_{x,y},t)}{I_A^*(T_{x,y},t) + I_D^*(T_{x,y},t)}. \tag{17}$$

The luminescence intensities $I_A^*(T_{x,y},t)$ and $I_D^*(T_{x,y},t)$ in Eq.(17) are integrated over the product of the luminescence spectrum $I(\lambda,T)$ and the bandpass filter transmission spectrum $\theta(\lambda)$, i.e.,

$$\begin{aligned}
I_A^*(T_{x,y}) &= \int I(\lambda, T_{x,y}) \theta_A(\lambda) d\lambda \\
I_D^*(T_{x,y}) &= \int I(\lambda, T_{x,y}) \theta_D(\lambda) d\lambda.
\end{aligned} \tag{18}$$
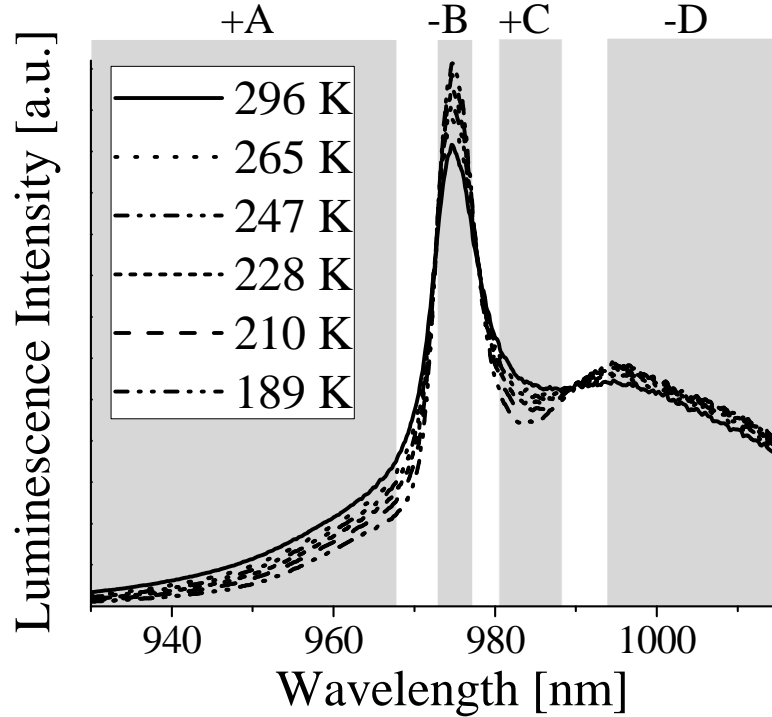
Figure 5 $^2F_{5/2} \rightarrow ^2F_{7/2}$ luminescence spectra of Yb^{3+} in ZBLAN glass at various temperatures. The gray areas indicate wavelength regions in which the luminescence intensity increases (A and C) and regions where the luminescence intensity decreases (B and D) as the temperature is raised. Portions of regions A and D can be selected with commercially available interference filters.

The experimental implementation of the TBDLT method uses a gain-balanced amplified pair of photo-detectors for the simultaneous measurement of $I_A^*(T)$, $I_D^*(T)$ and $I_A^*(T) - I_D^*(T)$, and it requires that the optical powers reaching the two detectors are balanced [20]. In practice this is achieved by simply detuning the optical alignment of the band with the larger signal to match the signal of the other band. Here, let us introduce a factor ζ by which we can scale $I_D^*(T)$ such that it matches $I_A^*(T)$ at the bath temperature T_0, i.e.

$$\zeta = \frac{\int I(\lambda, T_0) \theta_A(\lambda) d\lambda}{\int I(\lambda, T_0) \theta_D(\lambda) d\lambda}. \tag{19}$$

Finally, since luminescence is collected from the entire pumped volume, we must account for the temperature distribution in the pumped volume not being uniform. The measured TBDLT signal, $\Xi(T,t)$, is therefore obtained by integration of $\xi(T_{x,y},t)$ [Eq.(17)] over the transversal plane. Note that the luminescence intensity is proportional to the excited state population $n_2(x,y,t)$ [Eq.(11)], and $\xi(T_{x,y},t)$ is thus weighted by $n_2(x,y,t)$ according to

$$\Xi(T,t) = \iint n_2(x,y,t) \xi(T_{x,y},t) \, dx \, dy, \tag{20}$$

where T becomes the average temperature in the optically excited volume. With these definitions, we obtain $\Xi(T < T_0) < 0$, $\Xi(T = T_0) = 0$, and $\Xi(T > T_0) > 0$. That is, the TBDLT signal will become positive/negative upon laser-induced heating/cooling of a system that was initially thermalized at T_0.

III.   Results and Discussion

In the following, the model developed in Section II is applied to optical refrigeration in Yb[3+]-doped ZBLAN glass as both an example and a quantitative validation. In Section III.A we will first present the relevant material parameters of Yb[3+]-doped ZBLAN glass that are required for the calculation of laser-induced temperature changes (Section III.B) using the model developed in Section II. Section III.B presents a calculation of the laser-induced temperature distribution in ZBLAN:Yb[3+] as a function of time, and Section III.C shows the transient response of the respective two-band

differential luminescence thermometry (TBDLT). Finally, a discussion of sample size effects is given in Section III.D.

Two Yb^{3+}-doped fluorozirconate glass samples were used for the measurements in this study. Sample I was a ZBLANI:1%Yb^{3+} (ZrF_4-BaF_2-LaF_3-AlF_3-NaF-InF_3-YbF_3) glass fabricated in our laboratory from purified precursor materials. Sample II was a ZBLAN:2%Yb^{3+} glass obtained from IPG Photonics and known to be a good laser cooler. The samples were mounted in a liquid-nitrogen flow cryostat in close thermal contact with the cold finger. The sample temperature was measured with a miniature temperature sensor mounted directly on the sample surface. Optical excitation was achieved by a single-pass geometry with focusing the laser into the center of the sample.

A.   *Spectroscopic and material properties of ZBLAN:Yb^{3+} for thermal diffusion modeling*

Several spectroscopic parameters of ZBLAN:Yb^{3+} are needed for the thermal diffusion calculations. The temperature-dependent absorption cross section at the pump wavelength (Eq.(12)) and was obtained by fitting a cubic polynomial to measurements of the absorption cross section at $\lambda_p = 1020.6$ nm at different temperatures (see Figure 6 (a)). Likewise, the temperature dependencies of the mean luminescence wavelength $\bar{\lambda}_f$ (in Eq.(16)) as well as the luminescence intensity integrals $\int I(\lambda,T)\theta_A(\lambda)d\lambda$ and $\int I(\lambda,T)\theta_D(\lambda)d\lambda$ (Eq.(18)) were obtained by fitting cubic polynomials to respective experimental data obtained at different temperatures (see Figure 6 (b) and 6 (c)). Table 1 summarizes the respective polynomial coefficients. Table 2 summarizes material

properties typical of ZBLAN glass as well as laser and computational parameters specific

to the present experiments.
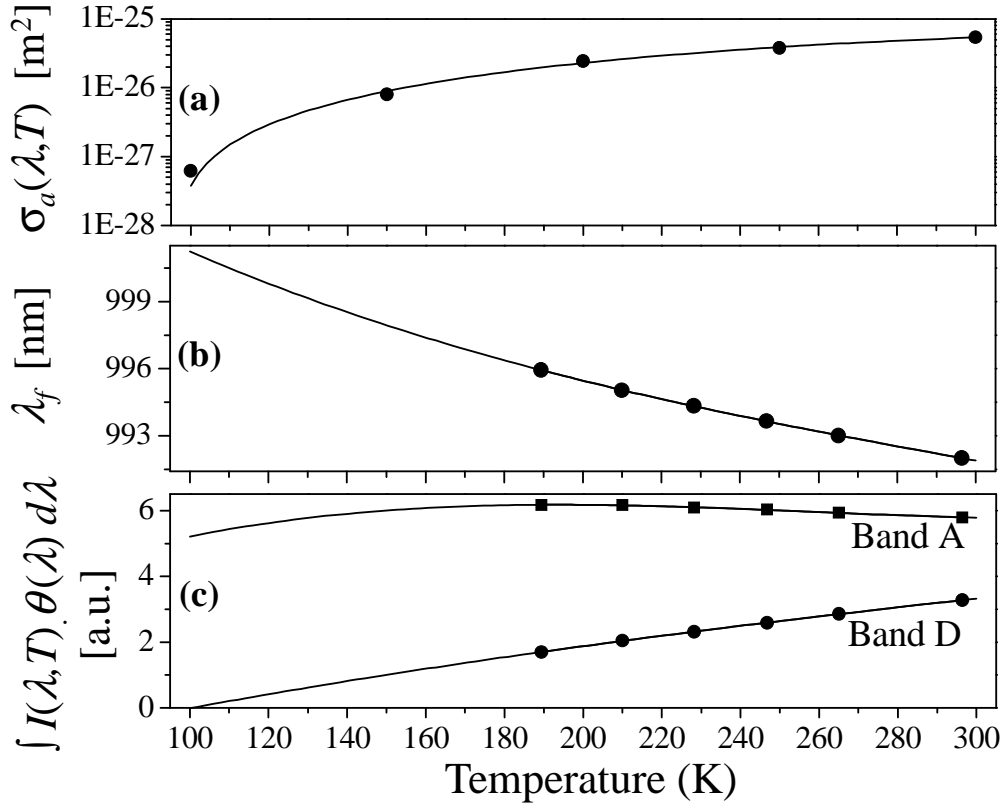
Figure 6 Temperature dependence of spectroscopic parameters of ZBLAN:Yb^{3+} : (a) Absorption cross section, $\sigma_a(\lambda, T)$, at λ_p = 1020.6 nm [26]; (b) Mean luminescence wavelength, $\bar{\lambda}_f$, derived from luminescence spectra at different temperatures; (c) Spectral overlap integrals $\int I(\lambda,T)\theta_A(\lambda)d\lambda$ (circles) and $\int I(\lambda,T)\theta_D(\lambda)d\lambda$ (squares) (see Eq.(18)). The solid lines in each of the plots are least-squares fits to a cubic polynomial, and the respective parameters are summarized in Table 1.

Table 1 Coefficients obtained from least-squares fits of the function $y(T) = a_0 + a_1T + a_2T^2 + a_3T^3$ to the experimental data shown in Figure 6.

Coefficient	Absorption Cross Section, σ_a [m^2]	Mean Luminescence Wavelength, $\bar{\lambda}_f$ [nm]	Band A [a.u.]	Band D [a.u.]
a_0	1.29E-26	1011.33	-2.58	0.669
a_1	-3.90E-28	-0.130	0.030	0.071
a_2	3.09E-30	3.21E-4	-4.64E-5	-2.91E-4
a_3	-4.46E-33	-3.52E-7	4.09E-8	3.73E-7

Table 2 Summary of key parameters characterizing the ZBLAN:Yb^{3+} glass, the laser excitation, and the Crank-Nicolson computation.

Parameter	Symbol	Value	Units	Ref.
Material Parameters				
Thermal Conductivity	κ	0.77	W m^{-1} K^{-1}	[26]
Density	ρ	4445	kg m^{-3}	[26]
Specific Heat	C_v	670	J kg^{-1} K^{-1}	[26]
Specific Heat Capacity	$C_p = C_v \rho$	2.9782 x 10^6	J m^{-3} K^{-1}	
Yb^{3+} Ion Density (1 mol%)	N_a	1.899 x 10^{26}	m^{-3}	[27]
Radiative relaxation rate	w_r	540	s^{-1}	[27]
Internal Net Quantum Efficiency	η	Varied		
Laser Parameters				
Laser Power	Ψ_0	3.75	W	
Laser Wavelength	λ_p	1020.6	nm	
Beam Waist	w_0	10	μm	
Laser ON time	t_0	0	s	
Crank-Nicolson Parameters				
Square lattice constant	Δd	50	μm	
Square Grid Elements	$N \times N$	71 x 71		
CFL number	M	0.2		

B. *Laser-Induced Temperature Changes in ZBLAN:Yb^{3+}*

The thermal response (Eq.(7)) and the resulting luminescence response (Eq.(20)) of a solid under Gaussian beam irradiation can now be calculated. As an example, **Figure 7** shows four calculations of the time-dependent transversal temperature distribution (at $T_0 = 300$ K) for four hypothetical samples of ZBLAN:Yb^{3+} having different net quantum efficiencies ($\eta = 1$, 0.98, 0.97, and 0.94). Continuous wave (CW) laser excitation with a Gaussian beam profile begins as a step function at $t = 0$ in these calculations. The lower part of **Figure 7** shows the corresponding change in temperature at the center of the Gaussian beam over the course of 5 seconds. The top row in **Figure 7** represents the case of an ideal ZBLAN:Yb^{3+} sample that has $\eta = 1$ and exhibits laser-induced cooling. For this case, the center of the pumped area cools from 300 K to 299.587 K during the first 20 ms and reaches a steady-state temperature of 299.18 K (at $t = 5$ s). Samples with lower net quantum efficiency show less laser-induced cooling or even laser-induced heating, as illustrated for the $\eta = 0.94$ case (**Figure 7**, bottom row). Note that internal heat generation is essentially zero at $\eta = 0.97$. This is expected from Eq.(16): η_{cool} is zero for $\eta = \bar{\lambda}_f / \lambda_p = 0.9718$, i.e. 300 K is the T_{ZCT} for ZBLAN:Yb^{3+} with $\eta = 0.9718$ pumped at 1020.6 nm. Net laser-induced heating thus occurs for $\eta < 0.97$.
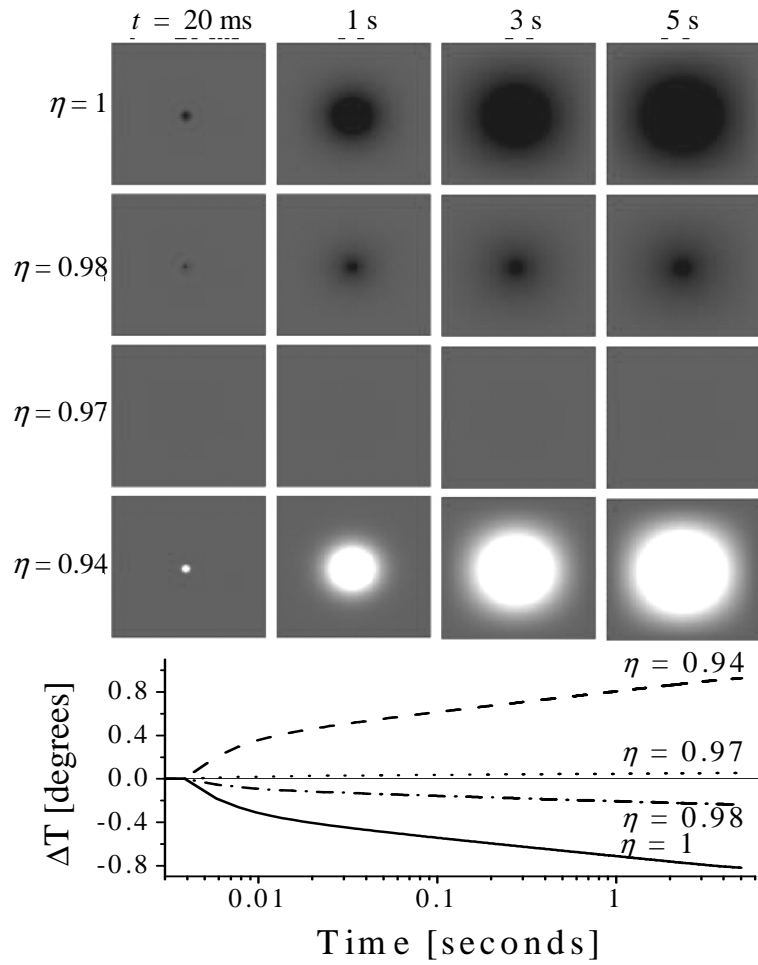
Figure 7 Spatial (top) and temporal (bottom) representation of calculated laser-induced heat diffusion in ZBLAN:1%Yb^{3+} glass pumped at 1020.6 nm. The calculation was performed using the two-dimensional CN method in a 3.55 × 3.55 mm grid (see Section II) and the parameters of Tables 1 and 2. The internal net quantum efficiency η is reduced from top to bottom in the figure. The gray scale covers the range of 299.0 K (black) to 300.1 K (white) with the bath temperature held at T_0=300 K.

C.   Transient   Response   of   ZBLAN:Yb^{3+} Luminescence

The TBDLT transients measured for Samples I and II at various bath temperatures are shown in Figure 8. Laser-induced cooling is evident by a decrease in the TBDLT

signal, $\Xi(T,t)$. The dependence of the TBDLT signal as a function of time is linear in the double-logarithmic representation of Figure 8, indicating that it follows a simple power law according to

$$\Xi(t) \propto t^{\vartheta}. \tag{21}$$

The slope, ϑ, of the line in double-logarithmic representation is a metric for the laser-induced temperature change, and it can be used as a figure of merit for the laser-cooling performance of the material at a given bath temperature. Laser-induced cooling or heating is therefore present if $\vartheta < 0$ or $\vartheta > 0$, respectively. Figure 9 presents the ϑ values obtained from fits of Eq.(21) to the experimental data (Figure 8), and T_{ZCT} was estimated to be 158 K and 238 K for Sample II (filled squares) and Sample I (filled circles), respectively. At these temperatures, the mean luminescence wavelength is found to be 995.9 nm and 993.96 nm, respectively (see Figure 6 (b) and Table 2). With a fixed laser excitation wavelength of 1020.6 nm, the net quantum efficiency η at T_{ZCT} is thus calculated to be 0.9758 (Sample II) and 0.9739 (Sample I) [Eq.(16)]. Figure 9 also shows ϑ values calculated from the model presented in Section II [Eq.(20)]. The calculations assumed the above net quantum efficiencies, and a scale factor was applied to the experimental data to match the absolute value of ϑ at 300.25 K (Sample I) and 257.05 K (Sample II). The model provides a good quantitative description of the experimental data and thus serves as a useful tool to predict the laser cooling performance of other materials.
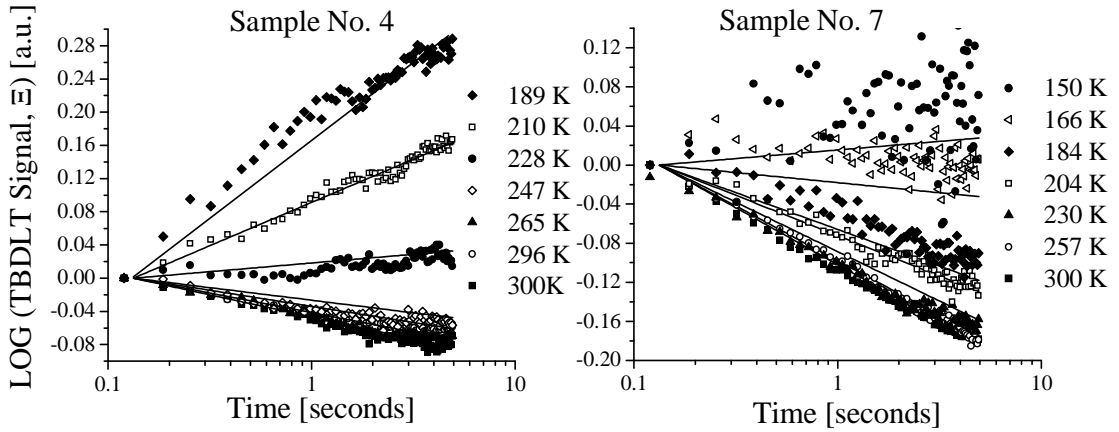
Figure 8 Experimental TBDLT transients of ZBLAN:Yb^{3+} Samples I and II (see Section III.A) recorded at different bath temperatures, T_0. The solid lines are fits to Eq.(21), and the respective ϑ-values are shown in Figure 9.

An interesting feature is observed at low temperatures for Sample II. ϑ and thus laser-induced heating reaches a maximum at 133 K. This maximum is the result of two counteracting effects. On the one hand, the laser cooling efficiency gradually decreases with decreasing temperature [Eq.(16)] causing more of the absorbed power to be converted to heat [Eq.(10)]. On the other hand, the absorption coefficient at the pump wavelength decreases rapidly with decreasing temperature (Figure 6 (a)). Therefore, $T \rightarrow 0$ causes $\sigma_a \rightarrow 0$ causing the rate of internal heat generation $P \rightarrow 0$ and thus $\vartheta \rightarrow 0$, a trend that is confirmed by the experimental data.
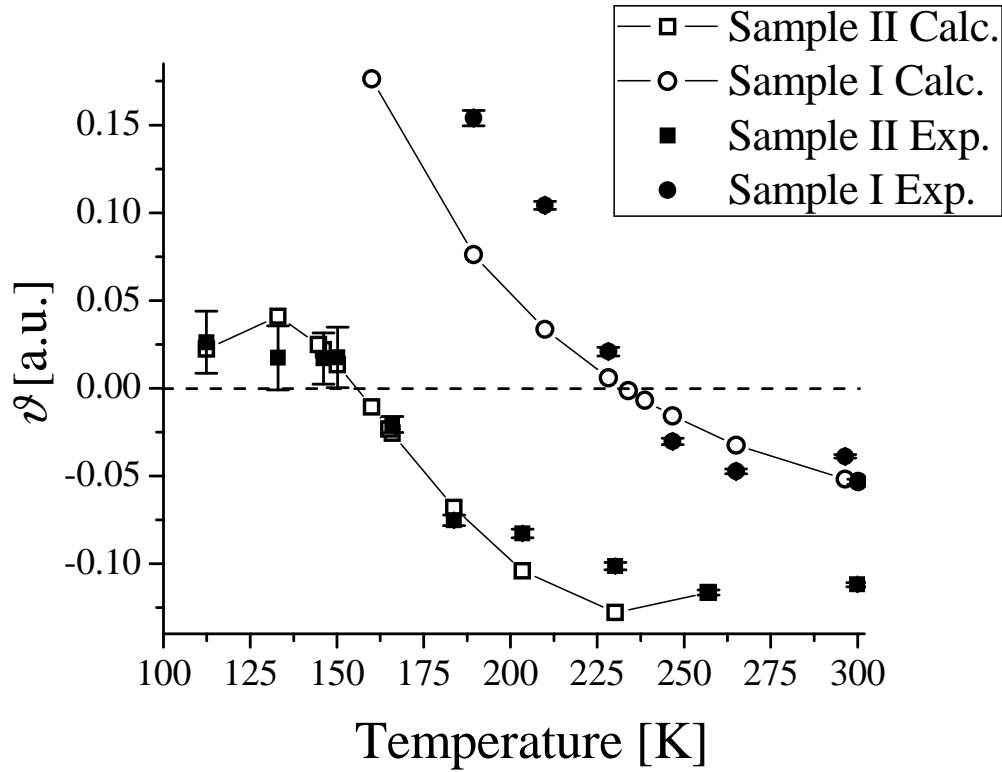
Figure 9 TBDLT parameter ϑ (Eq.(21)) for experimental data (filled symbols) and calculated data (open symbols) for Samples I and II (see Section III). The T_{ZCT} is found to be 238 K and 158 K for Sample I and II, respectively.

D.   Sample size and associated characteristic time constants

The model also allows the study of the dependence of the transient response on the size of the sample. This is illustrated in Figure 8, which shows calculated TBDLT transients over the course of 60 seconds for ZBLAN:Yb^{3+} with η = 0.9739 and various two-dimensional sample sizes. Three regimes are found. There is an initial fast component that is independent of sample size and that has a time constant governed by the excited state lifetime of the rare-earth ion. The respective time constant is

characteristic of how quickly heat is removed from (cooling) or deposited into (heating) the sample in the small excitation volume defined by the focused laser. This time constant is on the order of only a few milliseconds in ZBLAN:Yb^{3+} and was not resolved in the measurements shown in Figure 8. The initial fast component is followed by a slower component the duration of which depends on the sample size. The time constant of this component is governed by the heat capacity and thermal conductivity of the material and extends for several seconds for ZBLAN:Yb^{3+} samples with cross-sectional areas of >5 mm^2. This is the time regime in which the measurements of this study were carried out (Figure 8) and from which the TBDLT parameter ϑ was calculated (Figure 9). Finally, the thermal processes induced by a CW laser, combined with the sample surface being held at the constant bath temperature T_0, produces a steady-state temperature distribution (and thus a constant TBDLT signal) after some longer time. The time period for this steady state to develop in larger ZBLAN samples is on the order of many seconds and is determined by the total amount of heat being deposited into the sample (i.e. sample size) and the thermal properties (thermal conductivity and heat capacity). Note that the initial fast temporal response of the 0.55 x 0.55 mm^2 grid shown in Figure 10 is typical of what would be expected for a sample with small cross-sectional area such as a bare optical fiber. In the case of bulk ZBLAN:Yb^{3+}, the measured TBDLT transients during the first few seconds are well described by assuming a sample size larger than 3 x 3 mm^2 (see Figure 10), which is consistent with the transversal dimension of the actual samples used in our experiments.
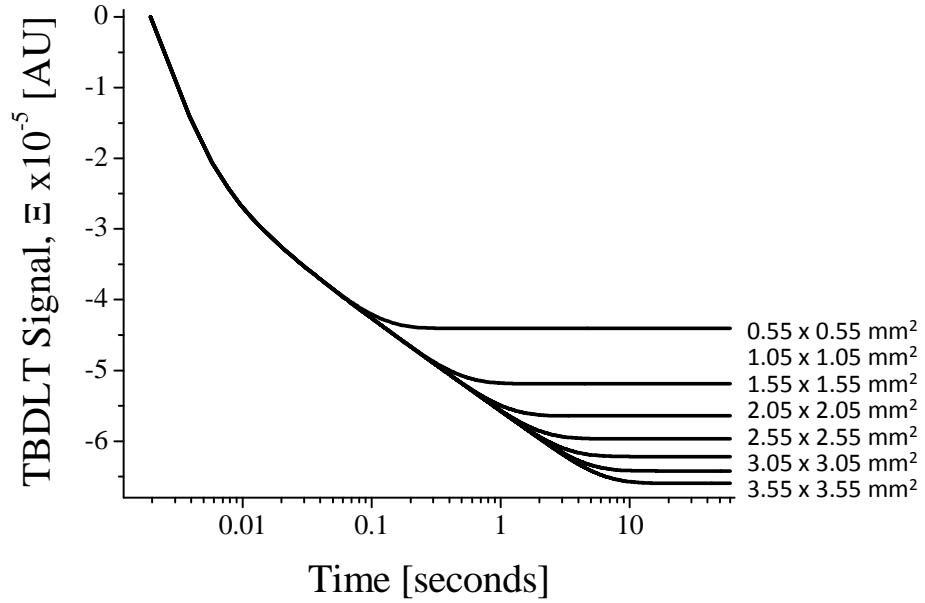
Figure 10   TBDLT transients for ZBLAN:Yb^{3+} calculated from Eq.(20) with $\eta =$ 0.9739 and   varying the sample size. The spatial resolution was held constant (50 x 50 μm^2 grid element size), and the sample size was varied via the grid dimension, N. Material parameter values from Tables 1 and 2 were used.

IV. Conclusions

We have presented a quantitative model that (1) describes the time-dependent laser-induced temperature distribution in a solid and (2) correlates the laser-induced temperature changes with changes in luminescence properties. The implicit Crank-Nicolson scheme used for the computational evaluation of the heat equation was found to be numerically stable and efficient, allowing for the rapid exploration of the parameter space. As an example, the model was validated for two-band differential luminescence thermometry (TBDLT) in ZBLAN:Yb^{3+} optical refrigerator samples. The laser-cooling performance as a function of temperature was accurately predicted by the model, allowing the T_{ZCT} and net quantum efficiency to be calculated. Furthermore, the model

revealed the presence of three distinct time constants that govern the luminescence response in optical refrigerators upon laser excitation. The tools developed in this study are general and can be readily applied to other materials and temperature-dependent properties, enabling quantitative studies of light-matter interactions in a wide range of materials and devices.

Acknowledgements:

References

[1] R. I. Epstein and M. Sheik-Bahae, eds., in *Optical Refrigeration. Science and Applications of Laser Cooling of Solids*, (Wiley, Weinheim, 2009).

[2] W. Koechner, *Solid-State Laser Engineering*, (Springer-Verlag, Berlin 1992).

[3] S. Tanimizu, "Principal phosphor materials and their optical properties," in *Fundamentals of phosphors*, W. M. Yen, S. Shionoya, H. Yamamoto, eds., (CRC Press, Boca Raton, FL, 2007), Chapter 2.

[4] E.F. Schubert, *Light-Emitting Diodes*, (Cambridge University Press, Cambridge, 2007).

[5] A. Christensen, S. Graham, "Thermal effects in packaging high power light emitting diode arrays," Applied Thermal Engineering **29** [2-3], 364-371 (2009).

[6] F. Hwu, G. Sheu, and J. Chen, "Thermal modeling and performance of LED packaging for illuminating device," Proc. SPIE 6337, 63371J (2006).

[7] K. Sokolov, M. Follen, J. Aaron, I. Pavlova, A. Malpica, R. Lotan and R. Richards-Kortum, "Real-time vital optical imaging of precancer using anti-epidermal growth factor receptor antibodies conjugated to gold nanoparticles," Cancer Res. **63**, 1999–2004 (2003).

[8] I. El-Sayed, X. Huang and M. El-Sayed, "Surface Plasmon resonance scattering and absorption of anti-EGFR antibody conjugated gold nanoparticles in cancer diagnostics: applications in oral cancer," Nano Lett. **5**, 829–34 (2005).

[9] O. Ekici, R. K. Harrison, N. J. Durr, D. S. Eversole, M. Lee1 and A. Ben-Yakar, "Thermal analysis of gold nanorods heated with femtosecond laser pulses," J. Phys. D: Appl. Phys. **41**, 185501 (2008).

[10] D. Rosenthal, "Mathematical theory of heat distribution during welding and cutting," Welding Journal, Res. Suppl. **20** [5], 220–234 (1941).
M. J. C. van Gemert, "Modelling of light and heat diffusion in biological tissue," in *Laser-induced interstitial thermotherapy*, G. J. Muller and A. Roggan eds., (SPIE, Bellingham, Washington, 1995), Part III.

[11] Yu. Scherbakov, A. Yakunin, I. Yaroslavsky, V. Tuchin, "Thermal processes modeling during uncoagulating laser radiation interaction with multi-layer biotissue. 2. Numerical results," Opt. Spectroscopy **76** [5], 759–765 (1994).

[12] T. Dai1, B. M. Pikkula1, L. V. Wang and B. Anvari, "Comparison of human skin opto-thermal response to near-infrared and visible laser irradiations: a theoretical investigation." Phys. Med. Biol. **49**, 4861–4877 (2004).

[13]   K. M. McNally, A. E. Parker, D. L. Heintzelman, B. S. Sorg, J. M. Dawes, T. J. Pfefer, and A. J. Welch, "Dynamic Optical-Thermal Modeling of Laser Tissue Soldering with a Scanning Source," IEEE J. Selected Topics in Quant. Elect. **5** [4], (1999).

[14]   S. T. Flock, M. S. Paterson, B. C. Wilson, D. R. Wyman, "Monte carlo modeling of light propagation in highly scattering tissues 1: model predictions and comparison with diffusion theory," IEEE Transaction on Biomedical Eng. **36** [12], 1162 (1989).

[15]   A. J. Welch and R. Richards-Kortum, "Monte Carlo simulation of the propagation of fluorescent light," in *Laser-induced interstitial thermotherapy*, G. J. Muller and A. Roggan eds., (SPIE, Bellingham, Washington, 1995), pp. 174-189.

[16]   S. M. George, "Laser-induced thermal desorption," in *Physical methods of chemistry*, Vol. 9, Part 1, B. W. Rossiter and R. C. Baetzold eds., (Wiley, NY 1993), Chapter 7.

[17]   J. Colinge , "Computer modeling of coupled electrodynamical and thermal processes of laser-radiation interaction with matter for 2-dimensional geometry," in *Physics of Semiconductor Devices*, J. Colinge and C. A. Colinge, eds., (Kluwer Academic Publishers, NY, 1998).

[18]   A. J. Reich, C. Tham, S. Smith, "Computational modeling of laser induced heating," ASME Publications – PVP **491** [1], 65-72 (2004).

[19]   D. V. Seletskiy, S. D. Melgaard, S. Bigotta, A. Di Lieto, M. Tonelli, R. I. Epstein, and M. Sheik-Bahae, "Demonstration of an Optical Cryocooler," in *Conference on Lasers and Electro-Optics/International Quantum Electronics Conference*, OSA Technical Digest (CD) (Optical Society of America, 2009), paper IPDA9.

[20]   W. M. Patterson, M. P. Hehlen, , R. I. Epstein, M. Sheik-Bahae, "Synthesis and evaluation of ultra-pure rare-earth-doped glass for laser refrigeration," Proc. SPIE 7228, 69070A (2008).

[21]   J. Crank, P. Nicolson, "A practical method for numerical evaluation of solutions of partial differential equations of the heat conduction type," Proc. Camb. Phil. Soc. **43**, 50 (1947).

[22]   R. Courant, K. Friedrichs, and H. Lewy, "On the partial difference equations of mathematical physics," IBM Journal March, 215-234 (1967).

[23]   F. Pelle, and F. Auzel, "Saturation effect on multiphonon relaxation rates of rare earth ions in glasses at high excitation power," J. Alloys and Compounds **131,** 300-301 (2000).

[24]   C. A. Van Dijk, N. Omenetto and J. D. Winefordner, "Extended model for saturation in a two-level system," Appl. Spectroscopy **35**, 389 (1981).

[25]   V. N. Lugovoi, V. N. Strel'stov, "Possibility of population inversion in a two-level system by a wide-band pump field," Sov. J. Quant. Electron **6**, 562 (1976).

[26]   S. M. Lima, T. Catunda, R. Lebullenger, A. C. Hernandes, M. L. Baesso, A. C. Bento and L. C. M. Miranda, "Temperature dependence of thermo-optical properties of fluoride glasses determined by thermal lens spectrometry," Phys. Rev. B. **60** , 15173 (1999).

[27]   M. P. Hehlen, R. I. Epstein, and H. Inoue, "Model of laser cooling in the Yb^{3+}-doped fluorozirconate glass ZBLAN," Phys. Rev. B **75** [14], 144302 (2007).

Chapter 5

Measurement of Solid-State Optical Refrigeration by Two-Band Differential Luminescence Thermometry

W.M. Patterson[*,1], D.V. Seletskiy[1], M. Sheik-Bahae[1], R.I. Epstein[2], M.P. Hehlen[2]

[1]   800 Yale Blvd. NE, Albuquerque, NM 87131

[2]   Los Alamos National Laboratory, Los Alamos, NM 87545, USA

[*]   Corresponding Author: wendy5@unm.edu, 505-277-3301, 505-277-xxxx

Abstract

We present a non-contact optical technique for the measurement of laser-induced temperature changes in solids. Two-band differential luminescence thermometry (TBDLT) achieves a sensitivity of ~7 mK and enables precise measurement of the net quantum efficiency of optical refrigerator materials. TBDLT detects internal temperature changes by decoupling surface and bulk heating effects via time-resolved luminescence spectroscopy. Several Yb^{3+}-doped fluorozirconate (ZBLANI) glasses fabricated from precursors of varying purity and by different processes are analyzed in detail. A net quantum efficiency of 97.39$\pm$0.01% at 238 K (at a pump wavelength of 1020.5 nm) is found for a ZBLANI:1%Yb^{3+} laser-cooling sample produced from metal fluoride precursors that were purified by chelate-assisted solvent extraction and dried in hydrofluoric gas. In comparison, a ZBLANI:1%Yb^{3+} sample produced from commercial-grade metal fluoride precursors showed pronounced laser-induced heating that is indicative of a substantially higher impurity concentration. TBDLT enables rapid and sensitive benchmarking of laser-cooling materials and provides critical feedback to the development and optimization of high-performance optical cryocooler materials.

1. Introduction

The first successful laser-induced cooling of a solid in 1995 produced a mere 0.3 Kelvin of cooling in the Yb^{3+}-doped fluorozirconate glass ZBLAN (ZrF_4-BaF_2-LaF_3-AlF_3-NaF) [1]. Since then, the field has made steady progress in material preparation methods [2],[3], optical configurations [4], and characterization techniques; and this effort has recently resulted in the laser cooling of a $LiYF_4$:Yb^{3+} bulk crystal to 164 K [5]. This temperature rivals high-end thermoelectric coolers [6] and underscores the potential of laser cooling as an emerging solid-state cryogenic refrigeration technology. Laser cooling down to ~70 K is theoretically possible in Yb^{3+}-doped materials [7],[8], and even lower temperatures may be achieved with other rare-earth ions (such as Tm^{3+} or Dy^{3+}) that have smaller energy gaps and respectively higher laser-cooling efficiencies.

The ability to accurately and rapidly measure the laser-cooling efficiency of a sample is critical for the systematic development of the purification and fabrication processes associated with the preparation of optical refrigerator materials. The measurement of the laser-cooling efficiency, however, is met with difficulties. Significant pump light absorption and a corresponding significant temperature change is only achieved in multi-pass pump geometries. These involve not only the setup and alignment of a pump cavity, but also the laborious preparation of a sample with high quality optical surfaces. Furthermore, non-contact thermometry is required since a temperature sensor in thermal contact with the sample would potentially become a heat load when exposed to the pump light and sample luminescence. A simple single-pass pump geometry and a thermometry method that is insensitive to surface preparation would greatly facilitate

sample characterization and enable expeditious feedback of laser-cooling performance data to the process development effort. A non-contact thermometry method is therefore needed that (1) has sufficiently high sensitivity to detect the < 0.1 K temperature changes that are typical of single-pass pumping of laser-cooling materials, (2) is insensitive to laser-induced heating at imperfect sample surfaces, (3) can be used at low temperatures, and (4) can resolve the fast thermal response in the time domain. Luminescence spectra have been used in the past as non-contact internal temperature probes and, in the case of rare-earth doped materials, absolute temperature measurements with ±0.1 ºC accuracy have been reported [9]. The changes in the luminescence intensity distribution for rare-earths are quite subtle, especially when compared to those observed in semiconductors where substantial wavelength shifts produce large changes in the intensity distribution [10]. In contrast, the *4f* electrons in rare-earths are well shielded from the environment in the solid, and crystal field transitions therefore do not appreciably shift with temperature. The temperature-induced intensity changes in rare-earth luminescence spectra are thus primarily due to changes in (1) the Boltzmann population of the crystal field levels of the emitting state and (2) the homogeneous linewidths of the individual crystal-field transitions. Seletskiy et al. reported a time-resolved technique that detects small laser-induced temperature changes inside the sample via changes in its luminescence spectrum [11]. Their differential luminescence thermometry (DLT) experiment correlated the relative intensity change of two adjacent regions in the luminescence spectrum to a temperature change and, using a monochromator in conjunction with a balanced pair of photodiodes, achieved milli-Kelvin sensitivity for a GaAs heterostructure sample.

In this paper we present a two-band differential luminescence thermometry (TBDLT) method that achieves ~7 mK sensitivity in rare-earth-doped materials. By selecting two bands in the luminescence spectrum by interference filters, in combination with large core optical fibers and highly amplified balanced photodetectors, improved optical throughput and significantly higher sensitivity is achieved compared to earlier DLT studies [9]. The TBDLT method offers substantially higher sensitivity than data acquisition with a commercial luminescence spectrometer and is a tool to study laser-induced thermal processes in any doped luminescent solid. In this study, we apply TBDLT to rare-earth doped optical refrigerator materials. We present a detailed analysis of several Yb^{3+}-doped fluorozirconate glasses and show that the measured laser-cooling performance correlates with the fabrication history of the sample, providing valuable information for further optimizing the material preparation processes. The TBDLT technique and data analysis methods are described in Section 2 followed by a description of the experiments in Section 3. Section 4 presents measurements of two $ZBLAN:Yb^{3+}$ laser-cooling samples, and Section 5 summarizes the findings of this study.

2. Two-Band Differential Luminescence Thermometry

A. Principle of Operation

Two-band differential luminescence thermometry (TBDLT) monitors the luminescence from a sample and deduces laser-induced temperature changes from changes in the spectral distribution. Laser-induced temperature changes can arise from (1) local cooling or heating inside the material and (2) heating at imperfect sample

surfaces. The main advantage of TBDLT is in its ability to distinguish the intrinsic laser-induced cooling or heating processes from laser-induced heating at the sample surfaces, thereby eliminating the need for difficult and laborious surface preparation and thus greatly facilitating sample characterization. Bulk cooling or heating is decoupled from surface heating by monitoring laser-induced temperature changes in the time domain and in a small internal volume. This can be achieved because internal cooling or heating processes dominate the temperature change immediately after turning on the laser, and it is only after some time that heat generated at the sample surface reaches the locally monitored excitation volume inside the sample. The experiment, therefore, consists of turning on the laser for a period of time and monitoring the temperature change that occurs due to intrinsic cooling or heating processes, followed by turning off the laser for a period of time for the sample to thermalize back to the ambient temperature. This sequence is repeated, and the signals are averaged over many cycles. This cycled pumping method also eliminates the effects of long-term ambient temperature drifts. Such an experiment is also, importantly, insensitive to re-absorption effects which plague experiments taken with an infrared camera for example.
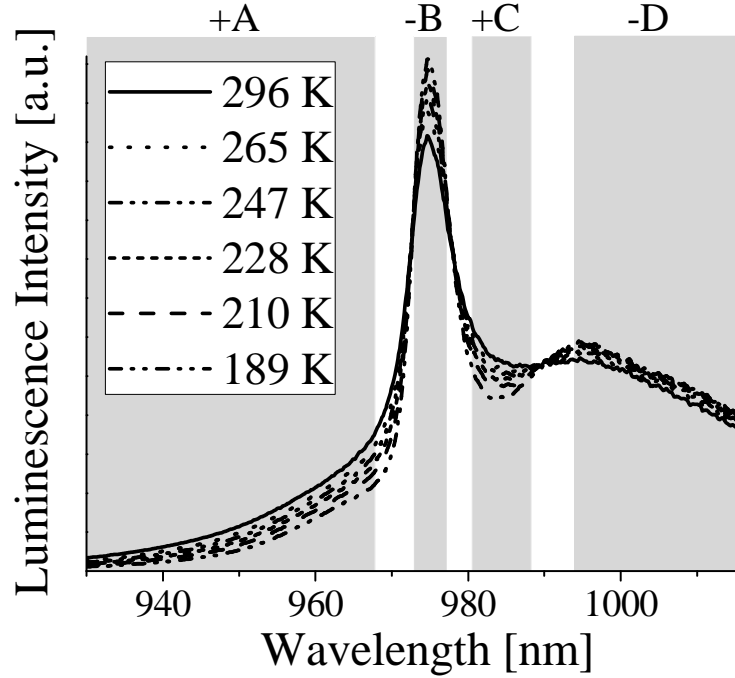
Figure 1 Area normalized luminescence spectra at different temperatures for sample No. 4 (see Table 1). As the temperature is increased, the luminescence intensity of regions A and C increases while the luminescence intensity of regions B and D decreases. Note that the full spectrum, which extends to > 1030 nm, is not shown for clarity.

Let us now look more closely at one such pumping cycle for the example of the Yb^{3+}-doped fluorozirconate glass ZBLANI (ZrF$_4$-BaF$_2$-LaF$_3$-AlF$_3$-NaF-InF$_3$). Assume a bulk sample of ZBLANI:Yb^{3+} in thermal equilibrium with the surrounding bath temperature. A pump laser with a Gaussian transverse intensity distribution is focused into the bulk of the sample and turned on at time $t = 0$. A spatially non-uniform and time-dependent temperature distribution will develop as a result of laser-induced internal heating or cooling processes. As illustrated in Figure 1, the $^2F_{5/2} \rightarrow ^2F_{7/2}$ luminescence spectrum of Yb^{3+} is temperature dependent, and the Yb^{3+} ions can therefore serve as local

temperature probes. Specifically, the ZBLANI:Yb^{3+} luminescence spectrum contains four spectral regions in which the luminescence intensity either increases (regions A and C) or decreases (regions B and D) as the sample temperature is raised (See Figure 1). We will focus on regions A and D since they can be easily selected with commercial bandpass filters (see Section 3.B). The Yb^{3+} luminescence spectral distribution $I(\lambda,T,t)$ at time t is determined by the local temperature T and the respective differential luminescence signal is defined as [12]

$$\Xi(T,t) = \frac{I_A^*(T,t) - I_D^*(T,t)}{I_A^*(T,t) + I_D^*(T,t)}. \tag{1}$$

In Eq.(1), $I_A^*(T,t)$ and $I_D^*(T,t)$ are integrals over the product of the luminescence spectrum, $I(\lambda,T,t)$, and the bandpass filter transmission spectra $\theta_A(\lambda)$ and $\theta_B(\lambda)$, respectively, i.e.

$$\begin{aligned} I_A^*(T,t) &= \int I(\lambda,T,t)\theta_A(\lambda)d\lambda \\ I_D^*(T,t) &= \int I(\lambda,T,t)\theta_D(\lambda)d\lambda, \end{aligned} \tag{2}$$

where Figure 2 shows this overlap for our particular example.
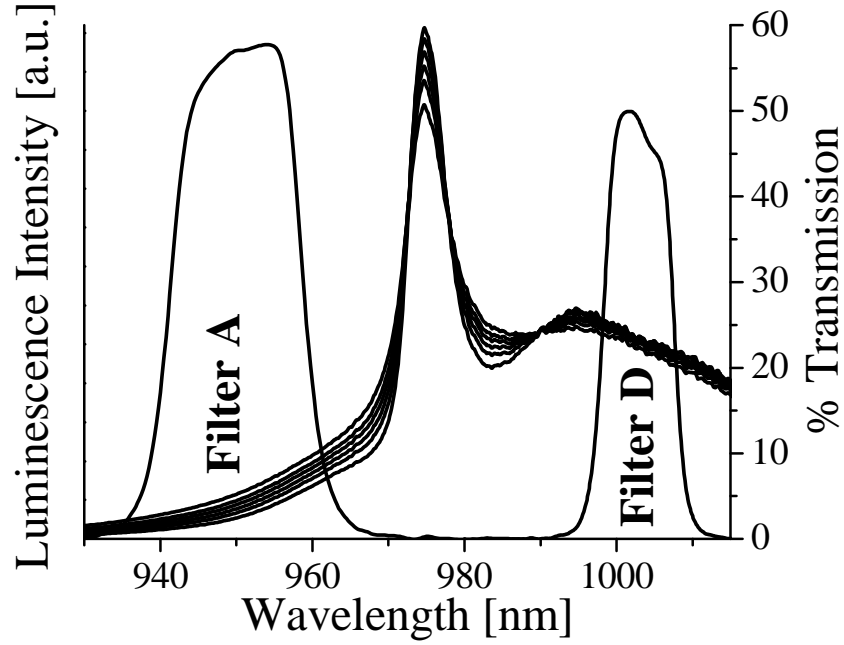
Figure 2 Area normalized luminescence spectra at different temperatures for Sample No. 4 (left axis) and transmission spectra of the commercial band pass filters (right axis) used in the TBDLT experiment. Filters A and D are chosen such as to select and integrate a sizeable portion of the luminescence spectrum regions +A and -D (see Figure 1), respectively.

Finally, since luminescence is collected from a finite volume, we must account for the temperature distribution in the collection volume not being uniform. The measured TBDLT signal, $\Xi(T,t)$ is therefore obtained by integration of Eq. (1) over the transversal plane. Note that the luminescence intensity is proportional to the excited state population $n_2(x,y,t)$, and $\Xi(T,t)$ is thus weighted by $n_2(x,y,t)$ accordingly, as discussed in detail elsewhere [12]. $\Xi(T,t)$ is defined such that it decreases with decreasing sample

temperature, i.e. laser-induced cooling will cause the value of $\Xi(T,t)$ to decrease with time. Normalization to the total luminescence intensity $I_A^* + I_D^*$ accounts for the temperature dependence of the absorption coefficient as well as for drifts in optical alignment and laser power. The change in $\Xi(T,t)$ is thus a direct measure for the laser-induced temperature change in the collection volume. $\Xi(T,t)$ can be found, in principle, from a series of luminescence spectra recorded in rapid succession after the laser has been turned on. The sensitivity of commercial luminescence spectrometers, however, was found to be insufficient and did not allow for sufficiently high data acquisition rates to resolve $\Xi(T,t)$. This provided the main motivation for developing the TBDLT method presented here.

B. Data Analysis Method

The local temperature in the excited volume, and thus the measured TBDLT signal $\Xi(T,t)$, varies as a function of time after turning on the laser. $\Xi(T,t)$ therefore depends on several factors including (1) host material properties such as heat capacity, thermal conductivity and the mass density, (2) pump beam characteristics such as beam waist and laser power, (3) rare-earth dopant ion density and relaxation rate, (4) the net quantum efficiency, η, which is affected by impurity concentrations, and (5) sample size. A formal description of the spatial and temporal dependence of temperature in laser-cooling materials is given elsewhere [12]. From these calculations we expect the TBDLT signal $\Xi(T,t)$ to have three temporal components. There is an initial fast component

with a time constant governed by the excited state lifetime of the rare-earth ion, and it is characteristic of how quickly heat is removed from (cooling) or deposited into (heating) the sample in the small excitation volume defined by the focused laser. A subsequent second slow component has a time constant that is governed by the material properties, and it is characteristic of how quickly heat flows out of (cooling) or into (heating) the much larger bulk volume of the sample. Finally, the sample reaches thermal equilibrium and $\Xi(T,t)$ reaches a steady-state value. The period of time required for the steady state to develop depends on the sample size and was found to be > 5 seconds for the samples of this study. The experimental setup, described in detail in Section 3.B, did not allow for measurement of the initial fast component and therefore only captured the second slow component (beginning at $t \approx 25$ ms in ZBLANI:Yb^{3+}). The functional form of the slow component of the $\Xi(T,t)$ transient follows a simple power law [12]

$$\Xi(T,t) \propto t^{\vartheta}.$$ (3)

The slope, ϑ, of the respective line in double-logarithmic representation is a metric for the laser-induced temperature change, and it can be used as a characteristic TBDLT parameter that provides a measure of the laser-cooling performance of the material at a given bath temperature. Laser-induced cooling or heating is therefore present if $\vartheta < 0$ or $\vartheta > 0$, respectively. $\vartheta = 0$ corresponds to the temperature at which the rates of laser-induced heating and cooling processes are exactly balanced. As shown in the next

section, this heat-balanced point is of particular significance as it can be used to determine the net quantum efficiency of the material.

C. TBDLT of Optical Refrigerator Materials

In rare-earth-doped optical refrigerators, a pump laser is tuned to excite the rare-earth ion at a wavelength λ_p that is longer than the mean luminescence wavelength $(\overline{\lambda}_f)$, and thermal energy is subsequently removed from the solid by anti-Stokes luminescence. The laser-cooling process is characterized by the cooling efficiency

$$\eta_{cool} = \left(\eta\lambda_p - \overline{\lambda}_f\right)/\overline{\lambda}_f, \tag{4}$$

where η is the net quantum efficiency of the rare-earth excited state [13]. η is defined as

$$\eta(\lambda_p, T) = \eta_{abs}\eta_{ext}, \tag{5}$$

where η_{ext} describes the efficiency with which an excited ion produces a luminescence photon that escapes from the sample. The absorption efficiency, $\eta_{abs} = \alpha_r(\lambda)/\left(\alpha_r(\lambda) + \alpha_b\right)$, accounts for the fraction of excited photons that are engaged in cooling, where $\alpha_r(\lambda)$ is the resonant (e.g. Yb^{3+}) absorption at a given wavelength and α_b is the background absorption of the material, typically assumed to be independent of pump wavelength and temperature. Note that η is a function of both temperature and pump wavelength, largely through the absorption term, η_{abs}, but also due to the spectral overlap between the rare-earth ion emission and the impurity absorption. Previous studies

have identified certain transition metal ions (e.g. Cu^{2+}, Fe^{2+}, Co^{2+}, and Ni^{2+}) and impurities having high-energy vibrational modes (e.g. OH^- and H_2O) as contributors to lowering the net quantum efficiency [14]. It was estimated that the concentration of such impurities must be below the 100 parts-per-billion (ppb) range for a material to realize practical cooling efficiencies at cryogenic temperatures. The measurement of impurity concentrations is therefore a prerequisite for the systematic development of advanced purification and fabrication methods for laser-cooling materials.

Here we use the net quantum efficiency of the material as an indirect measure of the aggregate impurity concentration, providing a quantitative benchmark for the quality of a sample. While measurements of absolute quantum efficiencies of luminescent materials are notoriously difficult, particularly when η is close to 1, the situation is fortunate in laser-cooling materials. Here, the wavelength difference $\eta\lambda_p - \overline{\lambda}_f$ can be tuned to one of the two points where laser-induced cooling and laser-induced heating are exactly balanced and no laser-induced temperature change occurs. Figure 3 illustrates the normalized laser-induced change in temperature, ΔT (which is proportional to η_{cool}), as a function of pump wavelength. The heat-balanced points (solid dots) can be reached by tuning $\eta\lambda_p - \overline{\lambda}_f$ either by (1) changing λ_p at a fixed sample temperature and observing the wavelength where this crossover point occurs (referred to as the zero crossing wavelength, λ_{ZCW}), or (2) by changing $\overline{\lambda}_f(T)$ via the sample temperature at a fixed laser wavelength. In the latter case, ϑ then gradually increases as the sample temperature is

lowered (and $\eta\lambda_p - \overline{\lambda}_f$ is decreased via increasing $\overline{\lambda}_f$) until laser-induced cooling switches over to laser-induced heating ($\vartheta > 0$) at a characteristic sample temperature. This crossover point is referred to as the zero-crossing temperature (T_{ZCT}) where laser-induced cooling and heating are exactly balanced, i.e. $\vartheta = 0$. This is the lowest temperature at which the sample can sustain laser-induced cooling and is yet another benchmark for laser-cooling performance. At the two heat-balanced points, the laser induced temperature change, $\Delta T \propto \eta_{cool} = \left(\eta\lambda_p - \overline{\lambda}_f\right)/\overline{\lambda}_f = 0$, and the net quantum efficiency $\eta(\lambda_p, T) = \overline{\lambda}_f / \lambda_p$, can be calculated from two easily observable quantities. Laser-induced temperature changes near the heat-balanced point are small, and a sensitive, non-contact thermometry method is therefore needed.
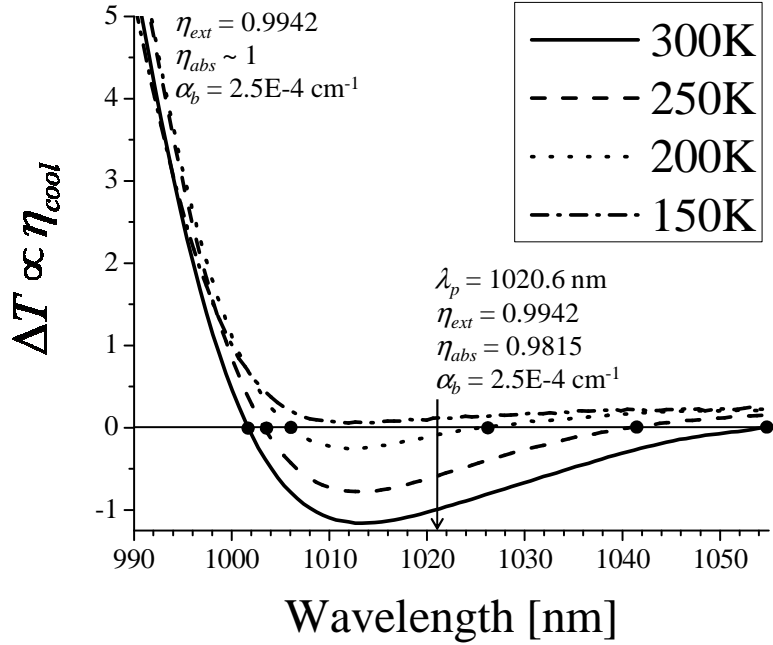
Figure 3   Calculation of the normalized laser-induced temperature change as a function of wavelength illustrating the two points for a given sample temperature where ΔT (and thus η_{cool}) go to 0. The long-wavelength zero crossing arises due to $\alpha_b > 0$. A widely tunable pump source would clearly be required to predict the T_{ZCT} for this long-wavelength zero crossing. However, near this zero crossing, a large ΔT is observed, allowing greater sensitivity. The short-wavelength zero crossing occurs when $\lambda_p = \overline{\lambda}_f$. Here, α_r is large and α_b can be neglected, allowing for a measurement of η_{ext}. The values of η_{ext}, η_{abs} and α_b used for this example calculation are also shown. These calculations were derived from Eq. 2 in Chapter 2.

Changing the pump wavelength to locate one of the temperature balanced points is a

conceivably easier experiment; however, widely tunable, high power lasers are not

necessarily available at the desired pump wavelengths. At longer pump wavelengths, we

can take advantage of the second approach to finding a temperature balanced point when

such tunable pump sources are not readily available, as was the case for our particular experiment.

At shorter wavelengths, where $\lambda_p \approx \overline{\lambda}_f$, α_b is insignificant with respect to the large α_r. Therefore, $\eta_{abs} \sim 1$ and thus $\eta \sim \eta_{ext}$ and the cooling efficiency should be approximately linear with respect to λ_p. In this case, η_{ext} can be measured by a standard fractional heating experiment [14] that observes ΔT as a function of λ_p to find λ_{ZCW}. However, in the longer wavelength region, α_r is significantly smaller and α_b becomes more significant and must be accounted for. Assuming that η_{ext} does not vary with wavelength, α_r can be found at the shorter wavelength and used to determine η_{abs} [in Eq. 5]. Additionally, given $\alpha_r(T)$, we can estimate the background absorption, α_b. Thus, each zero crossing point provides valuable information on η_{ext} and α_b and thus on the impurity concentration.

An experiment thus consists of measuring $\Xi(T,t)$ transients at different sample temperatures, fitting the power law [Eq.(3)] to the slow component of each transient, calculating the slopes ϑ, deducing the T_{ZCT} from a plot of ϑ versus sample temperature, and calculating $\eta = \overline{\lambda}_f / \lambda_p$ from $\overline{\lambda}_f$ at the T_{ZCT}. The measured net quantum efficiency η or the T_{ZCT} can be used as a measure for the quality of a laser-cooling sample, where a higher value of η or lower T_{ZCT} is indicative of a sample with a lower level of impurities.

This method enables performance benchmarking of laser-cooling samples by correlating lower impurity samples with lower T_{ZCT} values.

3. Experimental Section

A. Yb^{3+}-doped Fluorozirconate Glasses

Several Yb^{3+}-doped ZBLANI (ZrF$_4$-BaF$_2$-LaF$_3$-AlF$_3$-NaF-InF$_3$) glasses were characterized by the TBDLT method described in Section 2. Table 1 summarizes the glass compositions and provides comments on sample preparation conditions. Sample No. 1 was synthesized from commercially available high-purity metal fluoride precursors without conducting any further purification except the mandatory drying and fluorination of metal fluoride precursors in hot hydrogen fluoride gas. Samples No. 2, 3, and 4 incorporate progressive stages of the solvent-extraction purification currently under development in our laboratory, a process that aims at reducing transition-metal impurities to low-ppb levels [2],[3]. Samples No. 5 and 6 are identical to Sample No. 4, except for a higher 2 mol% Yb^{3+} concentration in Sample No. 5, and sublimated (another purification technique) rather than solvent-extracted ZrF$_4$ in sample No. 6. Sample No. 7 is a commercial ZBLAN:Yb^{3+} sample procured from IPG Photonics that has shown good laser-cooling performance, and it was used as a point of reference in this study.

B. TBDLT Experiments

The TBDLT experimental setup is shown schematically in Figure 4. The sample was mounted on the temperature-controlled cold finger of liquid-nitrogen flow cryostat

(Helitran, LT-3-110) and cooled to the desired temperature in the 100–300 K range. The ambient sample temperature was measured by a miniature (1.5 mm diameter) calibrated silicon diode (Lakeshore DT-421) mounted directly onto the surface of the sample using a small amount of Apiezon grease. Direct measurement of the sample temperature was important because different samples exhibited different temperature gradients between the sample and the cold finger temperature sensor depending on the quality of the thermal contact. TBDLT decouples laser-induced temperature changes at the surface from those inside the sample in the time domain, and we confirmed that any potential heating of the small silicon diode at the sample surface during exposure to laser and luminescence light did not affect the measurement.
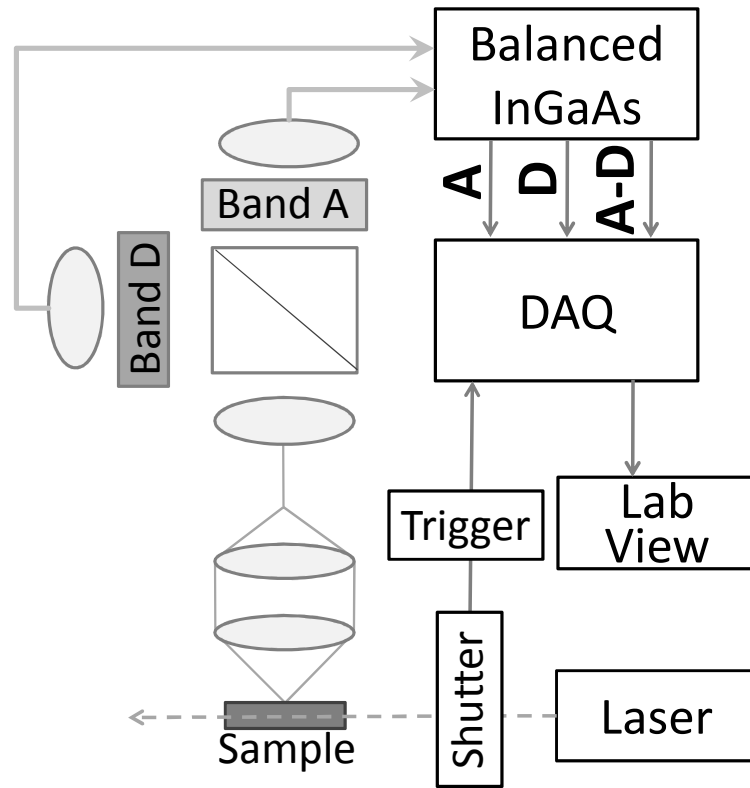
Figure 4 Schematic of the TBDLT experimental setup described in detail in Section 3.B. The transmission spectra of the filters used to define bands A and D are shown in Figure 2.

A diode-pumped continuous-wave (CW) Yb:YAG laser (Nanolase, DP12011-T01) equipped with a tunable birefringent filter (1010-1050 nm) produced ~3.5 W of pump power at 1020.5 nm with a Gaussian intensity distribution. This pump wavelength was chosen as a compromise between maximizing the absorbed power for the entire temperature range (favoring a shorter wavelength) and maximizing the laser-cooling efficiency (favoring a longer wavelength). Excitation of the sample was performed in a time sequence consisting of pump laser exposure for 5 seconds during which the sample

heated or cooled, followed by the pump laser being off for 5 seconds during which the sample equilibrated back to the ambient temperature set by the cryostat. A function generator was used to control the respective laser shutter and to trigger the data acquisition system. The time constant of the mechanical laser shutter was ~20 ms, and luminescence transient data collected for $t < 25$ ms was therefore discarded. The pump beam was focused into the sample and, in order to reduce the effects of luminescence reabsorption, the focal spot was aligned near the sample surface through which the luminescence was collected.

Sample luminescence was collected and collimated by a 2-inch diameter lens ($f = 60$ mm) and coupled into a 600-µm diameter multimode fiber by a second lens ($f = 100$ mm). For reference, the luminescence spectrum was recorded with an Ocean Optics mini-spectrometer (SD2000) at each sample temperature. The luminescence emerging from the multimode fiber was collimated and then divided into two beams by a 50:50 non-polarizing beam splitter cube. One beam was filtered by bandpass filter A (Andover Corporation, 950FS10), and the other beam was filtered by bandpass filter D (Andover Corporation, 100FS10). Figure 2 shows the transmission spectra of the commercial interference filters used to select bands A and D of the Yb^{3+} luminescence spectrum. Note that the spectrally narrower bands B and C (indicated in Figure 1) were omitted for simplicity and because they could not be selected easily with commercially available bandpass filters. Each filtered beam was re-coupled into respective 600-µm diameter multimode fibers that terminated on a pair of InGaAs balanced photodiodes (ThorLabs PDB150C). The PDB150C balanced photodetector consists of two photodiodes with well

matched responsivity and provides separate voltage outputs that are proportional to the optical power received in each band A and D. In addition, the PDB150C includes an ultra-low noise, high speed transimpedance amplifier that generates an output voltage proportional to the *difference* in the optical power in bands A and D, i.e. $(I_A^* - I_D^*)$. The voltage at each of these three detector outputs was independently and simultaneously measured by a multi-channel data acquisition (DAQ) board (Measurement Computing, USB-1616FS) that provided 16-bit resolution at a simultaneous acquisition rate of 36 kHz/channel, enabling time resolutions of up to ~30 µs in the measured TBDLT transients. The DAQ board transferred the data via USB to a PC-based LabView application that captured and analyzed the data real-time. To achieve maximum dynamic range, the two filtered beam paths were aligned for each measurement such that the measured difference signal $(I_A^* - I_D^*)$ was zero for CW pumping.

The transients recorded during each 5-second pump interval were averaged until the desired signal-to-noise ratio in the TBDLT transient was obtained. Typical averaging times ranged from 10 minutes (60 intervals) to 2 hours (720 intervals), depending on the luminescence intensity available at a particular temperature.

4. Results and Discussion

The TBDLT characterization included six Yb^{3+}-doped ZBLANI samples prepared in our laboratory (Samples No. 1-6) and a commercial 2% Yb^{3+}-doped ZBLAN sample (IPG

Photonics; Sample No. 7) which had shown substantial laser cooling in earlier experiments (see Table 1).

Table 1 Yb^{3+}-doped fluorozirconate glass samples used in this study. The ZBLANI composition is given in mol% of the respective $ZrF_4–BaF_2–LaF_3–AlF_3–NaF–InF_3$ metal fluoride constituents. A detailed description of solvent-extraction and hydrogen fluoride gas drying processes is given in Ref.[2].

Sample Number	Yb^{3+} (mol%)	ZBLANI composition (mol%)	Sample descriptions and preparation notes
1	1	54–21–3.5–3.5–16.5–0.5	Synthesized from commercial metal fluoride precursors without further purification. Some bulk scattering.
2	1	54–21–3.5–3.5–16–1	First generation solvent-extraction purification process. Some bulk scattering.
3	1	53–20–3–3–17.5–2.5	Second generation solvent-extraction purification process. Excellent optical quality.
4	1	53–20–3–3–17.5–2.5	Third generation solvent-extraction purification process. Improved hydrogen fluoride gas drying process. Excellent optical quality.
5	2	53–20–2–3–17.5–2.5	Same as No. 4 but with 2% Yb^{3+} doping.
6	1	53–20–3–3–17.5–2.5	Same as No. 4 but ZrF_4 was purified by sublimation rather than solvent extraction.
7	2	Unknown	Commercial ZBLAN sample from IPG Photonics.

Figure 5 shows TBDLT transients for Sample No. 4 and Sample No. 7 at different temperatures. The solid lines represent least-squares fits of the power law in Eq.(3) to the

135

transient data. The measured TBDLT transients are described well by this functional shape. Both samples exhibit laser cooling at 300 K as evident from the negative slope of the transient at that temperature. The magnitude of cooling gradually diminishes as the temperature is lowered, i.e. as $\eta\lambda_p - \overline{\lambda}_f$ decreases due to the increase in $\overline{\lambda}_f$. This is more clearly illustrated in Figure 6, which shows the respective TDBLT parameter ϑ as a function of sample temperature. The closed symbols are the experimental data while the open symbols were obtained from modeling calculations described in detail elsewhere [12]. The temperatures at which laser-induced cooling and heating are exactly balanced, T_{ZCT}, are found by interpolation to be 238 K and 158 K for Samples 4 (filled circles) and 7 (filled squares), respectively. Note that ϑ goes through a maximum around 133 K for Sample 7. With decreasing temperature, the pump absorption coefficient decreases and causes the sample to heat less; while the cooling efficiency decreases and causes the sample to heat more. The maximum at 133 K is a result of these two competing effects.
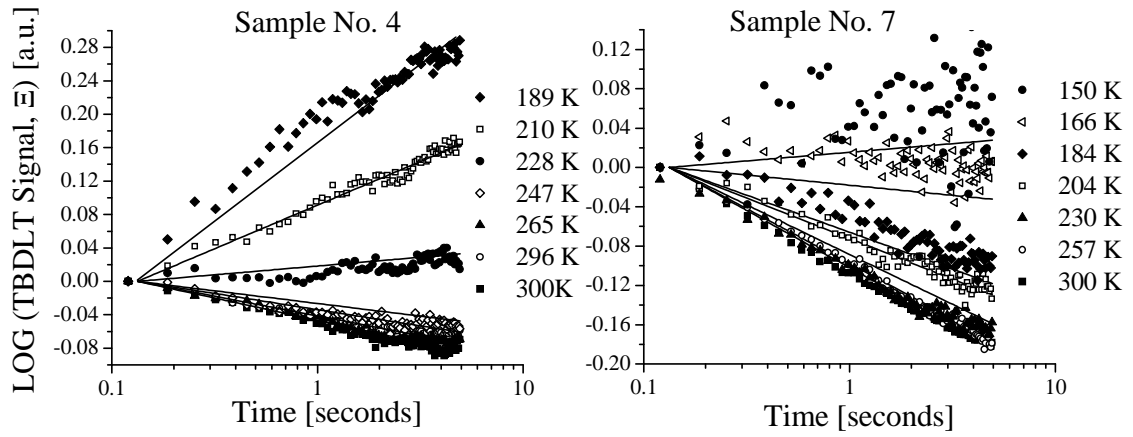
Figure 5 Transient TBDLT signal corresponding to the laser-induced temperature change at different ambient sample temperatures for Sample 4 (left) and Sample 7 (right). Negative slopes indicate laser-induced cooling while positive slopes indicate laser-induced heating. The solid lines are fits of the power law [Eq.(3)] to the experimental data.
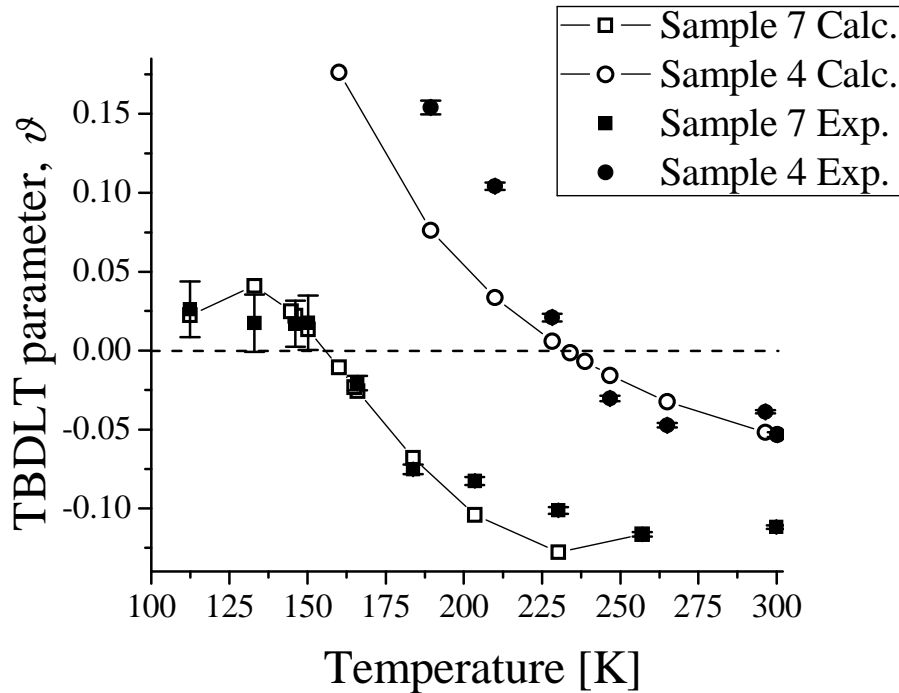
Figure 6 TBDLT parameter as a function of ambient temperature for Samples 4 (circles) and 7 (squares). Open symbols indicate ϑ calculated from a theoretical model [12], while closed symbols indicate experimental data. Points below the horizontal line ($\vartheta < 0$) indicate laser-induced cooling while points above the line ($\vartheta > 0$) indicate heating. From this data, the ZCT can be deduced as 238 K for Sample 4 and 158 K for Sample 7.

The 150 K measurement of ϑ for Sample 7 has an uncertainty that is just above the zero line, indicating that this temperature change is just resolvable with the TBDLT technique. The calculated laser-induced temperature change at this point is ~7 mK [12], a value that is representative of the sensitivity of the TBDLT method. This sensitivity is indicative of what can be achieved for Yb^{3+}-doped ZBLAN glass. Other materials will have different luminescence spectra with different temperature dependence and may thus lead to a different sensitivity.

Figure 7 shows the mean luminescence wavelength $\overline{\lambda}_f(T)$ calculated from the luminescence spectra recorded at different temperatures for Samples No. 4 and 7. $\overline{\lambda}_f(T)$ is fit with a cubic polynomial function, and the respective fits (solid lines in Figure 7) can be used to calculate $\overline{\lambda}_f(T_{ZCT})$. Using the T_{ZCT} found in Figure 6, this yields 993.9±0.4 nm and 995.9±0.4 nm for Sample No. 4 and 7, respectively. Given the fixed laser wavelength of 1020.6 nm, the net quantum efficiency $\eta = \overline{\lambda}_f / \lambda_p$ can now be calculated to yield 97.39±0.01% (at 238 K) and 97.58±0.01% (at 158 K) for Sample No. 4 and 7, respectively. The higher T_{ZCT} and slightly lower net quantum efficiency of Sample No. 4 indicates that this sample had a higher concentration of impurities than commercial sample No. 7, demonstrating that precise measurements of net quantum efficiency efficiencies are possible with TBDLT. These values are also summarized in Table 2.
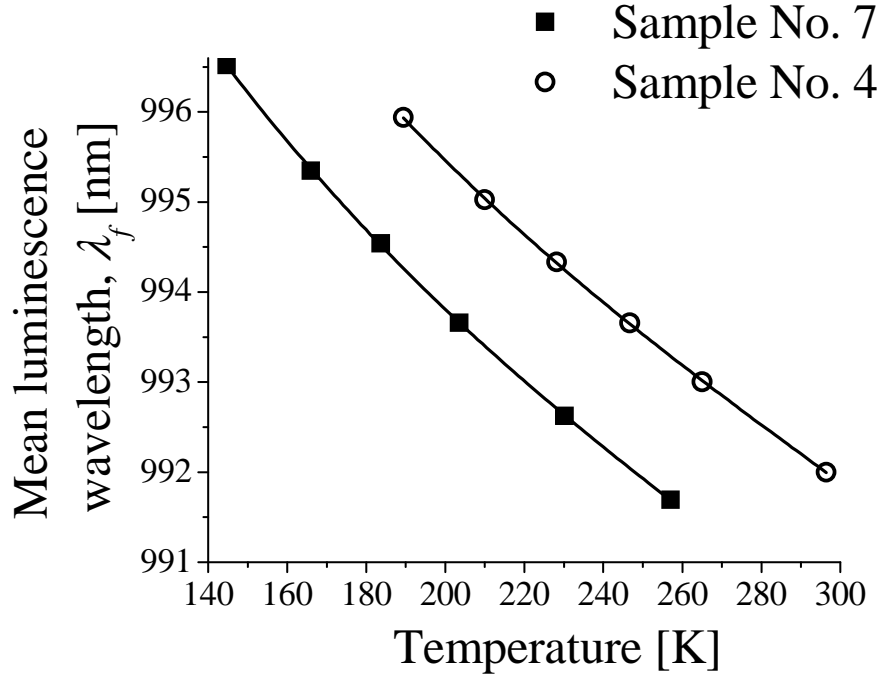
Figure 7 Mean luminescence wavelength, $\overline{\lambda}_f(T)$, as a function of temperature for Samples 4 (open circles) and 7 (filled squares). The cubic polynomial fits (solid lines) were used to interpolate $\overline{\lambda}_f(T)$ at temperatures of interest. The mean luminescence wavelength is defined as $\overline{\lambda}_f(T) = \int \lambda \, I(\lambda,T) \, d\lambda \Big/ \int I(\lambda,T) \, d\lambda$ which is calculated from luminescence spectra $I(\lambda,T)$.

Table 2 Summary of parameters critical for assessment and comparison of Samples 4 and 7. T_{ZCT} and η were measured as described in detail in this article. η_{ext} was measured using a thermal camera and a Ti:Sapphire pump source in a fractional heating experiment as described elsewhere [14]. η_{abs} was derived from the measurements of η and η_{ext}. α_b was calculated given η_{abs} and α_r. Sample 7 has a lower T_{ZCT}, η_{abs}, α_b and a higher η and η_{ext}, indicating it contained fewer impurities as compared to Sample 4. The values for η_{abs}, α_b and α_r are reported at T_{ZCT} and $\lambda_p = 1020.6$ nm.

	T_{ZCT} [K]	η_{ext}	η_{abs}	η	α_r [cm^{-1}]	α_b [cm^{-1}]
Sample 4	238	0.9906	0.9831	0.9739	0.0315	5.42E-4
Sample 7	158	0.9942	0.9815	0.9758	0.0165	3.11E-4

A more detailed discussion of the net quantum efficiency in Eq.(4) is instructive, as past reports of the quantum efficiency were higher than those we report here [13]. This lower η in the present experiments is due to the fact that the material is pumped at a longer wavelength where the absorption efficiency (η_a, in Eq.(5)) is lower, indicating the presence of impurities. In an impurity-free material, $\alpha_b = 0$ and $\eta \sim \eta_{ext}$. As shown in Table 2, this is clearly not the case for Samples 4 and 7. Given η_{ext} and $\alpha_r(T_{ZCT}, \lambda_p)$, α_b can be calculated. Background absorption coefficients of $\alpha_b = 5.42 \times 10^{-4}$ cm^{-1} and $\alpha_b = 3.11 \times 10^{-4}$ cm^{-1} are found for Sample 4 and Sample 7, respectively, indicating a lower impurity concentration in Sample 7. This trend is in agreement with a lower T_{ZCT} for sample 7, compared to Sample 4.

An even more expeditious characterization can be done by simply measuring the TBDLT parameter ϑ at room temperature. As seen in Figure 6, a smaller value of ϑ corresponds to a lower T_{ZCT} and thus higher quantum efficiency. While a room-temperature measurement alone does not provide the T_{ZCT} or η, it allows for a relative comparison of the performance of different laser-cooling samples. All samples listed in Table 1 were characterized in this manner, and the respective ϑ-values are shown in Figure 8. Sample No. 1 clearly illustrates that even the best commercial metal fluorides have insufficient purity to enable laser cooling; this sample showed substantial laser-induced heating even at room temperature. Purification of precursor materials along with a sufficiently high InF$_3$ oxidizer concentration, optimized hydrogen fluoride drying, and sufficiently long melting times [2] provide a substantial improvement of laser cooling

performance as evident from the successive implementation of these processes in samples No. 2, 3, and 4. The 1% Yb^{3+} concentration of Sample No. 4 was increased to 2% in Sample No. 5, which resulted in substantial heating. The rate of energy migration among Yb^{3+} ions increases with increasing Yb^{3+} concentration, and some of the excitations can find impurity sites where non-radiative relaxation takes place. This process is more efficient in the 2% sample (No. 5) compared to the 1% sample (No. 4), and the fact that sample No. 5 showed substantial heating is direct evidence for energy migration to transition-metal and/or OH^- impurity sites. Also note that the use of ZrF_4 purified by sublimation (sample No. 6) resulted in a sample that cooled, however not as much as the best sample fabricated from precursors purified by solvent extraction.
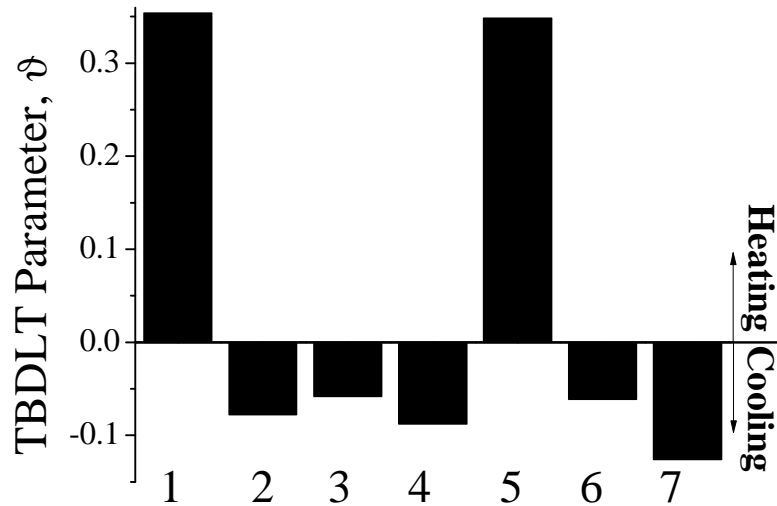
Figure 8 TBDLT parameter, ϑ, (measured in vacuum at room temperature ($T = 296$ K) and with $\lambda_p = 1020.5$ nm) for a qualitative comparison of several ZBLANI:Yb^{3+} samples fabricated in our laboratory (Samples 1 - 6) and one sample commercially procured (IPG, Sample 7). A positive ϑ corresponds to heating, while a negative ϑ corresponds to local

laser-induced cooling. Here we show a steady improvement in our purified materials over those produced with commercially available starting materials.

5. Conclusions

We have successfully demonstrated TBDLT – a non-contact spectroscopic technique for measuring laser-induced temperature changes in optical materials. This method was used to characterize and benchmark the performance of optical refrigerator materials. The TBDLT method uses two commercially available band pass filters to select regions of the luminescence spectra that show different temperature dependences. These temperature induced luminescence intensity changes can quantify laser-induced heating and cooling processes. TBDLT achieved a sensitivity of 7 mK and could successfully detect the temperature at which laser-induced heating and cooling are exactly balanced. We have shown that net quantum efficiency can be obtained with high precision using TBDLT. Several Yb^{3+}-doped fluorozirconate glasses were characterized by this method, and the results provided valuable feedback to the development of material purification and fabrication processes. The best ZBLANI:1%Yb^{3+} sample produced in our laboratory had a T_{ZCT} of 238 K and a corresponding net quantum efficiency of 97.39% at a pump wavelength of 1020.6 nm. This laser-cooling performance is a substantial improvement over samples prepared from commercial grade, high-purity metal fluoride precursors. While the TBDLT technique was shown to be an expedient and effective experimental method for characterizing the laser-cooling performance of Yb^{3+}-doped fluorozirconate glasses, it can be adapted easily to other rare-

earth doped crystals and glasses. TBDLT enables a key diagnostic capability that is critical to the further development of high performance solid-state optical cryocoolers.

Acknowledgments

References

[1] R. I. Epstein, M. I. Buchwald, B. C. Edwards, T. R. Gosnell, and C. E. Mungan, "Observation of laser-induced fluorescent cooling of a solid," Nature **377**, 500-503 (1995).

[2] M. P. Hehlen, in *Optical Refrigeration. Science and Applications of Laser Cooling of Solids*, R. I. Epstein and M. Sheik-Bahae, eds., (Wiley, Weinheim, 2009), pp. 33-68.

[3] W. M. Patterson, M. P. Hehlen, , R. I. Epstein, M. Sheik-Bahae, "Synthesis and evaluation of ultra-pure rare-earth-doped glass for laser refrigeration," Proc. SPIE 7228, 72280C (2008).

[4] D. Seletskiy, M. P. Hasselbeck, M. Sheik-Bahae, R. I. Epstein, S. Bigotta, and M. Tonelli, "Cooling of Yb:YLF using cavity enhanced resonant absorption," Proc. SPIE 6907, 69070B (2008).

[5] D. V. Seletskiy, S. D. Melgaard, S. Bigotta, A. Di Lieto, M. Tonelli, R. I. Epstein, and M. Sheik-Bahae, "Demonstration of an Optical Cryocooler," in *Conference on Lasers and Electro-Optics/International Quantum Electronics Conference*, OSA Technical Digest (CD) (Optical Society of America, 2009), paper IPDA9.

[6] R. Frey, F. Micheron, and J. P. Pocholle, "Comparison of Peltier and anti-Stokes optical coolings," J. Appl. Phys. **87**, 4489–4498 (2000).

[7] G. Mills and A. Mord, "Performance modeling of optical refrigeration," Cryogenics, **46**, 176-182 (2005).

[8] G. Lamouche, P. Lavallard, R. Suris, and R. Grousson, "Low temperature laser cooling with a rare earth doped glass," J. Appl. Phys. **84**, 509-516 (1998).

[9] V. K. Rai, "Temperature sensors and optical sensors," Appl. Phys. B **88**, 297–303 (2007).

[10] B. Imangholi, M. P. Hasselbeck, D. A. Bender, C. Wang, M. Sheik-Bahae, R. I. Epstein, S. Kurtz, "Differential luminescence thermometry in semiconductor laser cooling," Proc. SPIE 6115, 215-220 (2006).

[11] D. V. Seletskiy, M. P. Hasselbeck, M. Sheik-Bahae, and R. I. Epstein, "Fast differential luminescence thermometry," Proc. SPIE 7228, 72280K 2009.

[12] W. M. Patterson, M. Sheik-Bahae, R. I. Epstein, and M. P. Hehlen, "Model of laser-induced temperature changes in solid-state optical refrigerators," submitted for publication in Journal of Applied Physics, October 2009. (Will update right before this article goes to print).

[13] M. Sheik-Bahae and R.I. Epstein, "Optical refrigeration," Nature Photonics **1**, 693-699 (2007).

[14] M. P. Hehlen, R. I. Epstein, and H. Inoue, "Model of laser cooling in the Yb^{3+}-doped fluorozirconate glass ZBLAN," Phys. Rev. B **75** [14], 144302 (2007).

[15] C. Hoyt, "Laser cooling in thulium-doped solids" (Ph.D. Dissertation, University of New Mexico, 2003), Chapters 2, 4.

Chapter 6

Conclusions

Optical refrigeration has made significant advances over the past decade, and is primed to deliver a promising technology by providing a rugged, low cost, compact, cryogenic cryocooler in the near future. This technology is predicted to be especially beneficial for cooling satellite instrumentation and space-based sensors where long lifetimes, low mass, and the lack of moving parts are crucial. Although not reviewed specifically in this manuscript, much progress has been made in semiconductor-based optical refrigerators, where advanced heterostructure growth and novel device fabrication are currently underway in an effort to achieve high external quantum efficiency.

Summary and significance of contributions

The focus of this research was in developing and characterizing rare-earth doped, solid state materials for laser cooling by optimizing the cooling efficiency. This manuscript has outlined the essential qualities of a laser cooling material, providing insight into what constitutes an ideal host material. To summarize, some characteristics of a host material for laser cooling include:

- Low phonon energy
- High thermal conductivity
- Narrow ground state splitting
- High absorption cross-section
- High material hardness and durability

147

- Low Thermal emissivity

- Low impurity concentration.

The necessity of these properties was each reviewed in detail in the Materials Selection of the Introduction in this manuscript.

Also discussed in the Materials Selection section of the Introduction were the characteristics of a dopant ion favorable for laser cooling. To summarize, we found that a smaller dopant energy, ΔE, (such as is the case of Tm^{3+} versus Yb^{3+}) provides higher cooling efficiency, η_{cool}, yielding more cooling power. This advantage of a smaller bandgap is offset by enhanced interaction of the excited state with host phonon modes, increasing multiphonon relaxation rates. Additionally, the higher energy levels present in Tm^{3+} or Er^{3+} give the potential for excited-state absorption and cross-relaxation. In contrast to these and other rare earth ions, Yb^{3+} is unique in that its electron configuration produces only a ^2F manifold split into a $^2F_{7/2}$ ground state and one $^2F_{5/2}$ excited state multiplet. The absence of other electronic states greatly simplifies the excitation dynamics, comparatively. It specifically excludes up-conversion or cross-relaxation processes. The multi-phonon relaxation rate is thus relatively low.

Although significant progress has been made in purifying our materials to remove impurities (such as transition metals and OH^-), they still exist and must be considered accordingly. The potential for excited state energy transfer from transition metal impurities to Tm^{3+} might possibly be less problematic since there is less spectral overlap between the emission of the Tm^{3+} ion, versus the Yb^{3+} ion, and the absorption of the impurity. Even after considering these pros and cons for thulium versus ytterbium, it is not clear which ion will provide the most benefit to the field of optical refrigeration and

researchers continue employing both. In this dissertation, both have been demonstrated and the main discoveries are now briefly summarized.

This research was the first to demonstrate laser induced cooling in a thulium doped crystal, namely $BaY_2F_8:Tm^{3+}$, as summarized in Chapter 2. Protocols for materials synthesis and purification of $ZBLANI:Yb^{3+}/Tm^{3+}$ glass components were also developed, providing a contribution to materials science outside the specific field of laser cooling. This research was first to synthesize and purify *all* of the components of ZBLANI glass. From this development, we prepared a material capable of laser induced cooling as low as 238 K with a net quantum efficiency of 0.9739. The details regarding these purification methods described in Chapter 3 can be extended to other potential ultra-pure host materials, for applications beyond laser cooling, to a variety of optical glasses and crystals. The need for a very sensitive (7 mK) non-contact temperature measurement technique was necessary for this research. The experiment, as outlined in Chapter 5, is general and could easily be modified to evaluate other materials with temperature dependent fluorescence spectra. Finally, the theory and simulation developed in Chapter 4 is also not limited to our particular example of $ZBLAN:Yb^{3+}$. The basis for this theory can be applied to evaluate cooling or heating in any material exhibiting laser induced heating or cooling. The specific benefit to our laser cooling effort is in its ability to predict what materials will cool and by how much.

Future Work

Materials

Certainly, the work presented in this dissertation can be extended and improved. Improving and optimizing the purification techniques of the precursor materials and the

glass/crystal synthesis is an obvious extension given that only a few iterations of the entire process were performed for the materials discussed in this study. An exploration of the optimum pH for more efficient transition metal extraction for each fluoride component could be studied more comprehensively. There are also a number solvents and reagents used throughout the purification process which could be investigated as well. For example, APDC (see Chapter 3) is the chelate used to remove transition metals in our current system, however, other chelates such as DDTC or DOED might prove more efficient at extraction in one component of the glass system. The buffer used to control the pH was an acetate found to interfere with fluoride formation for two of the fluorides. Perhaps an alternative buffer could be explored, such as a citrate or formate. Additionally, the analysis of transition metal concentration was only performed on the zirconium portion of the glass. Further studies would analyze the degree of purification in the remainder of the glass components as well. One might also find from such a study that three successive extraction steps are not required to reduce impurities to the desired level. There is also room for improvement of the HF/Ar ultra-drying system developed to reduce OH^- impurities. Different drying temperatures and times could be explored, and the concentration of HF monitored, to better control the amount of HF exposure for the fluorides.

New materials, in addition to ZBLANI, are certainly being investigated [1]. For simplicity, the six component system of ZBLANI could be reduced to a more simple glass, such as BIG, for example. Although we have presented methods for purifying fluoride glasses, many properties make crystals the likely choice for next generation coolers. For example, high dopant concentrations for ZBLANI are not stoichiometrically

feasible, given that the dopant partially substitutes for LaF$_3$ (constituting only 4% at most). Also, as discussed in detail in the Materials Selection section in the Introduction of this manuscript, crystals not only allow higher doping concentrations, but also exhibit crystal field splitting which leads to sharp Stark manifolds and thus higher, concentrated peak absorptions near the cooling wavelengths of interest. A good example of that is the recent demonstration of optical cooling in LiYF$_4$ [2]. Certainly there is much to explore regarding the influence of the doping level on the cooling efficiency. Additionally, the radiative heat load on the sample could be dramatically decreased by using a host material such as BaY$_2$F$_8$ that has low emissivity.

Experiment

Improvements in the characterization and evaluation of our laser cooling materials, as well as methods to increase the absorbed power in the samples are needed. Although the TBDLT method outlined in Chapter 5 is quite sensitive, measuring laser cooling transients at very low temperatures proved time consuming. An even more sensitive experiment incorporating a spectrometer (or monochrometers) with better resolution could reduce the need for long averaging times. This will become more important as materials cool at lower and lower temperatures, as is expected.

New pump sources will be necessary as we seek to increase the pumping power and expand the tunability of experiments (a current limitation). The use of a high power, tunable, solid state pump laser is very useful for studying the cooling properties of a material; however, the use of a diode laser is more appealing from a technological point of view. The limited power, tunability, and poor optical quality of diode lasers would need to be improved.

In order to increase the absorbed power, new pump geometries could be employed. Cavity-enhanced and other advanced multi-pass pumping schemes have already been successfully demonstrated and provide a starting point in developing more efficient ways to trap the pump radiation. Showing great promise, are the cavity enhanced methods, where the sample is placed in a resonant cavity external to the pump source. However current limitations in cavity stability must be overcome [3]. Trapping the beam in a non-resonant cavity has also been demonstrated where the cooling power was increased over 250% [4]. Finally, improvements in the deposition of extremely high quality mirrors should be pursued for either of these methods. The benefits of ion beam sputtering techniques could be explored for such high quality dielectric mirrors.

References

[1] M. P. Hehlen, "Novel materials for laser refrigeration," Proc. SPIE 7228, 72280E (2009).

[2] V. Seletskiy, S. D. Melgaard, S. Bigotta, A. Di Lieto, M. Tonelli, R. I. Epstein, and M. Sheik-Bahae, "Demonstration of an Optical Cryocooler," in *Conference on Lasers and Electro-Optics/International Quantum Electronics Conference*, OSA Technical Digest (CD) (Optical Society of America, 2009), paper IPDA9.

[3] D. Seletskiy, M. P. Hasselbeck, M. Sheik-Bahae, R. I. Epstein, S. Bigotta, and M. Tonelli, "Cooling of Yb:YLF using cavity enhanced resonant absorption," Proc. SPIE 6907, 69070B (2008).

[4] C. Hoyt, "Laser cooling in thulium-doped solids" (Ph.D. Dissertation, University of New Mexico, 2003).